Probing the Role of Hot Carriers and Photothermal Effects in Plasmonic Photocatalysis with Ultrafast Surface-Enhanced Raman Spectroscopy

A Dissertation

SUBMITTED TO THE FACULTY OF THE

UNIVERSITY OF MINNESOTA

BY

Emily L. Keller

IN PARTIAL FULFILLMENT OF THE REQUIREMENTS

FOR THE DEGREE OF

DOCTOR OF PHILOSOPHY

Advisor

Renee R. Frontiera

August 2018

Acknowledgements

I would not have made it to this point in my academic career without the help and support of my mentors, colleagues, friends, and family.

To Renee, thank you for choosing me as one of the founding members of your lab. I've always appreciated our conversations. Every time I left your office, I would be excited about science and my research, even if I had entered feeling very discouraged by the way things were currently going in lab. Thanks for being an awesome mentor and providing me with so many opportunities to grow as a scientist and as a person. Your guidance has been invaluable over the years!

To the Frontiera group, past and present members, I am indebted to all of you for your helpful discussions, support (and mutual suffering), consumption of my baked goods, and friendship over the last 5 years. The journey through graduate research is not an easy one, and your presence has made this path an enjoyable one.

To my friends, I cannot express how much your companionship and camaraderie has buoyed me through the hardships and struggles of graduate school. Your encouragements, as well as evenings off attending games nights or going out to dinner, made facing experimental difficulties more manageable.

To my family, your support and faith in me has always driven me to be the best I can be. I would not have accomplished near as much without your love and unwavering belief in my future successes.

Abstract

Plasmonic materials convert light into chemical energy, which is used to drive chemical reactions with greater efficiency and selectivity than traditional catalysts. To enhance the efficacy of these plasmon-driven processes, it is critical to determine the underlying mechanisms that occur once plasmons are excited by light. However, the manner in which these materials convert light into chemical energy is poorly understood due to the fast time scales of energy partitioning into various plasmon decay pathways, including hot carrier generation, localized heating, and enhanced electromagnetic fields. To that end, I have developed ultrafast surface-enhanced Raman spectroscopy (SERS) as a technique to probe the fundamental interactions between plasmons and molecules to elucidate a possible mechanism for plasmon-driven photochemistry.

Initial studies using ultrafast SERS examined plasmon-molecule interactions to probe how hot electron generation upon plasmon decay affects adsorbed molecules. The observed photophysical response of 4-nitrobenzenethiol (4-NBT) adsorbed to aggregated gold nanoparticles allowed for the quantification of charge delocalization across the plasmonic substrate. The surprisingly large number of charges available is promising for hot electron driven plasmonic processes.

Later studies focus on the modification of the ultrafast SERS instrument for ultrafast nanoscale Raman thermometry measurements. The ability to measure the localized heating of adsorbates on plasmonic materials is essential for understanding the contribution of localized heating in plasmonic photocatalysis. Follow-up studies examine

the effect of the local environment upon plasmonic heating of adsorbed molecules. The local environment is an important consideration as catalysts are commonly stabilized by various catalytic support materials.

Finally, I characterize the plasmonic properties of a new non-noble plasmonic material, consisting of copper selenide nanoparticles ($Cu_{2-x}Se$ NPs), by measuring their SERS enhancement factor. Additionally, $Cu_{2-x}Se$ NPs are promising photocatalysts as shown by their ability to dimerize 4-NBT in the presence of light. New plasmonic materials, like $Cu_{2-x}Se$ NPs, are exciting earth-abundant and cost-effective alternatives to the more traditional noble metal photocatalysts.

Herein, I show that ultrafast SERS provides a unique approach to examine plasmon-molecule interactions on the picosecond time scale of chemical reactivity. This technique has the potential to determine the underlying processes that directly influence plasmon-mediated catalysis and to provide insights for the development of more efficient plasmonic photocatalysts.

Table of Contents

List of Tables

List of Figures

Chapter 2: Ultrafast Surface-Enhanced Raman Spectroscopy

Chapter 3: Monitoring Charge Density Delocalization upon Plasmon Excitation with Ultrafast Surface-Enhanced Raman Spectroscopy

Chapter 4: Ultrafast Nanoscale Raman Thermometry Proves Heating Is Not a Primary Mechanism for Plasmon-Driven Photocatalysis

Appendix C: Supporting Information for Manuscript: Effect of Silica Supports on Plasmonic Heating of Molecular Adsorbates as Measured by Ultrafast Surface-Enhanced Raman Thermometry

Appendix D: Supporting Information for Manuscript: Plasmon-Enhanced Chemical Sensing and Conversion using Copper Selenide Nanoparticles

Appendix E: Supporting Information for Chapter 7: Prospects

List of Abbreviations

AlNCs	aluminum nanocrystals
AlNC-Pd	aluminum nanocrystals decorated with palladium islands
p-MA	*p*-aminothiophenol
AuNPs	gold nanoparticles
AuNRs	gold nanorods
BBO	beta-barium borate
BPE	*trans*-1,2-bis(4-pyridyl)ethylene
BT	benzenethiol
CFQ	7-(trifluoromethyl)quinoline-4-thiol
COORS	common old ordinary Raman spectroscopy
CTAB	cetyltrimethylammonium bromide
$Cu_{2-x}Se$ NPs	copper selenide nanoparticles
DMAB	dimercaptoazobenzene
EF	enhancement factor
IPA	isopropyl alcohol
IVR	intramolecular vibrational redistribution
LSPR	localized surface plasmon resonance
4-NBT/NBT	4-nitrobenzenethiol
NIR	near infrared

NOPA	non-colinear optical parametric amplifier
OAm	oleylamine
PDF	probability distribution function
PVP	polyvinylpyrrolidone
QMS	quadrupole mass spectrometer
SE-CARS	surface-enhanced coherent anti-Stokes Raman spectroscopy
SECM	scanning electrochemical microscopy
SE-FSRS	surface-enhanced femtosecond stimulated Raman spectroscopy
SEM	scanning electron microscopy
SERS	surface-enhanced Raman spectroscopy
TEM	transmission electron microscopy
TMS	chlorotrimethylsilane
TR-SE-CARS	time-resolved surface-enhanced coherent anti-Stokes Raman spectroscopy

Chapter 1

Introduction

1.1 Motivation

Plasmonic materials convert light into various forms of energy, which can be used in a myriad of applications, including photovoltaics,[1] photothermal therapies,[2] water purification,[3] and selective photocatalysis.[4,5] In particular, plasmonic photocatalysts have the potential to drive chemical reactions with greater efficiency and selectivity than traditional catalysts.[4] However, the manner in which these materials convert light into chemical energy is poorly understood. To enhance the efficacy of these plasmon-driven processes, it is critical to determine the underlying mechanisms that occur once plasmons are excited by light.[6]

A plasmon is the collective oscillation of charge density across a plasmonic nanostructure that occurs upon photoexcitation. These oscillations focus the electromagnetic field into nanoscale volumes located between nanostructures, creating hot spots. Molecules in these hot spots may experience altered reaction pathways due to the high concentration of light. Additionally, plasmons can decay *via* several competing pathways, including generation of hot or highly energetic carriers through the formation of electron-hole pairs, localized heating of the surroundings, and transfer of energy to nearby adsorbates.[5,7,8] However, knowledge of the underlying mechanisms, which determine the energy partitioning into these pathways, is lacking.

This lack of knowledge arises, in part, due to the fast time scales of the plasmon decay pathways. After photoexcitation, a plasmon quickly dampens in 10 to 100 fs through electron-electron scattering, leading to highly energetic or hot electrons.[9] These

hot electrons can have energies ranging from the Fermi energy to the work function of the material.[10] Once generated, the hot electrons may scatter off the phonons of the plasmonic material generating a hot lattice or transfer to nearby adsorbates to drive a chemical reaction. These interactions occur in 1 to 10 ps.[7] In the following 100s of picoseconds, the plasmonic substrate transfers the heat generated upon electron-phonon scattering to the surroundings. To further elucidate these plasmon decay pathways, a technique with high time resolution is needed to monitor plasmon-molecule interactions in real time.

Ultrafast surface-enhanced Raman spectroscopy (SERS) is a vibrationally sensitive technique with picosecond time resolution.[11,12] SERS is a plasmon-enhanced technique that preferentially probes the bonds of molecules adsorbed in the plasmonic hot spots.[13] Thus, SERS is an ideal technique for studying the plasmon-molecule interactions from the point of view of the molecular probe. The ability to probe picosecond dynamics of the molecular-plasmonic system will allow for the rational design of materials for more efficient plasmonic catalysts.

1.2 Outline

In the following chapters, I build upon the current understanding of the underlying mechanism of plasmonic photocatalysis by further elucidating molecular-plasmonic systems using ultrafast SERS.

Chapter 2 discusses the need for new time sensitive techniques for studying plasmon-driven photocatalysis due to the femtosecond and picosecond dynamics of

plasmon excitation and decay as well as the time scale of bonds breaking and forming. This chapter reviews various ultrafast Raman spectroscopy techniques and how the use of these techniques for studying plasmonic photocatalysis will lead to new insights into the mechanisms behind plasmon-driven processes.

In Chapter 3, I use ultrafast surface-enhanced Raman spectroscopy to examine hot carriers generated upon plasmon excitation from the molecular prospective. From these measurements, I relate the changes in the transient SERS signal depletion to charge delocalization across the plasmonic substrate and quantify the charges available to drive a chemical reaction.

In Chapter 4, I introduce a new technique, ultrafast nanoscale Raman thermometry, where I modify the ultrafast SERS technique to allow for the monitoring of changes in vibrational kinetic energy, described as effective temperatures, of the adsorbates on the aggregated gold nanoparticles upon plasmon excitation. I then estimate the impact of this degree of heating upon several examples of plasmonic photocatalysis from the literature.

In Chapter 5, I further explore the potential effects of localized plasmonic heating on plasmonic photocatalysis by examining the effect of various catalytic supports near adsorbed molecules in the hot spots. I measure the effective temperature of an adsorbate on gold nanostructures with various local environments, ranging from ligand to mesoporous silica shell to a non-porous silica shell. These measurements shed light on the impact catalytic supports upon the efficiency of plasmonic photocatalysts.

In Chapter 6, I transition away from the classic gold nanostructures discussed in previous chapters to examine the plasmonic properties of a more unique plasmonic substrate. Here, I discuss the plasmonic properties of semiconductor $Cu_{2-x}Se$ nanoparticles in terms of SERS enhancement factors and a common plasmon-driven chemical reaction and how these measured properties compare to more traditional materials, like gold nanostructures.

In conclusion, Chapter 7 discusses promising avenues of further research with these techniques, including quantifying the absorption-induced heating as well as mode-specific energy transfers between adsorbates and plasmons. Additionally, I discuss the potential of alternative plasmonic materials, including aluminum nanocrystals and the $Cu_{2-x}Se$ nanoparticles examined in Chapter 6, for plasmon-driven catalytic processes. These studies will further elucidate the mechanisms behind plasmon-mediated photocatalysis.

Chapter 2

Ultrafast Surface-Enhanced Raman Spectroscopy

Reprinted with permission from the manuscript by Emily L. Keller, Nathaniel C. Brandt, Alyssa A. Cassabaum, and Renee R. Frontiera *Analyst* **2015**, *140*, 4922-4931

2.1 Synopsis

Ultrafast surface-enhanced Raman spectroscopy (SERS) with pico- and femtosecond time resolution has the ability to elucidate the mechanisms by which plasmons mediate chemical reactions. Here we review three important technological advances in these new methodologies, and discuss their prospects for applications in areas including plasmon-induced chemistry and sensing at very low limits of detection. Surface enhancement, arising from plasmonic materials, has been successfully incorporated with stimulated Raman techniques such as femtosecond stimulated Raman spectroscopy (FSRS) and coherent anti-Stokes Raman spectroscopy (CARS). These techniques are capable of time-resolved measurement on the femtosecond and picosecond time scale and can be used to follow the dynamics of molecules reacting near plasmonic surfaces. We discuss the potential application of ultrafast SERS techniques to probe plasmon-mediated processes, such as H_2 dissociation and solar steam production. Additionally, we discuss the possibilities for high sensitivity SERS sensing using these stimulated Raman spectroscopies.

2.2 Introduction

The surface-enhanced Raman spectroscopy (SERS) field has matured significantly over the past decades since its discovery,[14,15] with clear proof of single-molecule sensitivity,[16] a general agreement upon the enhancement mechanism,[13,17,18] and the development of commercial substrates for SERS applications.[19,20] More recently, there have been exciting developments in extending SERS techniques and methodologies to the ultrafast regime, in which femtosecond and picosecond time scale techniques have

been coupled with the plasmonic materials used for SERS. These successes have opened a new direction in SERS research, in which new methods allow for the direct probing of mechanisms of plasmon-mediated chemical processes.

Plasmon-induced photochemical and photophysical processes have been the recent focus of intense research efforts[21,22] and convincing demonstrations of these new class of reactions include high efficiency photovoltaics,[1,23,24] water splitting,[25,26] and pollutant degradation.[27,28] However, many of the recent reports on plasmons as catalysts are phenomenological, as the mechanism of turnover enhancement is unknown and typically behavior is quantified only as an overall improvement in reaction efficiency. The newly developed techniques described in this minireview have great potential in elucidating direct mechanisms of plasmon-induced processes, ideally leading to great improvements in rational device design and overall efficiency.

This paper provides a review of recent ultrafast SERS methods, including surface-enhanced femtosecond stimulated Raman spectroscopy (SE-FSRS), surface-enhanced coherent anti-Stokes Raman spectroscopy (SE-CARS), and time-resolved SE-CARS (TR-SE-CARS). These recently developed techniques have convincingly demonstrated the compatibility of ultrafast pulses with highly enhancing plasmonic substrates, have conclusively proven that surface enhancement extends to stimulated Raman processes, and have enabled molecular-plasmonic studies on the femtosecond time scale of nuclear motion. These abilities allow one to directly follow bond-making and –breaking processes as plasmons induce new chemical changes in proximal molecular species. Additionally, due to the higher order fields used in stimulated Raman processes, these

new techniques may prove to be more sensitive to detection of low concentration analytes as compared to spontaneous SERS processes. These new developments build off of numerous previous works in the field which examined properties including picosecond dynamics,[29,30] tip enhanced coherent Raman spectroscopy,[31] ultrafast decay rates,[32] and ultrafast charge-transfer.[33]

This paper begins with a discussion of the electromagnetic field enhancement mechanism of SERS, followed by a discussion of the relevant time scales of coupled molecular-plasmonic system dynamics and the advantages of probing these systems with ultrafast spectroscopies. Section 2.3 discusses three recent demonstrations of ultrafast SERS, consisting of SE-FSRS, SE-CARS, and TR-SE-CARS. These three examples are chosen as they represent some of the most recent advances in the rapidly expanding ultrafast SERS field, and do not include all work in this area. They exemplify significant technical advances, by pushing the limits of time resolution and making measurements of very few numbers of molecules. We follow with an outlook on possible applications of these novel ultrafast SERS techniques, including discussions on plasmon-induced H_2 dissociation, plasmon-driven steam generation, and increased sensing specificity at low concentrations.

2.2.1 What is a plasmon and how is it related to SERS?

The dramatic signal enhancement characteristic of SERS is due in large part to the enhancement of the electromagnetic fields involved in the Raman measurement by the nanoscale metallic structures typically used as SERS substrates.[17,34,35] The underlying

origin of the electromagnetic field enhancement lies in the coupling of incident electromagnetic fields to localized surface plasmon resonances (LSPRs) of the nanoscale metallic SERS substrates. In their most basic form, plasmons are oscillations of free electron density relative to fixed nuclei in a metallic lattice and may be excited by light irradiation. Excitation occurs when the applied external oscillating electric field is matched to the resonant plasmon frequency, which is dependent on the dielectric constants of the material employed (Figure 2.1a).[36,37] The transition from bulk plasmon resonance to LSPR occurs as the result of confining the plasmon resonance to a metallic object much smaller than the wavelength of the external electric field, and results in an electric field enhancement near the surface of the metallic object on the order of 10^1 to 10^2.[38]

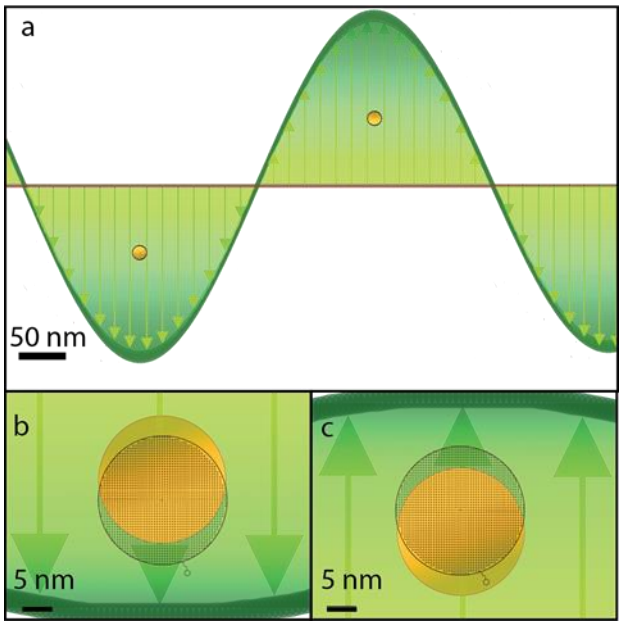

Figure 2.1 To-scale depiction of a localized surface plasmon resonance. **a.** Light with a wavelength of approximately 500 nm irradiates a 20 nm gold nanoparticle. Panels **b** and **c** depict the oscillation of the electron cloud (gold) relative to the atomic lattice (grey), in response to the incident electromagnetic field.

Figure 2.1 shows a to-scale depiction of the creation of the LSPR following light irradiation. In this case, a spherical nanoparticle with radius r is irradiated by light with wavelength λ in the long wavelength limit (given as $r/\lambda<0.1$).[34] The small size of the nanoparticle relative to the wavelength of the irradiating light allows the electric field surrounding the nanoparticle to be approximated as constant at a given time point. In the

case of a sphere, the field enhancement associated with LSPR excitation occurs along the polarization axis of the light and rapidly switches poles at the frequency of the applied field, corresponding to a period of several femtoseconds for visible light (Figure 2.1b and 2.1c).

SERS measurements are typically characterized by an enhancement factor (EF), which quantifies the amount by which the surface increases the Raman signal.[13,39] In spontaneous Raman-based SERS, the signal enhancement scales as approximately E^4, where E is the electromagnetic field. This can be understood by examining the interactions of the incident and scattered fields with a simple spherical nanoparticle using the formalism given by Van Duyne and colleagues.[34] In this case, the incident field E_0 experiences an enhancement given by:

$$|\mathbf{E}_{\text{out}}|^2 = 2E_0^2|g|^2$$

where $\mathbf{E}_{\text{out}}$ corresponds to the electric field at the surface of the nanoparticle and the field enhancement associated with the nanoparticle is given by the parameter g. The Raman-scattered electromagnetic field will experience a similar enhancement at the Raman-scattered frequency. Comparison of the enhanced fields relative to the incident field E_0 yields the enhancement factor EF as

$$EF = \frac{|\mathbf{E}_{\text{out}}|^2|\mathbf{E}_{\text{out}'}|^2}{|\mathbf{E}_0|^2} = 4|g|^2|g'|^2$$

where the terms corresponding to the Raman-scattered field are denoted by " $'$ ". Assuming the frequency of the Raman-scattered field to be close to the frequency of the

incident field yields $g = g'$ and gives an enhancement scaling of g^4. Thus, for a single particle with field enhancement of 10 (a typical value for an isolated nanosphere), the Raman signal is expected to be enhanced by 10^4.

Stronger electric field enhancement, above that expected for a single metal nanoparticle, can obtained through the use of aggregates of two or more nanoparticles.[38] When two nanostructures are placed close to one another, coupling between the LSPR of each particle results in additional field enhancement in the region between the two particles, which is commonly referred to as a "hot spot". The interaction between the two particles can be considered in a fashion similar to molecular orbital theory in molecular systems, a theory which readily leads to predictions of aggregate plasmon resonance energies and field enhancements.[40,41] For aggregated particles with field enhancements of 10^4, the SERS EF could be as high as 10^{16}. However, particles and molecules start to break down under these high field strengths and experimental EFs have only been verified to a level of approximately 10^{12}.[13] Additionally, quantum tunneling begins to dominate in this limit, as the nanostructures must be quite close together.[42]

Over the past several decades since its discovery, investigations have focused on the mechanism of SERS signal enhancement and the use of SERS for quantitative sensing of a variety of analytes.[37] The mechanism of enhancement is dominated by the electromagnetic field enhancement described above, with small contributions from chemical processes, such as charge -transfer. In the sensing area, current work focuses on solving long-standing problems such as rigorous quantification of unknown analytes and

specificity within complex media. A new and highly active area of SERS research involves the coupling of plasmonic surface enhancement with ultrafast spectroscopies, with the goal of following molecular adsorbate-plasmon interactions on the femtosecond and picosecond time scale. As plasmons have been found to enhance a number of photochemical and photophysical processes, these new ultrafast methods have the potential to quantify and elucidate the mechanisms behind these new processes, including hot electron and hole transfer, increased heating or scattering, and modification of reactive potential energy surfaces.

2.2.2 How do plasmons and molecules interact?

In addition to forming the basis for SERS, plasmonic excitations may also be exploited to drive chemical reactions.[43,44] To most effectively use plasmons to perform chemical reactions, a greater understanding of the decay mechanisms, energy or electron transfer pathways, and the lifetimes of various processes is required. A major goal in the development of new ultrafast SERS methodologies is to quantitatively measure these processes. Here we discuss what is currently known about molecule-plasmon interactions on the ultrafast time scale. In Figure 2.2, we depict likely decay pathways for an excited molecular-plasmonic system; however time scales are merely approximate and subject to change for specific systems.

Once excited, plasmons quickly decay and dissipate their energy via several pathways (Figure 2.2). The decay of the coherent plasmon, which results in the formation of hot electrons, is predicted to occur within approximately 10-100 fs due to electron-electron interactions.[45,46]

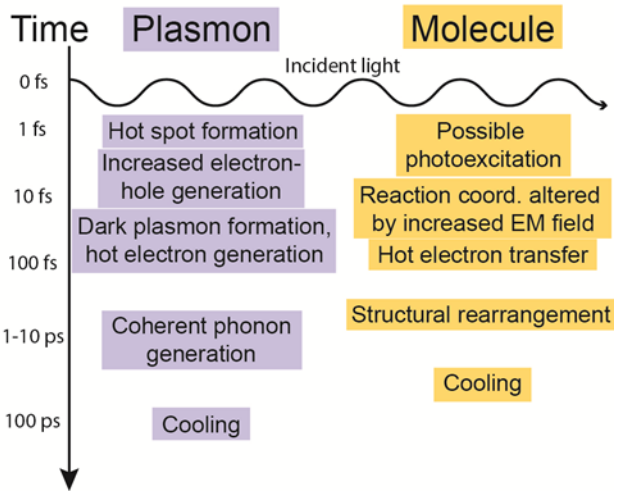

Figure 2.2 Approximate time scales of molecular-plasmonic interactions. Timescales are generalized and could vary by several orders of magnitude depending on the system.

Ejected hot electrons could have energies ranging from the Fermi level to the work function of the plasmonic material and are likely sufficiently energetic to drive chemical reactions in adsorbed analyte molecules.[10,47] Quantitative measurements of the lifetime and yield of these hot carriers are currently lacking, although numerous theoretical models predict their existence.[10,47,48] Within the nanoparticle, the initially coherent plasmon gas quickly becomes incoherent, and through interactions between the electrons and the metal phonons, forms a hot metal lattice with a lifetime of 1-10 ps.[49–51] The hot metal lattice then relaxes by coming to equilibrium with the surrounding environment through the release of excess energy as heat over the course of several hundreds of picoseconds to nanoseconds.[7,52]

Bright, or radiative, plasmons can also decay into dark, or non-radiative, plasmons.[53–57] Dark plasmons exhibit no overall dipole moment, precluding their interaction with plane wave excitation sources. In single nanoparticles, dark plasmons are

typically associated with quadrupole or higher multipole modes. In aggregated particles, dark plasmons arise when the individual plasmons associated with single nanoparticle dipoles interact to yield no net dipole moment, creating a dark mode similar to an anti-bonding orbital. Because they cannot be directly excited by incident radiation and experience minimal radiative damping, dark plasmons exhibit longer lifetimes than their bright counterparts. They are also localized in different regions on the nanoparticle and are not visible in extinction spectra or other far-field measurements.[56] Due to their longer lifetimes, dark plasmons have more time to interact with nearby molecules, potentially leading to more efficient plasmon-driven processes. As a result, when formed, dark plasmons are promising avenues of plasmonic research in areas such as plasmon-induced chemistry.

Molecules placed near the hot spots of plasmonic structures may be affected by plasmonic excitations in several ways; however, the precise nature of the interplay between plasmons and nearby molecules is not well understood. Depending on the analyte of interest, the molecule may be photoexcited in the first few femtoseconds after light irradiation independent of the plasmonic excitation. Furthermore, the potential energy surface of a reacting molecule may be rapidly altered due to the intensity of the electric field in these regions, opening the possibility of accessing new reaction coordinates. Additionally, the hot electrons generated on the plasmonic material are transferrable to adsorbed molecules on the femtosecond time scale, which may be used to drive chemical reactions. Due to these plasmonic effects, the molecule could ideally undergo structural rearrangement on the femtosecond and picosecond time scale.

The techniques discussed in Section 2.3 have the potential to further elucidate plasmonic-molecular interactions, leading to the development of plasmon-mediated chemistry and increased sensing possibilities. Ultrafast Raman spectroscopy forms the common element of all discussed techniques because it allows for the observation of molecular structure through the vibrations of the molecule and changes in structure due to interaction with the plasmon. These structural changes are observed through shifts in the vibrational frequencies of the Raman active modes for a molecule. Ultrafast laser pulses allow for data acquisition on the time scales of the plasmonic and molecular lifetimes, generating "molecular movies" for the course of a reaction. Recently, stimulated Raman techniques have been combined with SERS, increasing the sensitivity of these time-resolved techniques. As a result, LSPR-driven electromagnetic field enhancement can be used to both observe molecular vibrations through SERS as well as drive chemical reactions through hot electron transfer to analyte molecules.

2.2.3 How does ultrafast spectroscopy probe molecular-plasmonic interactions?

Ultrafast spectroscopies are generally considered to be those which probe systems on the picosecond or femtosecond time scale. Given that molecular vibrational frequencies range from ~100 cm^{-1} to 3000 cm^{-1}, this time scale is comparable to the period of vibrational motion (from 333 fs to 11 fs). Thus, in order to use real-time monitoring of bond-breaking and -making processes induced by plasmons, ultrafast spectroscopies are required.

In this review, we consider ultrafast Raman spectroscopies, due to the strong enhancement of Raman spectroscopy by plasmonic fields, as described above. Time-

resolved spontaneous Raman spectroscopy is subject to the time-energy bandwidth product, meaning that there is an inverse relationship between spectral resolution and temporal resolution. In these spectroscopies, time resolution on the order of several picoseconds results in Raman linewidths of tens of cm^{-1}, which is sufficiently fast to observe some but not all of the relevant dynamics.

Stimulated Raman spectroscopies have the ability to extract structural information on time scales shorter than several picoseconds and, in some cases, can provide information on reaction dynamics on the 10s of femtosecond time scale. In this review, we consider two forms of stimulated Raman spectroscopies: femtosecond stimulated Raman spectroscopy (FSRS),[58,59] and coherent anti-Stokes Raman spectroscopy (CARS)[60,61]. Both of these spectroscopies involve the interaction of two or three ultrafast laser pulses and vibrational modes in the sample of interest. When coupled with a femtosecond excitation pulse, such as that indicated in Figure 2.2, these spectroscopies can be used to monitor chemical change in molecular-plasmonic systems.

2.3 Novel ultrafast SERS methods to monitor molecular-plasmonic systems

Here we highlight three different ultrafast SERS techniques, which emphasize the range of technical capabilities possible with these methods, including single molecule and time-resolved measurements.

2.3.1 SE-FSRS

SE-FSRS is a novel spectroscopic technique created by combining FSRS and SERS. FSRS allows for the vibrational dynamics of a system to be monitored over time, creating "molecular movies" of the evolution of the system. A drawback to this technique is that samples need to have high Raman cross sections or be highly concentrated to produce a strong FSRS signal. Adding surface enhancement to the FSRS process provides a significantly more intense spectral signal from fewer molecules, enabling the study of molecular-plasmonic interactions on the femtosecond time scale.

Previous attempts to couple stimulated Raman techniques with the surface enhancing capabilities of plasmonic materials were troubled by issues involving sample degradation. A SE-FSRS experiment by Gilch *et al.* convincingly demonstrated that particles aggregated by ionic interactions are not stable under irradiation from high energy, kHz repetition rate femtosecond pulses.[62] In these systems, the particles likely undergo rapid melting or de-aggregation, which surprisingly seems to occur on a time scale faster than vibrational signal generation.

SE-FSRS was demonstrated successfully through the use of higher repetition rate and lower peak power lasers, which enabled the clear generation of SE-FSRS signals with rapid acquisition times. Figure 2.3 shows the SERS intensity spectrum of *trans*-1,2-bis(4-pyridyl)-ethylene (BPE) on 100 nm gold nanoparticles encased in silica (red) as well as the SE-FSR spectrum (black).[63] The peaks in the SE-FSR spectrum show dispersive lineshapes where conventional SER spectra show Lorentzian lineshapes.

Dispersive lineshapes are not uncommon in stimulated Raman spectroscopies and can also be found when the Raman pump is on resonance with an electronic transition of the system. In this case, the dispersive features result from interactions of the plasmonic nanoparticles and the vibrational coherence used to generate the Raman signal.[64] The SE-FSR spectra show high degrees of spectral (20 cm^{-1}) and temporal (10-100 fs) resolution, and convincingly demonstrate that ultrafast stimulated Raman spectroscopies can be successfully adapted to plasmonically-enhanced nanoscale environments.

Determining the exact EF of the SE-FSRS process is a crucial factor in the overall sensitivity of this method. As with many SERS EF calculations, the exact determination in this experiment is hindered by uncertainty in the number of molecules participating in the Raman process. The EF is estimated to be between 10^4-10^6 when assuming a monolayer surface coverage, less than the 10^8 enhancement found in SERS experiments on the same samples.[63,65]

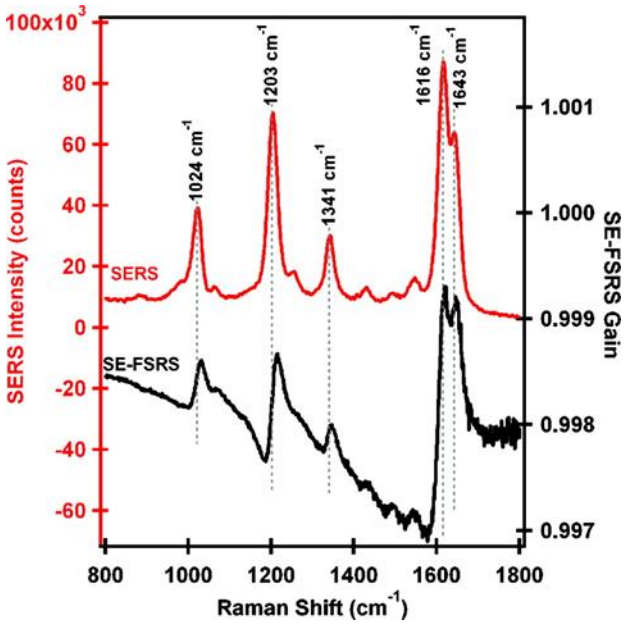

Figure 2.3 Proof of principle surface-enhanced femtosecond stimulated Raman spectra. In red is the spontaneous SER spectrum of the bis-pyridyl-ethylene nanoantennas, and in black is the SE-FSR spectrum. The two techniques show isoenergetic features, although the lineshapes are dispersive in SE-FSRS. Figure reproduced with permission from reference [63].

This discrepancy is likely due to particle degradation, as the authors found significant

changes in the LSPR over the course of the experiment, demonstrating a change in the plasmonic properties of the material. However, it is clear that high signal-to-noise ratio spectra are easily achievable with this technique.

The clear success of coupling plasmonic materials with femtosecond stimulated Raman techniques forms a first step towards monitoring plasmonically-induced photochemical and photophysical processes. SE-FSRS shows great potential in determining system mechanisms and intermediates that have low signals and short lifetimes that are not able to be detected by other methods, significantly increasing the number of systems and fields of study that can be explored.

2.3.2 SE-CARS

CARS is a stimulated Raman technique similar to FSRS, which involves the interaction of 2 to 3 laser beams and provides anti-Stokes Raman information in a coherent beam of emitted light. While CARS can suffer from interferences from electronic signals, termed the "non-resonant background", it has been highly useful in imaging and materials characterization.[60] Several attempts have been made to couple the CARS processes with the surface-enhancing capabilities of plasmonic materials, with historical enhancement factors on the order of 10^3.[66,67]

A more recent experiment by Halas *et al.* demonstrated SE-CARS with single molecule and single particle resolution.[68] This extraordinary sensitivity was achieved with a carefully designed plasmonic substrate consisting of a quadrumer of four Au disks evaporated onto a silica support. Once prepared and characterized, small molecules were introduced to the substrate to determine the EF, which was 10^5 relative to CARS without surface-enhancement. When compared to spontaneous Raman, an EF of 10^{11} was observed. A bi-analyte experiment was performed with p-aminothiophenol (*p*-MA) and adenine, which were used in the previous ensemble measurements, to obtain single molecule data. As bianalyte rather than isotopologue measurements were performed to prove single molecule behavior, the authors of this study did careful surface adsorption measurements to ensure differences in molecular binding affinities did not affect the statistics. As shown in Figure 2.4, three different

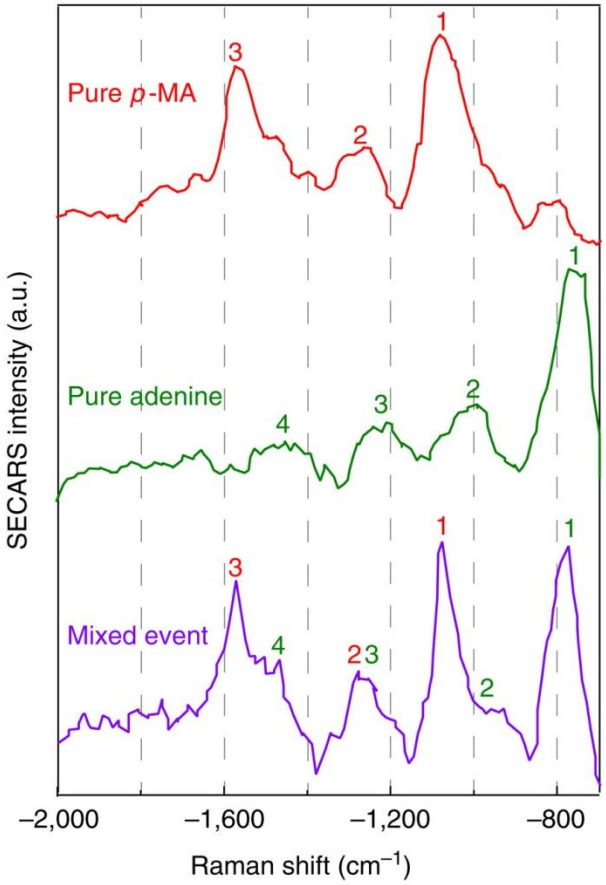

Figure 2.4 SE-CAR spectra depicting single molecule detection via the bianalyte method. The top two spectra show each analyte individually and the bottom spectrum is representative of the presence of both analytes. Figure reproduced with permission from reference [68].

spectra were observed. The spectra either contained peaks associated with only one of the analytes or a combination of peaks from both analytes. With the observed enhancement, the Halas group demonstrated the analytical potential of this technique when an appropriately enhancing substrate is used.

2.3.3 TR-SE-CARS

Both the SE-FSRS and SE-CARS experiments discussed thus far have been ground state measurements, with the undemonstrated potential of coupling these measurements with direct photoexcitation to follow the ultrafast dynamics of the molecular-plasmonic system. The next example, which we term TR-SE-CARS, is a true breakthrough in extracting femtosecond information from a CARS measurement. While not an example of a photoexcited system, femtosecond dynamics corresponding to molecular vibrations were obtained at the single particle and possibly single molecule level.

The recent demonstration of TR-SE-CARS allows for direct observation of molecular vibrations in real time.[69] Measurements of this type were made possible by utilizing the robust sample architecture used in the SE-FSRS experiments described in Section 2.3.1, in which analyte molecules (BPE, as in the SE-FSRS experiments) were adsorbed to gold nanoparticle dimers and then encapsulated in silica. This allows for SERS signals from single dimer particles to be reliably obtained over long time periods using intense ultrafast laser pulses without significant sample damage. Single particles immobilized on a TEM grid substrate were examined by TR-SE-CARS, in which Raman-

active vibrations were excited by a pump pulse pair and then probed at a later time using a single probe pulse (Figure 2.5a). Through proper tuning of the frequencies of the pump and Stokes pulses used to generate the TR-SE-CARS signal, the authors were able to excite multiple Raman-active vibrations of BPE. This resulted in a signal that oscillated in time due to the quantum beating of the closely-spaced excited vibrational modes (Figure 2.5b). This oscillatory signal appeared on top of a non-resonant background, which likely arose from the plasmonic response of the nanoparticle structures. While rigorous separation of the plasmonic and molecular responses is not trivial due to the extent of molecule-plasmon coupling being not well understood, the authors were able to extract and analyze the oscillatory features of the spectra.

In addition to forming an important demonstration of femtosecond time-resolved SERS, the authors were able to show evidence that some of the oscillatory TR-SE-CARS signals were suggestive of single molecule behavior through statistical analysis of the dephasing present in each signal. Whereas TR-SE-CARS signals from bulk BPE exhibit rapid dephasing back to zero signal (Figure 2.5c), the TR-SE-CARS signals from single dimer particles did not (Figure 2.5d). This behavior can be related to the number of molecules generating the signal through analysis of the average signal level at long delay time $\langle S(\tau \to \infty) \rangle$, which can be described by

$$\langle S(\tau \to \infty) \rangle = \frac{1}{NV}$$

where N is the number of particles and V is the number of vibrational states being excited. Through examination of the probability distribution function (PDF) of the

amplitude of each signal, with knowledge of *V*, assignments of *N* can be made with statistical certainty based on the moment of the signal PDF. As shown in Figure 2.5e, simulated TR-SE-CARS signals for one and two molecules show statistically different moments, with $\langle S(\tau \to \infty) \rangle = \frac{1}{2}$ for $N = 1$ and $\langle S(\tau \to \infty) \rangle = \frac{1}{4}$ for $N = 2$. Similar analyses of experimental signals allow for assignment of *N*, which in some cases confirmed single molecule behavior. It should be noted that single molecule behavior in this case was confirmed only through analyses of TR-SE-CARS traces as opposed to more commonly employed isotopic methods of confirmation, which are challenging under the experimental conditions employed in this work.[70]

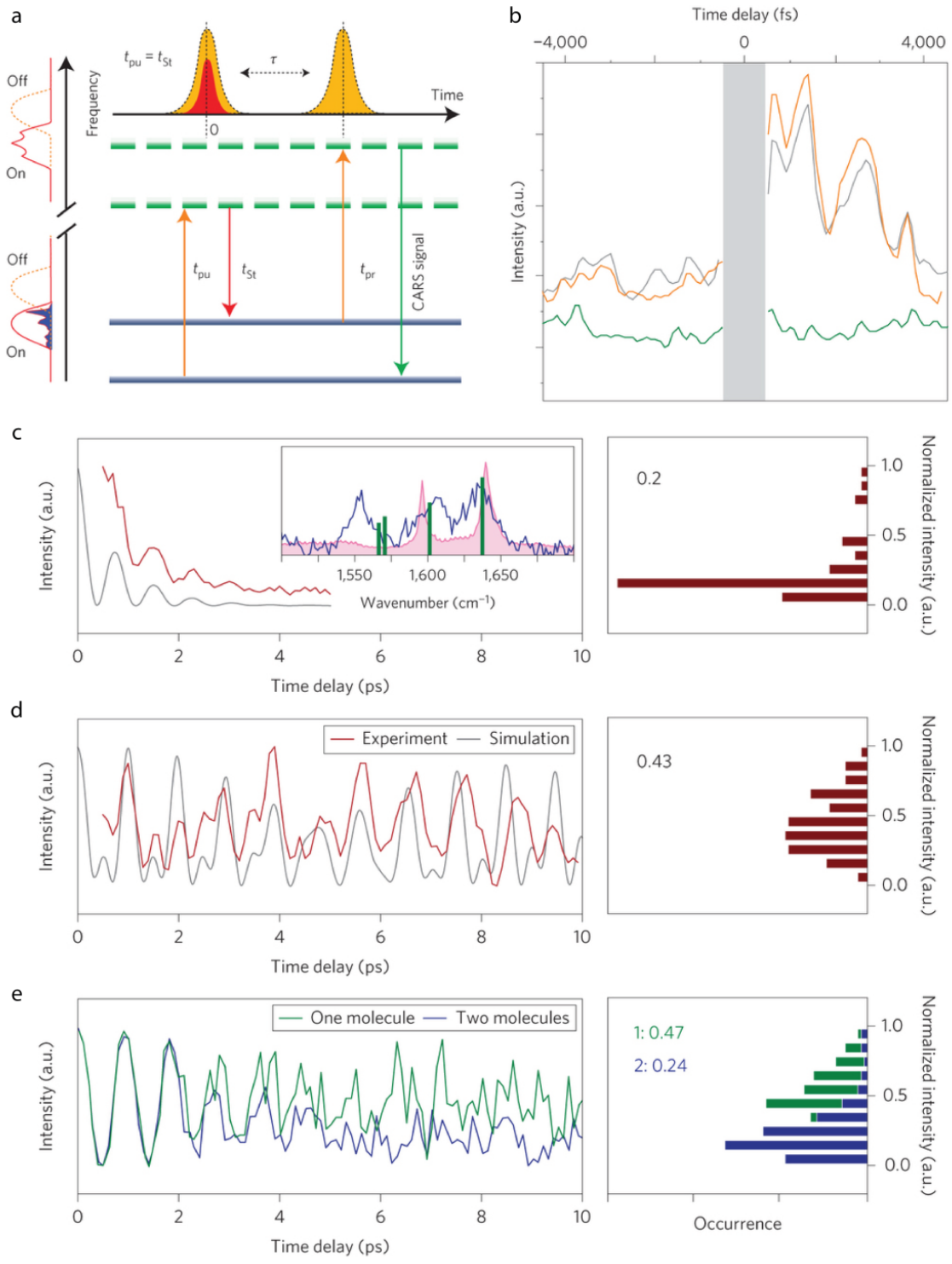

Figure 2.5 TR-SE-CARS set-up and spectra **a.** Jabolonski diagram of the pump pair and probe pulses **b.** TR-SE-CAR spectra from SERS-active (orange and gray traces) and non-

SERS active (green trace) substrates **c.** damped quantum beating of vibrational modes in bulk BPE obtained by TR-SE-CARS (brown curve) and windowed Fourier transform of bulk BPE Raman signal (grey curve). The right panel shows the probability distribution function and moment of the brown curve. Inset shows TR-SE-CAR spectrum (blue curve), bulk BPE Raman spectrum (pink curve), and stick spectrum used for simulations **d.** TR-SE-CARS signal from a single dimer (brown curve) compared to simulated signal for stick spectrum in inset of c (grey curve). The PDF and moment of the experimental trace appears in the panel on the right **e.** simulated TR-SE-CARS signals for one molecule (green curve) and two molecules (blue curve). The panel on the right shows PDFs and moments of both traces. Figures reproduced with permission from reference [69].

The combination of SERS with time-resolved measurements, including FSRS and CARS, is needed in order to study plasmon-mediated chemical reactions. The increased signal and resolution offered by the surface-enhanced techniques as well as the ability to collect spectra on the time scale of the reaction allow for the collection of data for unstable intermediates which may not be visible to similar techniques. Additionally, TR-SE-CARS would not only make it possible to study plasmon-mediated reactions as an ensemble but potentially offer the ability to observe how one molecule reacts when it is near a plasmonic hot spot.

2.4 Future Prospects/Applications

2.4.1 Plasmonic Processes

The development of the stimulated and time-resolved surface-enhanced Raman methods described above open a new door into the ability to follow plasmon-induced photochemical and photophysical processes in real time. The ability of plasmons to concentrate light, generate highly energetic electrons and holes, and drive new chemical processes is leading to exciting research in coupling these novel methods with various

chemical systems. Here we highlight a few of the future possibilities for SE-CARS and SE-FSRS.

2.4.1.1 H_2 dissociation

Recently, hot electrons generated by exciting plasmonic gold nanoparticles were used to dissociate H_2, which is typically an extremely energetically unfavorable reaction. Plasmon-mediated H_2 dissociation is a light driven reaction, which occurs at ambient conditions.[71,72] The photocatalytic power of plasmons towards heterogeneous catalysis and energy applications is quite appealing, however there remain significant questions as to the relative roles of hot electrons, light scattering, localized heating, and surface chemistry in these processes.

Determining the mechanism by which plasmon-mediated chemistry occurs is vital towards truly harnessing the power of plasmonic photocatalysts. The proposed mechanism for H_2 dissociation involves sufficiently energetic hot electrons populating an anti-bonding orbital of H_2, resulting in a broken H-H bond. Similarly, D_2 is dissociated and recombines with dissociated H_2 to form HD at a sufficiently high concentration to be quantified with a quadrupole mass spectrometer (QMS).[71] QMS detection allows for the determination of rate constants for this reaction, however it lacks sufficient time resolution and sensitivity to monitor the formation of the unstable intermediates proposed in this mechanism. The time-resolved SERS techniques described above could allow for data acquisition at each point in this photocatalytic process, providing molecular snapshots for each step of the mechanism. The structural information at relevant time

scales obtained by time-resolved SERS will show how molecules react near hot spots, providing many new avenues in plasmonic research and applications.

2.4.1.2 Solar Steam

An additional future application of time-resolved SERS lies in elucidating the mechanism of the recently reported plasmonically-driven steam evolution from liquid water. Irradiation of solutions of nanoparticles in water with focused sunlight has been shown to result in highly efficient steam generation,[3] with promising utility in off-grid applications requiring steam production, such as waste sterilization.[73] This process has been shown to yield steam generation with over 80% energetic efficiency without the need to heat the entire solution volume to its boiling point. The mechanism is believed to entail light trapping by nanoparticles in solution, in which multiple nanoparticle scattering processes followed by nanoparticle absorption results in localization of incident light into a small volume. This yields a compact and nanoscale heat source.[74] However, the temperature rise experienced by the solvent molecules immediately surrounding the nanoparticle and the relative role of collective versus individual nanoparticle heating is still unclear. Additionally, the precise location of vapor nucleation is currently unknown,[75] with the shape and spatial distribution of nanoparticles both believed to be important.

Understanding of the precise mechanism of solvent vaporization on nanoparticle surfaces will undoubtedly benefit from the ability of time-resolved SERS to shed light on the ultrafast time scales that govern energy relaxation from nanoparticles into their surroundings. Furthermore, time-resolved SERS can also be exploited to give information

on the instantaneous temperature of the solvent immediately surrounding the nanoparticle through comparison of Stokes and anti-Stokes Raman spectra. This would greatly assist in elucidating the precise temperature rise of the solvent layer immediately surrounding the nanoparticle and aid in future design considerations for more efficient solar steam generation.

2.4.2 Sensing applications

The novel ultrafast SERS methods described in Section 2.3 have been developed primarily for studies of plasmon-induced photochemical and photophysical processes, but also could have significant potential for SERS sensing applications. As SE-FSRS and SE-CARS involve coupling stimulated Raman processes with surface enhancement, they have the advantage of coherent signal generation, along with the possibility of field enhancements beyond the E^4 limit as described in Section 2.2.1.

Stimulated Raman techniques are fundamentally different than the spontaneous Raman techniques traditionally used for SERS. They are two-pulse techniques in which the first pulse induces an upward transition in the molecule from the ground state. The second pulse, which matches the frequency of the Raman shifted photon, stimulates a downward transition. Stimulated Raman therefore increases the probability of Raman scatter compared to spontaneous Raman. Furthermore, the stimulated Raman signal is coherent, meaning it is emitted in a beam-like fashion. This means that every Raman photon can in principle be collected, as opposed to spontaneous Raman signals in which photons are typically scattered in many directions and only a small solid angle is

collected. When approaching the limit for single molecule detection, the coherent nature of stimulated Raman scattering may enable greater sensitivity due to greater collection efficiency.

An unexplored area of SERS sensing involves the potentially higher EFs of stimulated Raman spectroscopies as opposed to spontaneous Raman spectroscopies. As discussed in Section 2.2.1, spontaneous SERS EFs depend roughly on E^4, where E is the applied electromagnetic field. In two and three pulse stimulated Raman spectroscopies, the EF may consist of contributions of multiple enhanced electromagnetic fields. In that case, the SERS EF could, in principle, scale as E^6 or even E^8, in which E represents contributions from the multiple applied electromagnetic fields. This higher order enhancement has yet to be seen experimentally, due to difficulties with sample heterogeneity and breakdown at high fields.. As researchers seek to sense broad classes of compounds at the single molecule level with SERS, the possible higher order enhancements of stimulated SERS processes, including SE-CARS and SE-FSRS, could represent an exciting path towards greater sensing sensitivity at low concentrations.

2.5 Conclusion

This review discussed recent developments in ultrafast SERS methodologies, with applications to plasmon-mediated chemical reactions and highly sensitive sensing technologies. We highlighted the need for ultrafast SERS methods by considering the time scales of relevant molecular-plasmonic interactions, with implications for understanding reaction dynamics in numerous light-driven chemical and physical processes. Advances in this area in the past several years have been made by coupling stimulated Raman methods, such as FSRS or CARS, with the surface-enhancing capabilities of plasmonic materials. More recent work has shown the applicability of these techniques to femtosecond time scale measurements, through the demonstration of single molecule TR-SE-CARS. These new techniques open a wide range of systems to study, such as plasmon-mediated H_2 dissociation and solar steam production, as well as opening new avenues for sensing applications. Ultrafast SERS techniques have great potential to further our understanding of plasmonic systems and elucidate mechanisms for plasmon-induced chemical reactions.

Chapter 3

Monitoring Charge Density Delocalization upon Plasmon Excitation with Ultrafast Surface-Enhanced Raman Spectroscopy

Reprinted with permission from the manuscript by Emily L. Keller, and Renee R. Frontiera *ACS Photonics* **2017**, *4*, 1033-1039

3.1 Synopsis

Plasmonic materials hold a great deal of potential for advances in energy and chemical applications by converting light into chemical energy. Many of these processes are aided by plasmon-generated hot electrons. However, the interaction between these hot electrons and adsorbed molecules on a plasmonic substrate is not well understood. Using ultrafast surface-enhanced Raman spectroscopy, we monitor plasmon-molecule interactions in real time using 4-nitrobenzenethiol as a molecular probe. Upon plasmon excitation, we observe transient peak depletions in our ultrafast surface-enhanced Raman spectra on the picosecond timescale. We attribute this peak depletion to a localized surface plasmon resonance red shift as a result of hot electron generation in our aggregated nanoparticles. Once generated, the hot electrons delocalize across the aggregate. By correlating the magnitude of the transient Raman dynamics with the degree of electron delocalization, we estimate charge displacement on the order of 10^9 electrons per aggregate. This indirect quantification of hot electron delocalization on aggregated nanoparticles will be of use in the rational design of materials for efficient plasmon-driven photochemistry.

3.2 Introduction

Plasmonic materials offer many avenues for the conversion of light energy into other forms of energy, including chemical energy or heat. Many current applications take advantage of this conversion, including photovoltaics devices,[1,76,77] photothermal cancer therapies,[2,78] and photochemistry and photocatalysis.[22,44,71] However, the direct mechanisms, rates, and efficiencies by which plasmons enhance these applications are

not well understood. To improve the efficiency and applicability of plasmon-driven processes, we need a better understanding of how the interaction between light and plasmonic materials results in various pathways of energy conversion.

Light energy conversion on plasmonic materials begins by shining light on the plasmonic material to excite a localized surface plasmon resonance. A localized surface plasmon resonance (LSPR) is the collective oscillation of electron density on the surface of a plasmonic material, which is formed upon excitation by an electromagnetic field. This oscillation concentrates the electromagnetic field in a small area, such as between gaps of two or more plasmonic nanoparticles. After excitation, the electron-electron scattering dampens the plasmon excitation in 10-100 fs.[9,79,80] The electron-electron scattering results in electron thermalization, generating highly energetic electrons, or "hot" electrons, with energies ranging between the Fermi level and the work function of a plasmonic material.[10] These hot electrons can either transfer to nearby molecules on the nanoparticle surface, potentially driving chemical processes, or they can undergo electron-phonon scattering, which occurs in 1-10 ps.[7,47] Interactions between hot electrons and phonons lead to a hot lattice of the plasmonic material, which reaches equilibrium with the surrounding environment in >100 ps.[7,9] However, experimental evidence for the number of hot electrons generated upon plasmon excitation as well as the likelihood for hot electrons to drive chemical change as opposed to transferring back into the plasmonic material is lacking.

A great deal of experimental work attempts to address how plasmon excitation and decay affects the plasmonic material and potential adsorbed molecules on the

surface. Due to the rapid timescales involved, ultrafast spectroscopic measurements are commonly employed. Transient absorption studies have typically focused on plasmon dynamics of metal nanoparticle monomers and aggregates on the picosecond and femtosecond timescale. Upon plasmon excitation, the plasmon resonance of the metal nanoparticle bleaches due to the generation of hot electrons. These hot electrons decay within 1 to 7 ps through electron-phonon scattering. [49,79,81–83] However, these measurements generally do not take into account potential plasmon-molecule interactions. Recently, plasmon-driven H_2 dissociation on gold nanoparticles demonstrated the possible application of plasmonic materials for photochemistry.[71,72] Although these studies could not track the H_2 dissociation mechanism on the timescale of plasmon dynamics, the authors hypothesized that hot electrons generated upon plasmon excitation drove the H_2 dissociation. However, the number of hot electrons generated and their distribution on a plasmonic substrate is currently unknown. Further mechanistic studies, on the timescale of plasmon dynamics, may elucidate why these plasmonic photochemical processes are successful and offer insights on how they may be improved.

To answer these questions, we study plasmon-molecule interactions on the picosecond timescale using ultrafast surface-enhanced Raman spectroscopy (SERS). SERS is a plasmon-driven technique which enhances Raman signal by interactions between the laser excitation electromagnetic field and the resulting Raman scattering electromagnetic field with the electromagnetic field of the plasmonic material. The Raman signal primarily is generated from molecules in hot spot regions and thus is sensitive to the most active regions of the plasmonic substrate. In ultrafast SERS,

plasmon excitation is initiated with a femtosecond pump pulse, and the subsequent molecular dynamics are interrogated with a picosecond SERS probe pulse.[11] A time delay between the two pulses allows us to probe the system at various times before and after plasmon excitation. These different time traces generate a 'molecular movie' of the examined system. Ultrafast SERS is thus a method of probing the molecular response to plasmon excitation on the timescale of molecular vibrations and chemical changes. Here, we show the plasmon-molecule interactions, which arise upon plasmon excitation, resulting in a change in the charge density of the nanoparticle aggregates arising from hot electron generation. We estimate the number of hot electrons affected per aggregate upon plasmon excitation and suggest possible mechanisms driving the change in charge density.

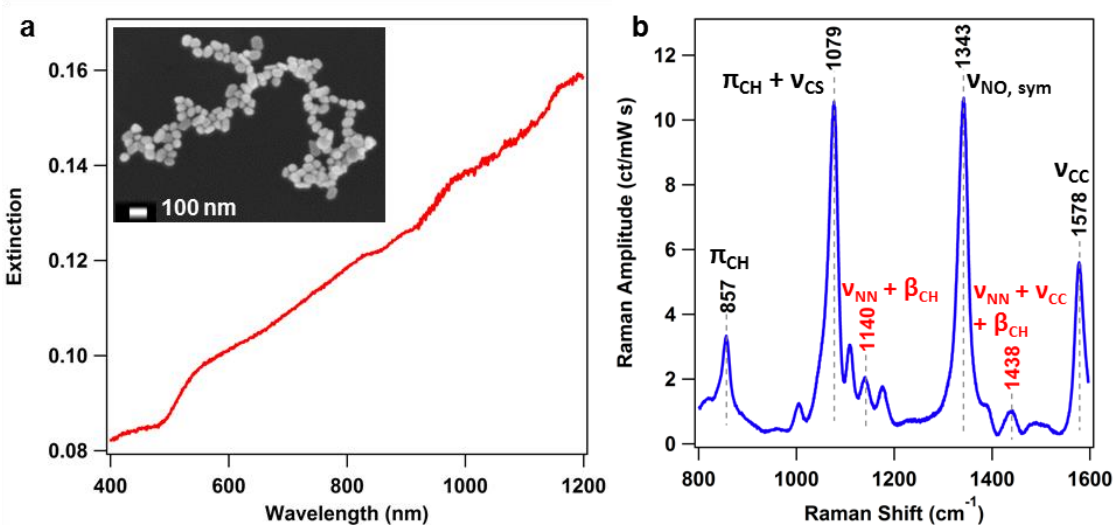

Figure 3.1 (a) Extinction spectrum of colloidal gold nanoparticle aggregates used for ultrafast SERS. The inset is a scanning electron micrograph of the gold nanoparticles which have a diameter of 70 ± 10 nm, measured from the micrograph by ImageJ software. (b) SER spectrum of aggregated gold nanoparticles with 4-nitrobenzenethiol (black labels) and dimercaptoazobenzene (red labels) adsorbed to the surface. The symbols, ν, β, and π represent stretching modes, bending modes and ring breathing modes, respectively. The two main peaks at 1343 cm^{-1} and 1079 cm^{-1} are associated with the NO_2 stretch and ring breathing of the 4-nitrobenzenethiol, respectively.

3.3 Results and Discussion

The plasmonic samples used for our ultrafast SERS measurements are gold colloidal nanoparticles synthesized via the Frens method.[84] The average size of the individual gold nanoparticles is 70 ± 10 nm, measured by SEM using ImageJ software (inset, Fig. 3.1a). The addition of salt (KNO_3) drives the aggregation of the nanoparticles via electrostatic interactions, generating a sample with a broad LSPR optimized for Raman probing at 1035 nm. This aggregation method leads to a heterogeneous sample with a wide range of aggregate sizes due to the number of individual nanoparticles within each aggregate, shown by the extinction spectrum in Figure 3.1a. These aggregated particles contain reporter molecules of 4-nitrobenzenethiol (4-NBT) and 4,4'-dimercaptoazobenzene (DMAB). The plasmon-driven conversion of 4-NBT to DMAB is a well-studied reaction.[85,86] In our samples, the hot spots capable of dimerizing 4-NBT do so prior to our measurement when exposed to ambient light.[11] During our ultrafast SERS measurements, the concentrations of 4-NBT and DMAB are essentially static and further irradiation does not drive any conversion of 4-NBT to DMAB. Figure 3.1b shows a continuous wave SER spectrum of these analytes adsorbed onto the aggregated gold nanoparticles. The main 4-NBT modes, denoted in black, are a ring breathing mode at 857 cm^{-1}, a ring breathing mode with additional CS stretching character at 1079 cm^{-1}, symmetric NO_2 stretch at 1343 cm^{-1}, and CC stretch at 1578 cm^{-1}. Two DMAB modes, shown in red, are modes with NN stretch character at 1140 and 1438 cm^{-1}.[87,88] The overall population of DMAB in this sample is significantly lower than 4-NBT, as can be

seen in the ratio between the peaks in Figure 3.1b, thus we focus our analysis on the more prominent 4-NBT peaks.

In Figure 3.2a, we present ultrafast SER spectra, which probe the ultrafast response of this molecular plasmonic system. The bottom spectrum is a pump-off spectrum, and transient spectra between -5 and +50 ps are displayed with a vertical offset. The transient spectra are presented as difference spectra, in which a -50 ps spectrum is subtracted from each time point.[11] This subtraction procedure eliminates any pump-induced scattering in the transient spectra, and as the pump pulse at -50 ps time delay comes in well after the probe pulse, the transient dynamics are preserved.

The transient spectra show significant peak depletions, as clearly seen for the main vibrations in 4-NBT at 1079 and 1343 cm^{-1}, corresponding to the ring breathing and the NO_2 symmetric stretch, respectively. The depletions for all peaks are maximized around time zero, where both the pump and probe pulses interact with the sample at the same time, and decay on a picosecond timescale.

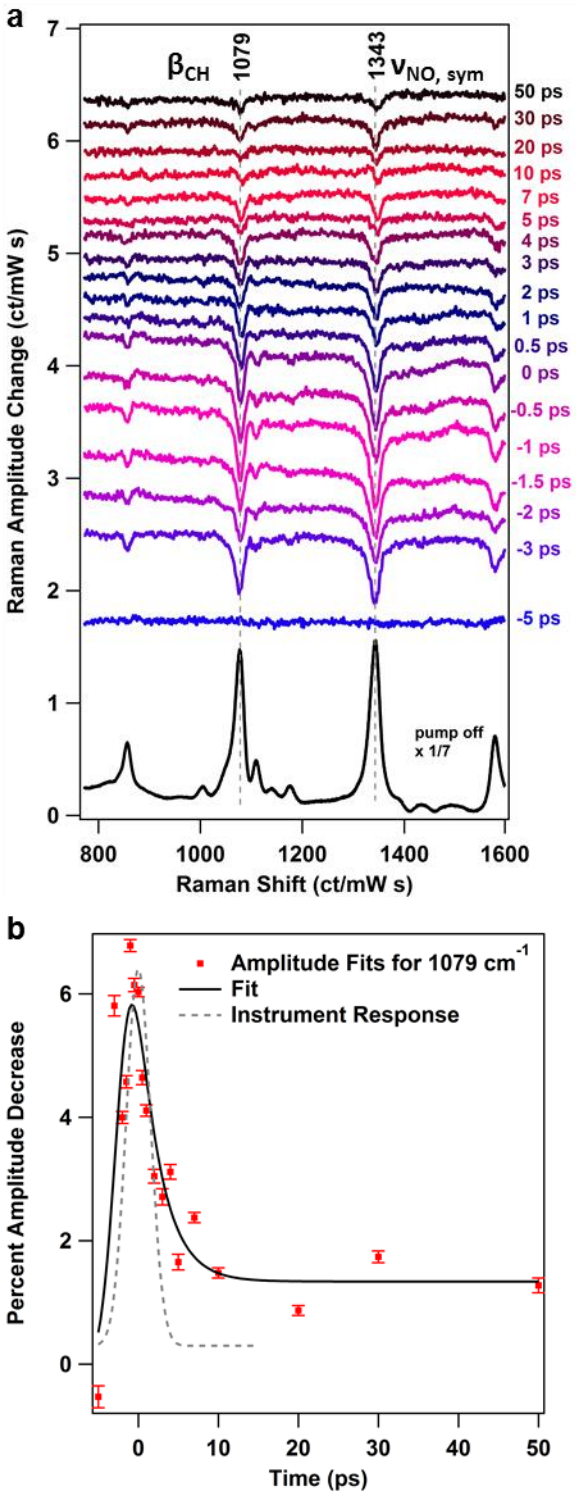

Figure 3.2 (a) Ultrafast surface-enhanced Raman difference spectra obtained upon excitation with 1.22 nJ of 1035 nm pump

pulse, resulting in a transient signal decrease for 4-nitrobenzenthiol modes. (b) convolved fit of 1079 cm^{-1} amplitudes from (a) and instrument response which yields a lifetime of 2.8 ± 0.2 ps for the transient peak depletion.

We fit the peak depletions for 1079 and 1343 cm^{-1} with Gaussian lineshapes to track the kinetics of the transient bleach. These amplitudes are normalized to the peak amplitudes from the pump off spectrum to yield the values shown in Figure 3.2b. To obtain the lifetime for the peak depletions, we fit the amplitude fits to a convolution of an exponential function with the Gaussian instrument response function (Z(t)) with the addition of a sigmoidal function with an offset for later time points, as shown in Equation 3.1. Here A is the amplitude of the exponential fit, τ is the decay time, t is the time, x_0 is time zero offset, b is the Gaussian standard deviation, y is the magnitude of the offset, and σ is the slope of the sigmoidal function. The instrument response is the time-dependent response function of our system and is measured by the cross correlation of our pump and probe beams using the optical Kerr effect in benzene. The offset at later time points likely arises from damage to the nanoparticles, which then no longer produce detectable SERS signal. However, the signal eventually recovers in >100 ps as we do not observe permanent signal loss in SERS signal or changes in the sample LSPR after a completed scan. Figure 3.2b depicts the kinetic fit for the 1079 cm^{-1} peak from Figure 3.2a, which gives a lifetime of 2.8 ± 0.2 ps. Additional fits with lifetimes for 1079 and 1343 cm^{-1} modes at varying pump energies and wavelengths are located in Appendix A with lifetimes ranging from 1 to 5 ps (Figure A2-A5).

$$\text{Fit} = \left[A \times e^{\left[\frac{\tau^{-2} - \left(4b\tau^{-1}(t-x_0)\right)}{4b}\right]} + \frac{y}{1+e^{\frac{-t+x_0}{\sigma}}} \right] \otimes Z(t) \qquad (3.1)$$

Peak depletions in the ultrafast SER spectra may arise from several different phenomena. First, the 4-NBT peaks may become depleted upon conversion of 4-NBT to DMAB. However, we would expect to see positive peaks in our transient difference spectra for the DMAB modes, which are not observed. When the DMAB signal at 1140 cm^{-1} is sufficiently large, the DMAB peak is also depleted in the ultrafast spectra (Figure A2). It is also possible that peak depletions may arise from sample degradation of either the analyte or the nanoparticles. However, LSPR spectra and ground state SER spectra taken during the experiment do not show significant signal depletion from sample degradation, with changes of, at most, 5% during the course of seven hours of experimentation. Thus, the most likely explanation for the transient peak depletions in our ultrafast SERS measurement are a result of a transient shift in the LSPR. SERS signal magnitudes are dependent on the magnitude of the LSPR at both the laser excitation wavelength and the Raman scattering wavelength.[89] Based on the slope of the LSPR for the nanoparticle aggregates (Fig 3.1a), we can conclude that the LSPR red shifts in order to give rise to the peak depletion seen in the transient SER spectra. We suggest that the plasmon excitation drives the LSPR shift, thus the magnitude of the peak depletion should depend on the overlap between the LSPR and the excitation wavelength.

A study on the wavelength dependence of the peak depletion shows that the magnitude of the transient features depends on the LSPR magnitude at the pump wavelength. In Figure 3.3a, the magnitude of the depletion becomes larger as the wavelength increases. This trend correlates to the sample LSPR shown in Figure 3.3b, demonstrating increasing plasmon resonance magnitudes with longer pump wavelengths. Thus, the LSPR shift is dependent on how well the excitation pulse couples to the nanoparticle aggregate population. We conclude that plasmon excitation induces a shift in the LSPR spectrum, which results in the peak amplitude changes in the transient ultrafast SER spectra on the picosecond timescale.

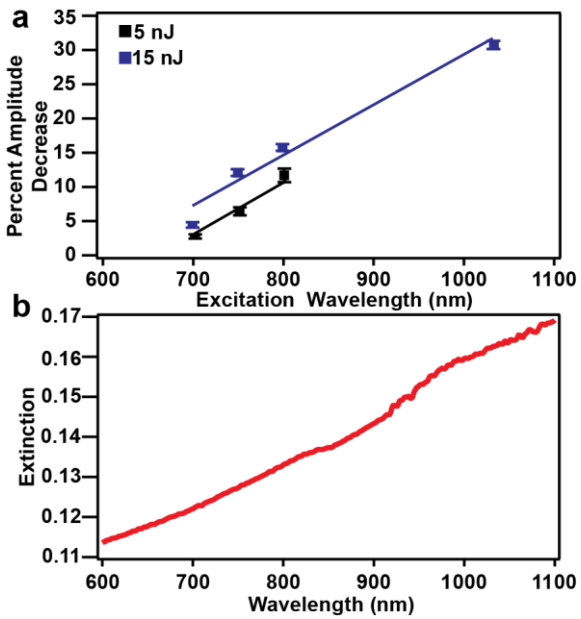

Figure 3.3 Pump wavelength dependence for transient peak depletion upon plasmon excitation (a) Maximum peak depletion at 5 and 15 nJ for pump wavelengths of 700, 750, 800 and 1035 nm. (b) LSPR of aggregated nanoparticle sample. The amplitude decrease magnitude correlates to the LSPR magnitude suggesting a strong dependence on the degree of plasmon excitation.

The LSPR red shifts as a result of plasmon excitation, however there are several possible physical explanations for the plasmon-driven shift. LSPR shifts commonly arise from changes in the plasmonic nanostructure shape or size.[89] However, based on the ultrafast timescale of the observed SERS amplitude changes, it is unlikely that this LSPR shift arises from photoinduced particle shape transformations. Another possible

explanation is a change in the aggregation of the nanoparticles, but it is unlikely that the particles could move instantaneously upon plasmon excitation as would be suggested by the transient signal depletion at time zero. Thus, the LSPR shift must arise from some change within or around the aggregate. A possible explanation is heating of the electrons due to plasmon excitation. Transient absorption studies on colloidal gold nanoparticles observed a similar LSPR bleach upon plasmon excitation.[49,79,82,90,91] In these studies, the authors attribute the bleach to hot electrons produced upon plasmon excitation through electron-electron scattering, which leads to a non-equilibrium distribution of highly energetic electrons. The hot electrons lead to a broadening of the LSPR and possible changes to the dielectric function of the nanoparticles, resulting in a red shift of the LSPR.[92,93] Thus, we conclude that the peak depletion seen in the transient SER spectra arises from perturbation to the electron density due to heating as a result of plasmon excitation.

The kinetics of the ultrafast SERS depletion as a result of an LSPR shift support the assignment to hot electron generation. These hot electrons quickly relax through electron-phonon interactions, with a lifetime for the electron-phonon coupling ranging from 1 to 7 ps.[9,79]. In Figure 3.2b, the kinetic fit for the peak depletion measures the electron-phonon scattering lifetime, which clearly lasts for several picoseconds. Additional lifetime measurements for various excitation wavelengths and powers are presented in Appendix A with additional discussion (Table A1-A3). Our lifetime measurements for the electron-phonon coupling agree with transient absorption measurements, which agrees with an LSPR red shift driven by electron heating.

Additionally, the electron-phonon scattering leads to a hot metal lattice. The hot metal lattice causes the particle to expand, which results in a decreased charge density for the particle. Transient absorption measurements have shown that the decreased charge density also leads to a red shift of the LSPR.[79] In SERS measurements, the hot metal lattice that arises from electron-phonon scattering may cause transient peak depletion features that persist much longer than 10 ps due to distortions of the hot spots. (Figure 3.2a). If the nanoparticles are expanding due to heating, then the transient SER spectra may be showing the distortion of the hotspot due to changing distances between nanoparticles, leading to the transient features present in later time points.

To investigate the magnitude of the SERS peak depletion, we also examined the effect of pump energies on the ultrafast signals. Figure 3.4 shows that the transient SERS bleaching magnitude increases linearly with increasing pulse energy. Figure 3.4a corresponds to data collected at a laser repetition rate of 2 MHz and shows peak depletion magnitudes increasing linearly between 15 and 75 nJ. Figure 3.4b corresponds with data collected at a laser repetition rate of 24.5 MHz with pulse energies below 6 nJ. The error bars account for differences across multiple samples measured at each pump power and are the standard deviation for the averaged percent amplitude decrease. Larger variance in error bars at higher pump energies arise from larger backgrounds for some of the spectra due to excess scattering from the pump beam. The peak depletion magnitudes show a linear dependence on pulse energy at both repetition rates, which suggests a one photon process.

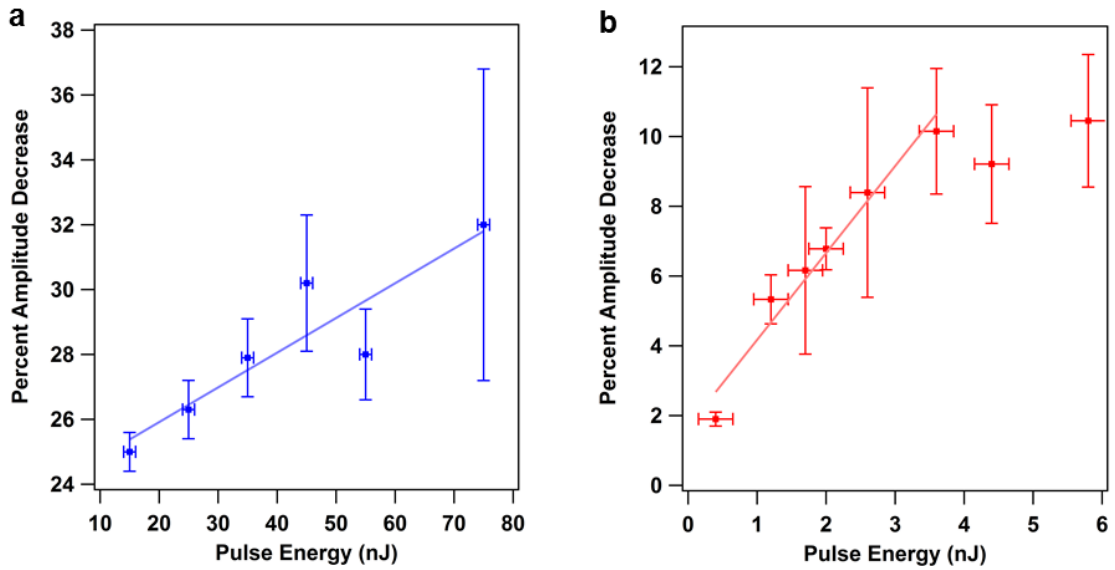

Figure 3.4 Power dependence at 1035 nm, maximum amplitude decrease vs pump pulse energy at (a) 2 MHz and (b) 24.5 MHz The power dependence is linear suggesting a one-photon process for plasmon excitation.

In Figure 3.4b, at pump pulse energies above 4 nJ, the peak depletion dependence on power changes, appearing to reach a saturation point. This saturation point may imply that there is a limited number of plasmon excitations that a given plasmonic nanoparticle aggregate can support. We can use the magnitude of the LSPR shift to approximate this threshold after making several assumptions, which are detailed further in Appendix A. First, the plasmonic nanoparticle aggregate is resonant at 1035 nm with an estimated radius of ~150 nm from Mie scattering, which based on random packing of spheres within a sphere[94] would suggest that ~50 Au nanoparticle monomers of an average radius of 35 nm are associated with one aggregate. This is an ensemble-averaged approximation. Then, we determine the number of photons per pulse from the pump energy at the saturation point and the repetition rate of the laser. Using this value, we estimated the number of photons per aggregate from the concentration of aggregates in the irradiated

volume. The sample concentration was determined by comparing the monomer peak in the aggregated sample extinction spectra to a calibration curve generated from the extinction spectra of the monomer Au nanoparticles at various known concentrations (Figure A6). At this point, we also assume that there is a possibility of plasmon re-excitation during one pulse interaction, due to the long pulse duration relative to the plasmon lifetime. However, we also must take into account the refresh rate of the aggregates moving in to and out of the irradiated volume, since these are solution phase samples that are stirred. Based on our sample concentration, laser spot size, and the spinning of the stir bar, we assume the nanoparticles in the spot size refresh between pulses at a rate of 1-8 particles/pulse. From these calculations, we estimate that up to 10^{11} photons drive plasmon excitation in a single gold nanoparticle aggregate before saturation. Any additional photons do not lead to an increase in plasmon excitation magnitude. Due to the heterogeneity of the sample, we only report an order of magnitude for these values due to the number of assumptions made in this estimate. This surprisingly large estimate suggests that it should be possible to generate a large population of hot electrons even if the quantum efficiency for hot electron generation in these aggregates is low.

As the pump energy increases, we expect the thermal distribution of the electrons to increase. Before excitation, some of the conduction electron density extends beyond the physical nanoparticle. As the temperature of the electrons becomes elevated, the electron density is expected to extend even further from the particle and is distributed

unevenly across the aggregate volume.[10,95] This increased charge delocalization results in a red shift of the LSPR.[96,97]

We can use the magnitude of the LSPR shift, as seen in our ultrafast SERS measurements in conjunction with previous electrochemical measurements of plasmon bleaching, to estimate the magnitude of charge density delocalization. Electrochemical tuning of plasmonic nanoparticles drives LSPR shifts by adding or removing charge density from a plasmonic nanoparticle by scanning across the potential in an electrochemical cell. These studies show a transient LSPR shift arising from a change in the charge density of the nanoparticles.[98–100] When charge density increases in the nanoparticles, the LSPR blue shifts and when the charge density decreases, the LSPR red shifts.[97] In the case of our measurement, we drive the LSPR shift photochemically by plasmon excitation instead of electrochemically. Thus, we can use the magnitude of the LSPR shift, measured by the peak depletion in the transient SER spectra at the saturation point in Figure 3.4b, to determine the degree of charge delocalization. While majority of SERS signal comes from a rather small percentage of molecules in the high field region,[13] our measurements probe an ensemble of hot spots of various intensity. In previous ensemble measurements, the enhancement factors for these systems are linearly related to the LSPR magnitude,[101] which would suggest that comparing the LSPR magnitude to our ensemble SERS signal is reasonable.

To estimate the degree of charge density change from the transient LSPR shift, we must make several approximations. Further details for this approximation, based on electrochemical models, are presented Appendix A. At the saturation point in Figure

3.4b, the SERS magnitude decreases by 10%, which we assume corresponds to a 10% decrease in the LSPR magnitude, based on ensemble-averaged SERS measurements.[101] From the charge density modeling for electrochemically driven LSPR shifts,[96] we estimate that the charge density change experienced in our system is approximately 0.7%, based on the LSPR magnitude change between 1035 to 1200 nm. Based on size estimates of our aggregates and the number of Au nanoparticle monomers which comprise them, we estimate that approximately 10^{11} conduction electrons are associated with a single aggregate. Thus, this charge density change results in the displacement of on the order of 10^{9} free electrons. The modeling of the electrochemical system suggests that majority of the charge density change occurs at or near the surface of the nanoparticles.[97] For optically excited nanoparticles, theoretical modeling shows hot carriers distributed across a nanoparticle with an increased concentration of hot electrons at or near the surface after plasmon excitation compared to the pre-excited system.[10] Based on these electrochemical measurements and modeling, the charge density change may be localized along the surface of the nanoparticle, potentially leading to a probability of charge-transfer with adsorbed molecules. Future work could provide additional support for transient charge delocalization resulting in an LSPR shift. Ultrafast SERS measurements in which the first solvent shell is resonantly enhanced could provide a direct measurement of charge transfer to nearby solvent molecules. Additionally, ultrafast electron microscopy or cathodoluminescence may enable direct probing of wavefunction delocalization, along with fully quantum mechanical calculations which include explicit solvent and analyte.

We hypothesize that the transient SERS depletion features observed here result from a shift in the LSPR intensity due to charge delocalization. Thus, the electronic wavefunction of the plasmonic aggregate must spread to nearby adsorbate or solvent molecules. We do not directly observe frequency shifts in the probed adsorbates with the ultrafast SERS measurements. These frequency shifts may not arise if the added charge to each adsorbed molecule is so small that there is no detectable shift. Additionally, as the majority of the SERS signal results from a small fraction of adsorbates,[102] the newly delocalized charge may not interact with the molecules giving rise to the SERS signal, perhaps interacting instead with other adsorbates or surrounding solvent molecules. Future work could provide additional support for transient charge delocalization resulting in an LSPR shift. Ultrafast SERS measurements in which the first solvent shell is resonantly enhanced could provide a direct measurement of charge transfer to nearby solvent molecules. Additionally, ultrafast electron microscopy or cathodoluminescence may enable direct probing of wavefunction delocalization, along with fully quantum mechanical calculations which include explicit solvent and analyte.

3.4 Conclusions

Using ultrafast SERS, we observed transient peak depletions following plasmon excitation of aggregated gold nanoparticles with adsorbed 4-NBT. The transient peak depletions arise from a plasmon-driven shift in the LSPR spectrum. This LSPR shift is caused by hot electrons, which are generated upon plasmon excitation. These hot electrons may cause the LSPR shift through their uneven distribution on the surface of the nanoparticles, charge-transfer between the hot electrons and adsorbed molecules, or

electron-phonon interactions, which heat the metal lattice. By determining the magnitude of the LSPR shift, we estimated a surprisingly large number of photons drive plasmon excitation, which may result in a significant magnitude of delocalized charges. From these indirect measurements, we describe how the charge delocalization driven by plasmon excitation arises from hot electron generation, which may be used to increase the efficiency of many plasmon-driven applications.

3.5 Methods

The instrumentation used for ultrafast SERS measurements is similar to that previously described.[11] Incident 220 fs at 1035 nm with a repetition rate of 24.5 MHz at 20.5 W output (Clark-MXR Impulse) was split to generate the pump and probe beams. The picosecond probe pulse was generated by sending 6 W of the incident beam into a spectral filter which contains a transmission grating to disperse the beam and a 100 mm focal length cylindrical lens to collimate the beam and send it to a slit. The spectral width of the probe is 12.6 cm^{-1}, measured from the 801 cm^{-1} peak of cyclohexane. Pump wavelengths used for excitation were 700, 750, 800, and the fundamental wavelength of 1035 nm. For wavelengths other than 1035 nm, a commercial NOPA (Clark-MXR) generated the pump beam from the Impulse output with a repetition rate of 2.04 MHz at 16 W. The bandwidth of the NOPA output at 700 nm, 750 nm and 800 nm was 16 nm, 28 nm and 50 nm, respectively. Unwanted NIR wavelengths from the NOPA output were removed by placing two 950 nm shortpass filters before the sample. The time delay between the pump and probe pulses was controlled by delay stage (Newport XMS50) in the pump path to obtain different time points during an experiment. The probe and pump

beams were focused onto the sample by a 100 mm focal length achromatic lens. After the sample, the spontaneous Raman signal was collimated by a 60 mm focal length lens with 830 and 850 nm longpass filters in place to reduce pump beam transmission. Any remaining fundamental from the Raman signal was removed by a 1064 nm Raman filter directly before the spectrograph. The Raman signal was focused onto a spectrograph (Princeton Instruments, 2300i), with a 600 gr/mm, 750 nm blaze grating by a 100 mm focal length achromatic lens. A 1024 pixel, liquid nitrogen cooled InGaAs array (Princeton Instruments, PYLON-IR 1.7) was used for detection. For measurements with NOPA excitation, all the collection optics were 2" in diameter to maximize the detected solid angle. All data collection was performed via home-made Labview program.

Samples were prepared by concentrating 3 mL of as-synthesized colloidal gold nanoparticles, following the Frens method,[84] to a 50 μL aliquot and adding 70 μL of a saturated aqueous solution of 4-nitrobenzenethiol. The nanoparticles were aggregated by adding 330 μL of an aqueous solution of potassium nitrate with concentrations ranging from 0.0318 M to 0.0454 M. Once prepared, the sample was transferred to a 2 mm quartz cuvette. Samples were stirred throughout the course of the experiment to refresh the sample in the spot size and to minimize precipitation of the aggregated particles.

3.6 Acknowledgements

This material is based on work supported by the Air Force Office of Scientific Research under AFOSR Award No. FA9550-15-1-0022. Parts of this work were carried out in the Characterization Facility at the University of Minnesota, which receives partial support from the NSF through the MRSEC program. The authors thank Prof. David Blank for access to the UV−visible spectrophotometer used for sample characterization, and Prof. Cari Dutcher and Ms. Shweta Narayan for flow volume replenishment simulations.

Chapter 4

Ultrafast Nanoscale Raman Thermometry Proves Heating Is Not a Primary Mechanism for Plasmon-Driven Photocatalysis

Reprinted with permission from manuscript by Emily L. Keller and Renee R. Frontiera *ACS Nano* **2018**, *12* (6), 5848-5855.

4.1 Synopsis

Plasmonic materials efficiently convert light to various forms of energies for many applications, including photocatalysis, photovoltaics, and photothermal therapies. In particular, plasmonic photocatalysts hold incredible promise for highly selective sunlight-driven catalysis through the generation of highly energetic holes and electrons used to drive chemical reactions. However, plasmons are also known to generate heat, and the partitioning of photoexcitation energy into hot carriers and heat on molecularly-relevant timescales is not well understood, yet plays a crucial role in designing and understanding these photocatalysts. Using an ultrafast surface-enhanced Raman thermometry technique, we probe the effective temperature, equivalent to the mode-specific increase of vibrational kinetic energy, of molecules adsorbed to gold nanoparticle aggregates in the most active hot spots on the picosecond timescale of chemical reactivity. This represents the first measurement of vibrational energy deposition for coupled molecular-plasmonic systems on the picosecond timescale of molecular motion. We find that upon plasmon excitation, the adsorbates in the hot spots undergo an initial energy transfer within several picoseconds that changes the effective temperature of the system by less than 100 K, even at peak flux values 10^8 times stronger than focused sunlight. The energy quickly dissipates from the adsorbates into the surroundings in less than 5 ps, even at the highest values of photoexcitation. This surprisingly modest energy transfer of the most active regions of the plasmonic materials on the ultrafast timescale decisively proves that most plasmonic photocatalysis is not primarily thermally driven.

4.2 Introduction

Plasmonic materials convert light into various forms of energy, which can be used for processes as varied as driving chemical reactions, heating the surrounding environment, and increasing scattering efficiency. These efficient plasmon-driven energy conversions[5,44] have led to advances in many different applications including CO_2 reduction,[103,104] water splitting,[22,105] water purification,[74] cancer therapies,[2,106] and photovoltaic devices.[1] However, a molecular-level picture of the mechanism of these processes is generally unknown, and requires a quantitative understanding of how plasmon energy can be rapidly converted into other forms. Plasmons are generated when excitation with resonant light generates a collective oscillation in the electron density of a plasmonic material. The oscillation confines the electromagnetic field into a small area, typically between two or more nanostructures, generating a hot spot.[13] Plasmons decay on very rapid timescales, leading to the generation of hot carriers and heating of the local environment in the first femtoseconds and picoseconds after photoexcitation. However, it is unclear what mechanisms govern the partitioning of energy into hot carriers, heating, or electric field enhancement and how they can be tailored to maximize the efficiency of a desired plasmon-driven process.[7]

In particular, heating may affect the efficiency of these plasmon-driven applications. Catalytic processes can exhibit significant rate and/or yield increases with increased temperature. For example, the Haber-Bosch process to synthesize ammonia from N_2 and H_2 shows yield increases of 15% when increasing the temperature from 350 to 450 degrees Celsius.[107] Given that the temperature experienced by molecules in a

plasmonic hot spot has not been previously determined, it is unknown to what extent localized temperature increases contribute to recent reports of plasmon-powered catalysis. Previous studies of various plasmon-driven reactions demonstrated the differences between the product yield of the light-driven process as compared to a thermal-driven process.[71,108,109] However, these comparisons did not allow for the control or measurement of localized heating near the reaction sites, which can differ from the heating of the overall sample.[110] Given that the temperature of electron gases in metals can reach 100s to 1000s of Kelvin, it is possible that heating could play a significant role in increasing the rate of catalysis in a plasmonic hot spot.[104] If plasmonic photocatalysis is primarily a result of increased localized temperatures, experimental optimization of reaction selectivity would be much more challenging than if alternative mechanisms, such as hot carrier transfer, are predominantly responsible for the chemical reactivity. Clearly, there are a wide range of possible temperatures in plasmonic hot spots, which may affect how each of these plasmon-driven processes work.

To determine the temperature increase following plasmonic excitation, previous studies have used techniques such as thermocouples,[74,111,112] IR cameras,[103,113] and various optical thermal microscopy methods.[114] These methods provide valuable information about how heat dissipates across these structures and how that affects the temperature of the surroundings. However, these techniques are ensemble measurements and do not measure the localized heating in hot spots, which are the sites responsible for plasmonic catalysis.[11] Techniques with higher spatial resolution, as well as selectivity for

the hot spots, are needed to monitor the temperature where the plasmonic photochemistry is actually occurring.[115]

Raman spectroscopy can be used to measure molecular temperatures by comparing the mode-specific relative intensities of Stokes and anti-Stokes scattering.[116,117] Surface-enhanced Raman spectroscopy (SERS) is a plasmon-enhanced Raman technique with high selectivity for the most active regions on a plasmonic surface. Boerigter *et al*. used steady-state SERS to examine the differences in temperature between metal nanoparticles and adsorbed molecules and how the effective coupling between the plasmon and adsorbates results in efficient energy transfer to drive chemical transformations.[8] To more closely examine molecular heating in plasmonic hot spots, Pozzi *et al*. measured the temperature of single molecules in plasmonically active hot spots and found that the variance between the wavelength dependent enhancement in the hot spots greatly affected the measurements.[118] These studies demonstrate the power of SERS to examine heating within plasmonic hotspots, but they lack the temporal resolution necessary to probe dynamics on the timescales most relevant to plasmonic photocatalysis.

In considering how heating might play a role in driving plasmonic photocatalysis, the relevant timescale to monitor is the ultrafast timescale of bond-breaking and –making processes.[58,119] By adding energy to vibrational modes, it is possible to selectively break bonds,[120] but molecules are extremely effective at rapidly dissipating energy through processes such as intramolecular vibrational redistribution (IVR) or by transfer of energy through the solvent on the picosecond timescale. Additionally, the partitioning of energy

into heat and hot carriers in plasmonic systems occurs on a very rapid timescale.[10] Upon photoexcitation, plasmons undergo plasmon damping and electron thermalization within 1-100 fs, generating hot carriers. The hot carriers scatter off the phonons in the metal lattice between 1-10 ps, which generates a hot metal lattice that eventually cools after > 100 ps.[7–9] To definitively determine how significant heating is to driving photochemical reactions on plasmonic surfaces, measurements on the ultrafast timescale are crucially needed.

4.3 Results and Discussion

Here we use ultrafast Raman thermometry to quantify the degree of energy deposition from photoexcited plasmons into molecular adsorbates. Obviously, on ultrafast timescales the system is not at equilibrium and temperature is not a relevant term, but we apply a similar analysis to obtain what we define as an effective temperature, which indicates the amount of energy deposited into each vibrational mode, equivalent to the time-dependent vibrational kinetic energy. By measuring Stokes and anti-Stokes Raman spectra as a function of time, we calculate the mode-specific change in vibrational energy using a Boltzmann distribution analysis, as described by Equation 4.1:[117,121]

$$\text{Effective Temperature (K)} = \frac{-\text{Energy of Vibration (J)}}{k_b * \ln\left(\frac{\text{Intensity}_{\text{anti-Stokes}}}{C * \text{Intensity}_{\text{Stokes}}}\right)} \quad (4.1)$$

where C equals $((\omega_L+\omega_{vib})/(\omega_L-\omega_{vib}))^4$, which describes the wavelength dependence of Raman scattering based on the excitation frequency (ω_L) and the corresponding

vibrational mode frequency (ω_{vib}). From this analysis, we are unable to obtain absolute temperatures for the non-equilibrium system, however we can compare the relative changes in effective temperature or energy deposition over the course of the measurement as well as between different modes. Using the Boltzmann distribution to estimate temperatures from Raman spectra is widely applicable across the field of Raman spectroscopy.[121–123] Equation 4.1 does not account for any possible chemical enhancement differences between the anti-Stokes and Stokes Raman features. We assume there is no contribution from new electronic states at 1035 nm due to the separation between the absorption band of the analytes and the excitation wavelength for these experiments. Based on shifts in the electronic states observed in other studies,[124] it is unlikely that a new electronic state would shift so far from the original electronic state.

To probe the effective temperature in the most active regions of plasmonic photocatalysts, we use ultrafast surface-enhanced Raman spectroscopy (SERS), which is selectively sensitive to the hottest hot spots.[11,12] The scheme in Figure 4.1a describes the experimental set-up. We photoexcite the plasmonic sample with a femtosecond pump pulse, centered at 1035 nm or doubled though second harmonic generation to 518 nm. We use a picosecond Raman probe pulse at various time delays to give a SER spectrum of the molecules adsorbed in the hot spots on the aggregated nanoparticles. We collect anti-Stokes and Stokes signal, which leads to an effective temperature measured at each time point for each vibrational mode. This approach provides the inherent surface selectivity and appropriate temporal response to definitively quantitate thermal increases of molecular adsorbates on plasmonic surfaces.

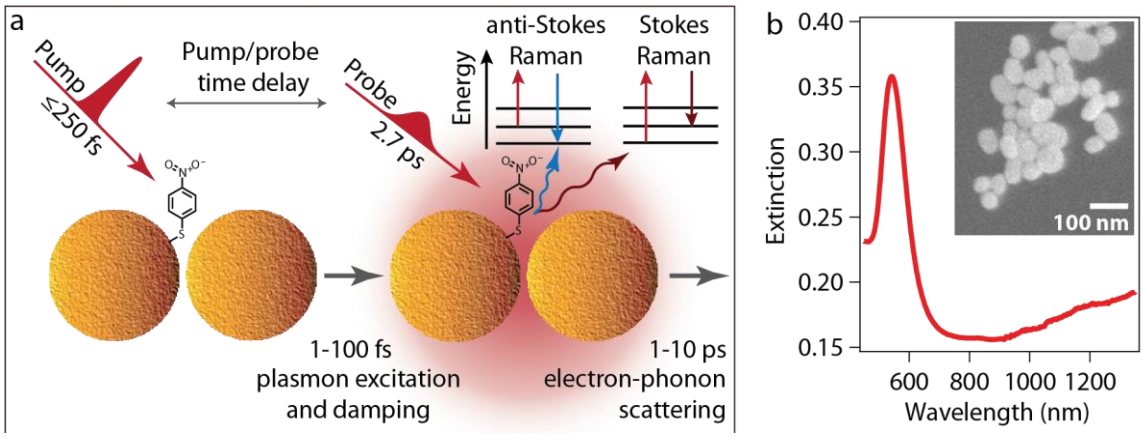

Figure 4.1 (a) Scheme depicting ultrafast Raman thermometry of plasmonic photocatalysts. Using a femtosecond pump pulse, we excite the plasmon and then obtain Stokes and anti-Stokes surface-enhanced Raman spectra using a picosecond probe pulse at various time points during this process.[7–9] (b) Extinction spectrum of the aggregated colloidal gold nanoparticle sample with adsorbed 4-nitrobenzenethiol. The inset is a scanning electron micrograph of the gold nanoparticles for which the monomers have an average diameter of 80 ± 30 nm.

In Figure 4.1b, we show an extinction spectrum of colloidal gold nanoparticles aggregated by electrostatic interactions driven by the addition of a 0.04 M aqueous solution of potassium nitrate (Figure B1). The aggregated samples are quite heterogeneous, as shown by the broad plasmon resonance response in the NIR region of the spectrum, with many different types of plasmonic interactions providing surfaces with a range of enhanced electric field magnitudes.[125] The analyte for our ultrafast SERS measurements is 4-nitrobenzenethiol (4-NBT) and *trans*-1,2-bis(4-pyridyl)ethylene, which adsorbs to the surface of the nanoparticles. 4-NBT can undergo plasmon-driven dimerization to dimercaptoazobenzene (DMAB),[85,86] which is present to a minor degree in our samples. However, our samples do not undergo additional reactions during our spectroscopic measurements and the populations of 4-NBT and DMAB remain steady.[11,12] The inset of Figure 4.1b is a scanning electron micrograph of the colloidal

gold nanoparticles with an average monomer diameter of 80 ± 30 nm, as measured by ImageJ software.

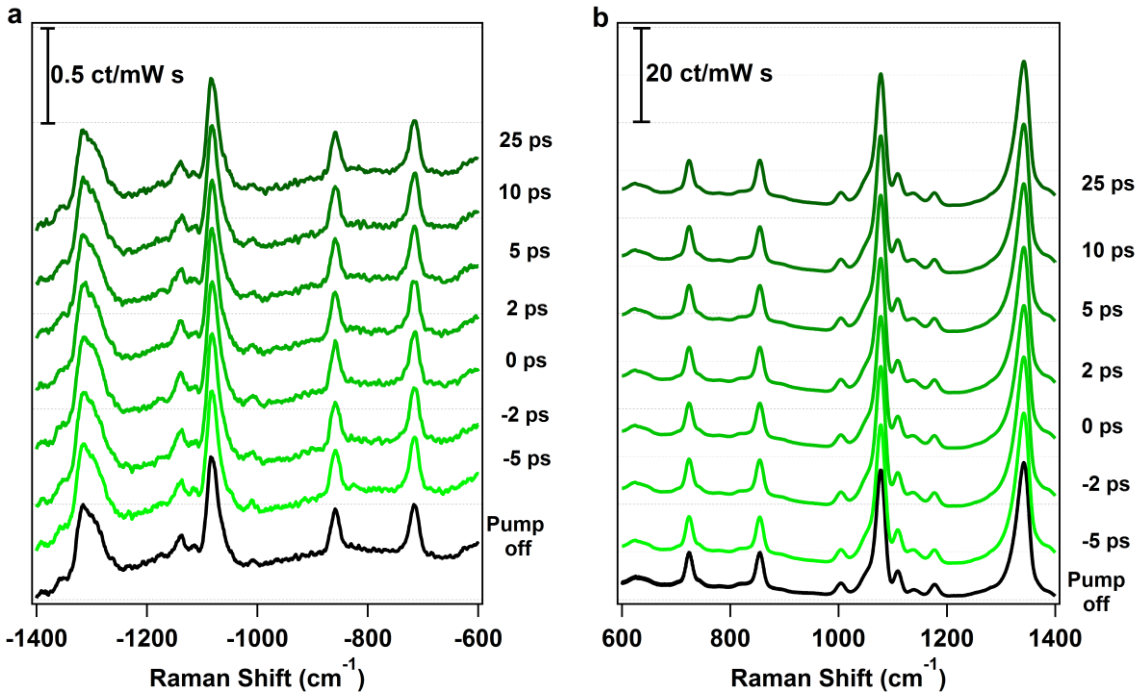

Figure 4.2 Ultrafast surface-enhanced (a) anti-Stokes and (b) Stokes Raman spectra of 4-nitrobenzenethiol adsorbed to colloidal gold nanoparticles with 50 W/cm^2 photoexcitation flux and 250 W/cm^2 probe flux. Spectra are offset for clarity.

Figure 4.2 shows ultrafast SER spectra obtained at 1035 nm with 50 W/cm^2 photoexcitation flux, which corresponds to a peak power of 8 MW/cm^2 (Table B1 & B2). For reference, experiments using focused sunlight typically have photoexcitation fluxes of 0.1 W/cm^2.[3] The pump-on spectra (denoted in green) are offset from the pump-off spectrum (black) after scaling each spectrum. Figure 4.2a shows the anti-Stokes spectra and Figure 4.2b shows the Stokes spectra, with the Stokes spectra approximately 40 times larger than the anti-Stokes spectra as indicated by the scale bars in the upper left corners. The changes between the transient pump-on spectra are relatively minor and are not

obvious upon initial inspection of the data. These small changes suggest that the effective temperature change between each time point is small relative to the vibrational frequency.

To quantify the effective temperature at various time points, we fit the 1079 cm^{-1} peak in Figure 4.2 to a Gaussian function to extract the amplitude. We use the peak amplitudes from the anti-Stokes and Stokes spectra in Equation 4.1 to obtain effective temperatures at every time point. To account for wavelength dependent enhancement, which arises in SERS from the plasmon resonance of the sample,[101] we normalize the peak amplitudes at each time point before calculating the effective temperature. Further details for these calculations can be found in the Methods.

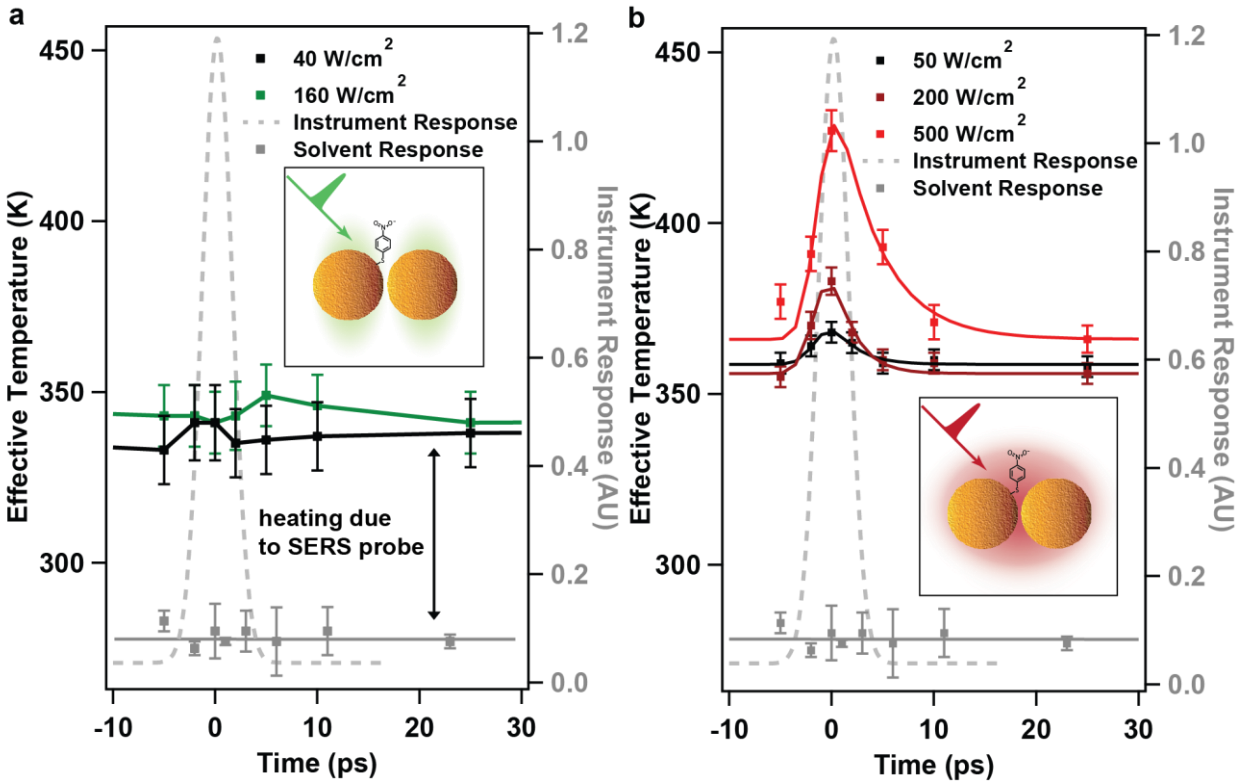

Figure 4.3 Energy distribution at varying pump excitation fluxes (a) with cross-polarized 518 nm excitation for 1079 cm^{-1} mode in 4-nitrobenzenethiol adsorbed to gold nanoparticle aggregates. The adsorbates have a baseline effective temperature due to the interaction with the picosecond probe pulse used to obtain surface-enhanced Raman spectra. Energy distribution at varying pump excitation fluxes (b) with 1035 nm excitation for 1079 cm^{-1} mode in 4-nitrobenzenethiol adsorbed to gold nanoparticle aggregates. The magnitude of energy deposited into the 1079 cm^{-1} mode is relatively modest considering the strong pump fluxes used. Inset is representative of an ensemble.

In Figure 4.3, we plot the effective temperatures from -5 to 25 ps for two different pump wavelengths at 518 nm and 1035 nm excitation, along with the instrument response with respect to time as measured by the optical Kerr effect in toluene. Figure 4.3 also depicts the instrument response with respect to temperature, as measured by a sample containing aggregated gold nanoparticles in isopropyl alcohol with no adsorbate while monitoring the 818 cm^{-1} peak in isopropyl alcohol. The solvent response shows minimal sample heating arising from the high power laser pulses and lacks any time dependent

features, illustrating the importance of surface-specific probing for plasmonic thermometry measurements.

In Figure 4.3a, we display ultrafast Raman thermometry values for a control experiment, in which photoexcitation does not lead to energy transfer to molecular adsorbates. This allows us to quantitatively determine the temperature change caused by the SERS probing process. In this experiment, the pump excitation at 518 nm is orthogonally polarized relative to the 1035 nm probe. Thus, these two beams can excite and probe different regions on the plasmonic nanoaggregate surface, depending on how efficiently they couple to longitudinal or transverse plasmon modes. In these cross polarized measurements, the probed adsorbates do not undergo a transient effective temperature change that is dependent upon pump excitation. If we simplify the aggregated sample to a dimer model, as shown in the inset of Figure 4.3a, the probe beam interacts with adsorbates located between the two particles, which we refer to as the longitudinal plasmon mode. The cross polarized 518 nm pump excitation excites the transverse plasmon mode, which interacts with a different subset of adsorbates on the nanoparticle surface. When this mode is excited, the energy is not as strongly localized to the probed hot spot spatial region (inset of Figure 4.3a), and thus we see essentially no photo-induced changes in molecular effective temperature attributed to the pump excitation. As can be seen in Figure 4.3a, the adsorbates undergo 70 K increase due to the SERS probing process compared to the solvent response for this instrument. Figures 4.3a and b were obtained with different samples showing slightly different baseline values (345 K and 360 K, respectively). All measured samples showed baseline values between

340 K and 370 K, with small variations likely resulting from differences in the hot spot density within the sample.

In Figure 4.3b, the photoexcitation is on resonance with the longitudinal mode, and photoexcitation of this mode results in nano-focusing of the light between the nanoparticles, in the same area as the probed adsorbates, as depicted schematically in the inset of Figure 4.3b. Thus we see a transient increase in effective temperature upon plasmon excitation at 1035 nm that scales linearly with pump flux. The effective temperature increases very rapidly after photoexcitation, and likely results from energy transfer during the electron thermalization time of the plasmonic nanoparticles. At the highest flux, the change in effective temperature as a response to photoexcitation remains below 100 K. While these measurements are ensemble measurements of many nanoparticle aggregate hot spots, the SERS signal we measure comes from a very small percentage of the most active hot spots.[102] Thus, the hot spots, which yield the highest SERS signal, correspondingly have the greatest temperature change, giving an upper limit for temperature increases in the substrates of less than 100 K.

From the power dependence in Figure 4.3b, we estimated the thermal contribution for several examples of plasmonic photocatalysis reported in the literature (Table B3). To make these estimates, we compare the peak power of our pulsed laser to the continuous wave laser power of the literature examples. We also assume that the plasmonic heating is linear across the range of photoexcitation powers in our experiments and the examples from the literature based upon the linear power dependent response we observed (Figure B2). Due to the number of assumptions made in these extrapolations, we report only an

order of magnitude for the scattering-induced plasmonic thermal contribution. Additional details about these estimates can be found in Appendix B. For ethylene epoxidation and acetylene hydrogenation,[4,109] the scattering-induced plasmonic thermal contribution is ~1 x 10^{-7} K and ~1 x 10^{-5} K, respectively. For H_2O splitting,[105] the thermal contribution is slightly higher at 0.01 K. Clearly, the thermal contribution for these plasmon-driven reactions is not significant. These estimates agree with previous literature which suggested but did not prove that heating contributions in these systems only become significant with sufficiently high peak powers.[110] Thus, we conclude the existing reports of plasmonic photocatalysis are not significantly affected by temperature-dependent rate or yield increases for photoconversion. These systems must rely upon hot carrier transfer to the adsorbates to drive the reaction, and thus have the potential for much higher chemical selectivity than heating alone, as has been seen in plasmon-driven acetylene hydrogenation.[4]

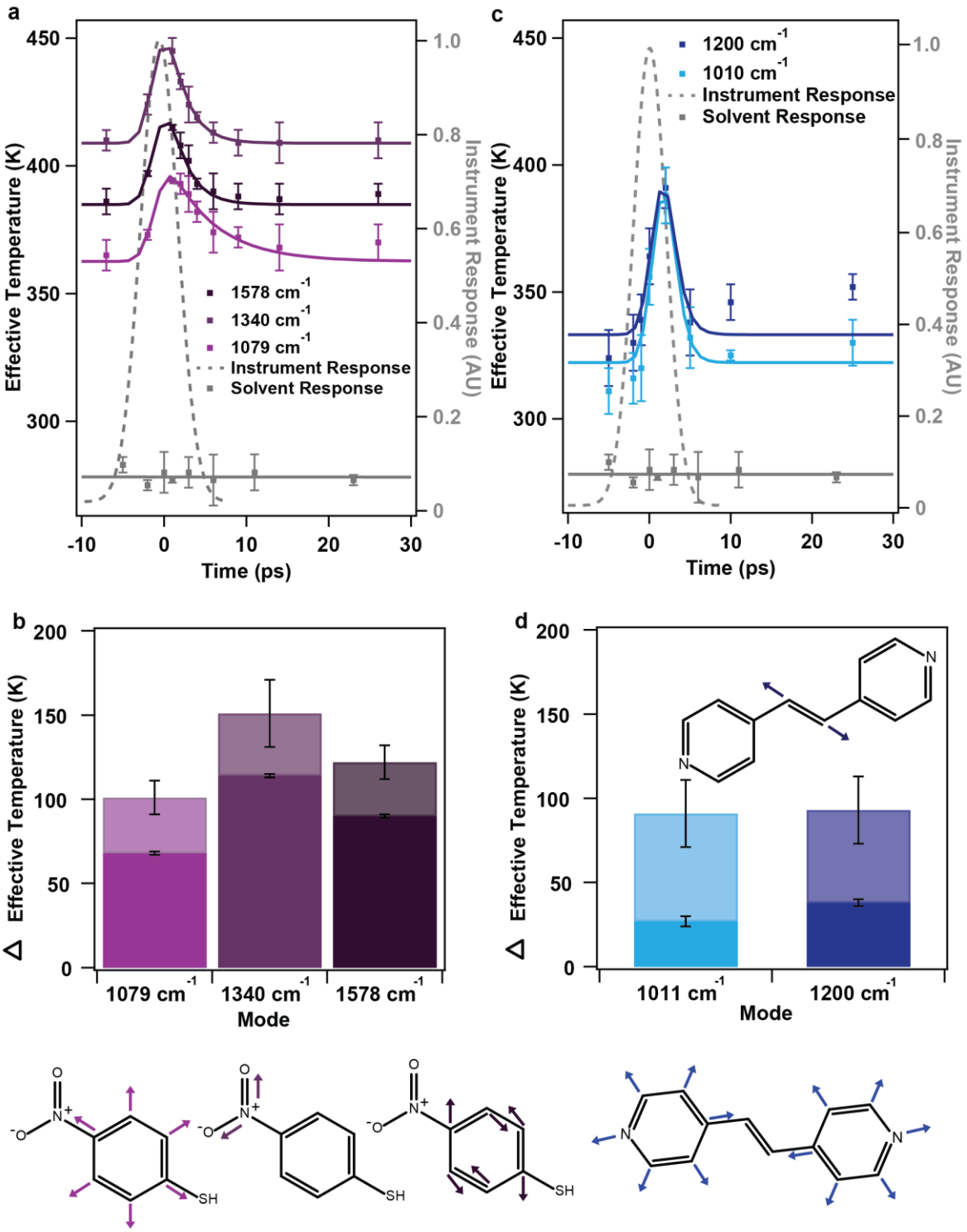

Figure 4.4 Energy distribution of various modes (a) of 4-nitrobenzenethiol adsorbed to gold nanoparticle aggregates with 1035 nm excitation at 200 W/cm^2. (b) Comparison of

effective baseline temperature (dark shading) and transient temperature change (lighter shading) relative to room temperature for three modes of 4-nitrobenzenthiol. The degree of heating depends on the coupling of each mode with the plasmon resonance. (c) Energy distribution of various modes of *trans*-1,2-bis(4-pyridyl)ethylene adsorbed to gold nanoparticle aggregates with 1035 nm excitation at 200 W/cm^2. (d) Comparison of effective baseline temperature (dark shading) and transient temperature change (lighter shading) relative to room temperature for two modes of *trans*-1,2-bis(4-pyridyl)ethylene. Similar to 4-nitrobenzenethiol, a modest deposition of energy into adsorbed *trans*-1,2-bis(4-pyridyl)ethylene occurs upon photoexcitation.

While the role of scattering-induced heating in plasmonic photocatalysis is minimal, we are also interested in how energy moves through the adsorbates and whether energy is preferentially deposited in certain modes and how this may impact plasmonic photocatalysis. Figure 4.4a depicts the heating response for three different modes in 4-NBT excited with 200 W/cm^2 pump flux at 1035 nm. The three modes are 1079 cm^{-1}, 1340 cm^{-1}, and 1578 cm^{-1}, which correspond to the ring breathing, NO_2 symmetric stretch, and carbon double bond stretch, respectively.[12] The baseline temperature of each mode varies due to different coupling with the plasmon. Modes that are highly coupled to the plasmon resonance receive greater energy deposition upon excitation. In Figure 4.4b, we compare the baseline effective temperature and the corresponding transient temperature change of each mode relative to room temperature (294 K). The darker bars represent the baseline effective temperature for each mode that arises due to the SERS probing process and the lighter bars on top represent the transient temperature change that occurs upon photoexcitation. The 1340 cm^{-1} mode, which corresponds to the symmetric NO_2 stretch, couples strongly with the plasmon and receives the most energy as seen by the baseline temperature. The 1079 cm^{-1} and 1578 cm^{-1} modes, which correspond to vibrations of the bonds associated with the benzene ring of 4-NBT, have a

similar thermal contribution to each other (Figure 4.4b). In our measurement, each mode of the adsorbate appears to receive energy on the same timescale, although, they are heated to different degrees.

A key advantage of the ultrafast approach to monitoring energy flow is the ability to extract time constants for energy dissipation. In these systems, the energy transferred into vibrational modes dissipates extremely quickly. The time constants for the fits in Figure 4.3b range from 2-5 ps where energy is transferred very quickly to and from the adsorbates. In a flash heating experiment of 4-NBT on a flash-heated gold surface, they observed a similar time constant of ~3.5 ps for the initial energy transfer to the adsorbates. At later time points, their system reaches a plateau that lasts for >200 ps and does not return to the starting value due to disorder in the self-assembled monolayer of their adsorbate on the heated gold surface.[126] However, in our measurements, the energy dissipates very rapidly, and at all powers has returned to baseline by 5 ps. In solution phase studies of a similar analyte, nitrobenzene, intramolecular vibrational relaxation (IVR) occurred within 2 ps after excitation of a particular mode.[127] If the adsorbates in our system return to baseline after 2-5 ps, then if IVR does occur in this system, then it may occur on faster timescales when the analyte is adsorbed to a plasmonic substrate than in solution. With the time resolution of our instrument, we are unable to resolve any IVR that may occur upon initial excitation of the system.

In addition to following the energy partitioning into various modes within a molecule, we can also examine how plasmon-induced heating may change with different

analytes. In Figure 4.4c, we measured the plasmonic heating for *trans*-1,2-bis(4-pyridyl)ethylene adsorbed to the surface of the gold nanoparticle aggregates using our ultrafast Raman thermometry technique (Figure B3). As seen previously, the SERS probing process results in an elevated baseline effective temperature from the solvent response due to excitation of the plasmon that occurs from the picosecond probe pulse (Figure 4.4d). Upon 1035 nm pump excitation at 200 W/cm^2, the adsorbates undergo a similar transient effective temperature increase as observed with 4-NBT. The effective temperature of each mode increases upon photoexcitation of the plasmon and once the pump pulse no longer interacts with the sample, the system returns to the baseline effective temperature within 5 ps. The variation between the baseline effective temperatures and the transient temperature change upon photoexcitation between the two molecules may arise from the different coupling of each molecule with the plasmon.

4.4 Conclusions

Here we used ultrafast SERS to measure the time-dependent effective temperature, equivalent to the vibrational kinetic energy, increase of adsorbates in the hot spots upon excitation of the longitudinal and the transverse plasmon modes. Ultrafast nanoscale Raman thermometry is a technique that allows for the measurement of localized heating directly in the most chemically reactive hot spots, acting as a nanoscale probe of vibrational energy deposition on the ultrafast timescale of chemical reactions. We find that energy deposited into molecular adsorbates very rapidly depletes, and the temperature increase is on the order of tens of Kelvin, even for extremely high photoexcitation values. Our quantification of localized heating of adsorbates in the hottest

and most active hot spots confirms that plasmon-driven chemistry is not thermally driven. Thus, hot carrier charge transfer to adsorbed reactants must play a key role in plasmon-driven chemical reactions, which is promising for applications in highly selective chemical catalysis.

4.5 Methods

Sample Preparation. Gold nanoparticles were synthesized following the Frens method.[84] The detailed synthesis is described in Appendix B. Samples for ultrafast nanoscale Raman thermometry measurements were prepared by centrifuging 3 mL as-synthesized gold nanoparticles until a pellet is formed and removing 2.95 mL of the supernatant. The gold nanoparticles were then aggregated through electrostatics by either adding 330 μL of 0.044 M aqueous potassium nitrate and 70 μL of saturated aqueous 4-nitrobenzenethiol or 350 μL of 0.032 M aqueous potassium nitrate and 50 μL of 0.18 mM *trans*-1,2-bis(4-pyridyl)ethylene dissolved in ethanol. Additional details can be found in Appendix B.

Ultrafast SERS Instrumentation. A detailed description of the instrument has been published previously.[12] In brief, <250 fs laser pulses, from a fiber amplifier (Clark MXR, Impulse) centered at 1035 nm, were split with a 50:50 beam splitter to make pump and probe pulses. The picosecond probe beam was generated by sending 6 W of the fundamental through a spectral filter, where the beam was sent through a transmission grating and focused onto a slit. The pump beam for the cross-polarized 518 nm measurements was generated by focusing 3 W of the fundamental onto a 3 mm BBO

crystal. For the 1035 nm pump measurements, a portion of the fundamental was used without further modification. The pump beam was sent onto a motorized stage to vary the time delay between the pulses. After the sample, the spontaneous Raman signal was focused into a spectrograph (Princeton Instruments, 2300i) equipped with either a 600 gr/mm grating blazed at 750 nm or a 300 gr/mm grating blazed at 1 μm. The signal was then focused onto a liquid N_2 cooled 1024 pixel InGaAs array (Princeton Instruments, Pylon-IR 1.7). A 1064 nm Raman edge filter before the spectrograph was used to collect Stokes spectra, while a 1000 nm short pass filter was used for collecting the anti-Stokes spectra. Additional details about the set-up and data collection can be found in Appendix B.

Calculating Effective Temperatures. We have rewritten the Boltzmann distribution in a more useful form for our measurements as follows:

$$\text{Effective Temperature (K)} = \frac{-\text{Energy of Vibration (J)}}{k_b * \ln\left(\frac{\text{Intensity}_{\text{anti-Stokes}}}{C * \text{Intensity}_{\text{Stokes}}}\right)}$$

where C equals $((\omega_L+\omega_{vib})/(\omega_L-\omega_{vib}))^4$, which describes the wavelength dependence of Raman scattering based on the excitation frequency (ω_L) and the corresponding vibrational mode frequency (ω_{vib}).

Obviously, the Boltzmann distribution applies only to systems at equilibrium, and does not apply to picosecond timescale dynamics. Thus, we use the term "effective temperature" to describe the energy distribution in the system obtained by this analysis. This value quantifies the mode-specific energy deposition in the system, equivalent to the

increase in vibrational kinetic energy. Each peak is fit to a Gaussian function to extract the amplitude. We use the peak amplitudes from the anti-Stokes and Stokes spectra in the above equation to obtain effective temperatures for each mode at every time point. The analysis in Figure 4.3 uses amplitudes from the intense 1079 cm^{-1} mode of 4-NBT.

To account for wavelength dependent enhancement, which arises in SERS from the localized surface plasmon resonance (LSPR) of the sample,[128] we take the Raman amplitudes and divide by the extinction of the LSPR at either 931 nm or 1165 nm, which corresponds to the anti-Stokes and Stokes scattering for the 1079 cm^{-1} mode, respectively. Additionally, we also take into account the wavelength dependent efficiencies of the detector by scaling each amplitude with the corresponding detector efficiency at each wavelength as described in Appendix B. An example of this calculation is shown below:

$$\text{Intensity}_{\text{Stokes}} = \frac{\text{Peak Amplitude for 1079 cm}^{-1}{}_{\text{Stokes}}}{\text{Extinction}_{1165\text{ nm}}} \times \text{detector efficiency}_{1165\text{ nm}}$$

$$\text{Intensity}_{\text{anti-Stokes}} = \frac{\text{Peak Amplitude for 1079 cm}^{-1}{}_{\text{anti-Stokes}}}{\text{Extinction}_{931\text{ nm}}} \times \text{detector efficiency}_{931\text{ nm}}$$

These intensities are then used in Equation 4.1 to determine an effective temperature at each time point. For analysis of additional modes, as applied in Figure 4.4, these equations are modified to reflect the corresponding wavelengths and energy for each mode.

4.6 Acknowledgements

This material is based on work supported by the Air Force Office of Scientific Research under AFOSR Award No. FA9550-15-1-0022 and by the University of Minnesota Doctoral Dissertation Fellowship. Parts of this work were carried out in the Characterization Facility at the University of Minnesota, which receives partial support from the NSF through the MRSEC program. The authors thank Prof. David Blank for access to the UV−visible spectrophotometer used for sample characterization.

Chapter 5

Effect of Silica Supports on Plasmonic Heating of Molecular Adsorbates as Measured by Ultrafast Surface-Enhanced Raman Thermometry

Reprinted with permission from manuscript by Emily L. Keller, Hyunho Kang, Christy L. Haynes and Renee R. Frontiera. To be published.

5.1 Synopsis

Plasmonic materials show great potential for selective photocatalysis under relatively mild reaction conditions. Many studies have focused on tailoring the plasmonic properties of these catalysts to improve their efficacy and overall yield. However, the catalytic activity of these plasmonic catalysts can also depend upon the catalytic support material that stabilizes the catalysts, where the composition of the catalytic support may change the overall photocatalytic efficiency. It is unknown how changes in the support material may change the plasmon-driven photocatalysis, which may be initiated by plasmon-derived hot carriers, localized heating, or enhanced electromagnetic fields. Herein, we probe the effects of catalytic supports on heating in plasmon-driven catalysis by examining various gold nanoparticle-oxide systems. We use ultrafast surface-enhanced Raman thermometry to measure the effective temperature, equivalent to the vibrational kinetic energy, of reporter molecules located between plasmonic gold nanostructures and various local environments ranging from ligands to mesoporous silica shells to silica shells. Upon photoexcitation, the transient effective temperature, equivalent to the energy deposited into a vibrational mode, of adsorbed molecules on the silica coated samples increases and the energy quickly dissipates within 3 ps. However, the baseline effective temperature that arises due to the SERS probing process depends upon the encapsulant, where the energy deposition differs by 200 to 300 K between the ligand coated (citrate or CTAB) and the silica coated (mesoporous or non-porous) samples, Adsorbates surrounded by a silica shell experience higher effective temperatures than adsorbates surrounded by ligands or solvent, likely due to the differing heat

capacities of these media. Taken together this work shows that a silica support impacts the localized heating of molecular adsorbates on the gold surface and may play a role in enhanced plasmonic photocatalysis due to increased thermal contributions.

5.2 Introduction

Plasmonic materials show great promise for highly selective photocatalysis by favoring the chemical pathway that produces the desired product and minimizing side reactions.[4,5,103,109] Plasmonic catalysts can drive a variety of reactions, including water splitting,[105] ethylene epoxidation,[109] selective hydrogenation,[4] and many others.[5] However, these systems are not as efficient as they could be, which may be due to, in part, a lack of understanding of the mechanisms for plasmonic photocatalysis.[22] Possible mechanisms rely on different energy partitioning pathways that occur upon plasmon excitation, including hot carrier generation, enhanced electromagnetic fields, and localized heating. The preference for each pathway may be highly dependent on the plasmonic photocatalyst or the desired chemical reaction. Not only is it important to understand the dissipation of energy into different pathways upon photoexcitation of a plasmonic material, but it is also vital to understand how the surrounding environment may influence the catalytic process.

While most reports of plasmonic photocatalysis focus on optimization of the plasmonic catalysts, the materials used to support them also affect their catalytic performance.[72] Catalytic supports are a good way to disperse the catalytic nanomaterials and provide stability while minimizing the obstruction of active sites.[129] Common support

materials include metal oxides, carbonaceous materials, and polymers.[129] Even in non-plasmonic catalysis, the support material can affect the activity of the catalysts due to interactions between the metal and support.[130–132] Common supports for plasmonic photocatalysts are typically semiconductors, such as TiO_2, SiO_2, and Al_2O_3.[131–133] It is likely that the catalyst composition will affect the catalytic process as in traditional catalysis, although there are fewer existing studies on the effect of the support for the developing field of plasmonic photocatalysis. In one of the earliest examples of plasmonic photocatalysis, the yield of plasmon-driven H_2 dissociation was shown to be dependent on the catalytic support of the plasmonic material.[72] In particular, the authors observed 2 orders of magnitude difference in catalytic activity between TiO_2 and SiO_2 catalytic supports, which they attributed to the formation of a Schottky barrier between the gold nanoparticles (AuNPs) and the TiO_2 support. The Schottky barrier allowed the highly energetic plasmon-derived electrons to transfer to the support, which prevented them from driving the H_2 dissociation on the gold surface. However, more detailed studies directly proving the effects of support materials on plasmonic photocatalysis are needed to definitively identify mechanistic impacts, particularly in terms of the effects on hot carrier transfer and localized heating.

The contribution of thermal energy towards lowering the energetics of a reaction is an important component of catalysis.[134,135] For plasmon-driven H_2 dissociation, they estimated the contribution of plasmonic localized heating for TiO_2 and SiO_2 supports and attributed the differences in heating to the thermal conductivity of the support.[72] This result highlights the importance in considering the thermal properties of the materials

near the plasmonic catalysts, including the thermal conductivity and heat capacity of the material. The physical and chemical properties of the surrounding material may affect the energy dissipation around the catalysts, which may, in turn, affect their catalytic activity. Clearly, catalytic supports can play an important role in plasmonic photocatalysis by affecting the local environment near the catalytically active surface.

In particular, the effect of catalytic supports on energy partitioning of a plasmonic catalyst is a key component to elucidating the mechanisms driving plasmonic photocatalysis. The energy partitioning upon plasmon decay occurs on the ultrafast time scales of femtoseconds to picoseconds.[7,9] Upon photoexcitation with resonant light, the charge density of a plasmonic material begins to coherently oscillate. Within 1 to 100 fs, plasmon damping and electron thermalization occurs *via* inelastic electron-electron scattering, generating a Fermi-Dirac population of highly energetic or hot carriers.[10,44] Within 1 – 10 ps, these hot carriers can interact with their surroundings, including transferring to adsorbed molecules, nearby solvent molecules, and scattering off ,phonons in the metal lattice. Upon electron-phonon scattering, the metal lattice becomes hot and eventually reaches equilibrium with the local environment in 100s of picoseconds.[7,52] Catalytic supports may alter the plasmon decay pathway, leading to mechanistic changes for plasmon-mediated reactions. To understand how catalytic supports affect plasmonic catalytic processes, we need to examine the evolution of energy partitioning within the system on the picosecond time scale of chemical reactivity.

One technique for studying complex plasmonic photocatalytic systems on the time scales of chemical reactivity is ultrafast surface-enhanced Raman spectroscopy

(SERS), which provides insights into plasmon-molecule interactions leading to chemical catalysis.[80] SERS is a plasmon-enhanced vibrational technique, which can be used to monitor plasmon processes from the point of view of adsorbed molecules on the surface. When coupled with a femtosecond plasmon excitation pulse, ultrafast SERS can provide structural snapshots of the evolving plasmonic-molecular system. Not only can ultrafast SERS provide structural information about adsorbed molecules on the plasmonic surface, this technique can also act as an ultrafast nanoscale thermometry technique. The temperature of specific modes can be determined by measuring the intensity ratio of the anti-Stokes and Stokes Raman peaks of a mode and applying a Boltzmann distribution analysis.[117,123,124] Essentially, the adsorbed molecule acts as a nanoscale thermometer reporting on the degree of heating, equivalent to the energy deposition into vibrational modes of the adsorbate, in a highly localized environment.

Using ultrafast SERS, we can monitor the heating response of an analyte on the picosecond time scale of plasmon dynamics and chemical reactions.. By probing the system on the picosecond time scale, temperature becomes an inaccurate way to describe the system, which is no longer at equilibrium. Instead, ultrafast SERS measures an effective temperature, which is equivalent to the vibrational kinetic energy deposited into a specific vibrational mode.[136] Using ultrafast SERS, we can examine how changes to the catalytic support may affect the local heating of adsorbates on the time scale of chemical reactivity. These differences may help to explain why some supports increase the catalytic activity or selectivity of a plasmonic catalyst.

5.3 Results and Discussion

To study the effects of silica supports on plasmon-driven heating, we examined four different samples as described in Figure 5.1a-d via transmission electron micrographs (TEM) and schematic depictions. The four samples, all with *trans*-1,2,-bis(4-pyridyl)ethylene (BPE) reporter molecules directly adsorbed to a gold nanoparticle surface, ranged in coatings from ligands (CTAB or citrate), a mesoporous silica shell, or a non-porous silica shell. Mesoporous silica supports are of particular interest for selective photocatalysis due to their porous nature. By controlling pore size, mesoporous silica supports can increase catalyst selectivity by limiting the type of molecules which can reach the catalyst surface.[137] The pore size can be tuned for the reactant of interest and prevent large molecules from interfering with the desired catalytic process. For comparison, we also examined a non-porous silica support and ligand-encapsulated particles without an oxide support.

The two silica coated samples consist of silica encapsulated gold nanoparticle (AuNP) dimers with BPE adsorbed to the gold surface prior to the synthesis of the silica shell (Figure 5.1a, green), and mesoporous silica coated gold nanorods (AuNRs) synthesized with a hydrophobic silane precursor (Figure 5.1b, chlorotrimethylsilane (TMS), blue). The silica encapsulated AuNP dimers were obtained from Becton Dickinson (SERS440 Nanotags) and used without further purification. The gold cores are approximately 60 nm in diameter with silica shell thickness of approximately 50 nm. The mesoporous silica AuNRs were synthesized following a previously published procedure.[138] Further synthetic details can be found in the Methods and Appendix C. This

synthesis produces a mesoporous silica shell around the AuNR with pore diameters between 4 to 10 nm.[139] The thickness of the silica shells at the SERS-active tips of the AuNRs is 8 ± 2 nm, as measured by TEM. The pores allow for the migration of analytes from the bulk solution to the gold surface. The two ligand coated nanomaterials consist of cetyltrimethylammonium bromide (CTAB)-capped AuNRs (Figure 5.1c, red), the same as those used in the synthesis of the mesoporous silica AuNRs, and citrate-capped AuNP aggregates. The AuNRs were obtained from Nanohybrids and used without further purification. The citrate-capped AuNPs (Figure 5.1d, yellow) were synthesized following the Frens method,[84] and were aggregated by the addition of 0.025 M aqueous potassium nitrate and 20 μM BPE dissolved in ethanol.

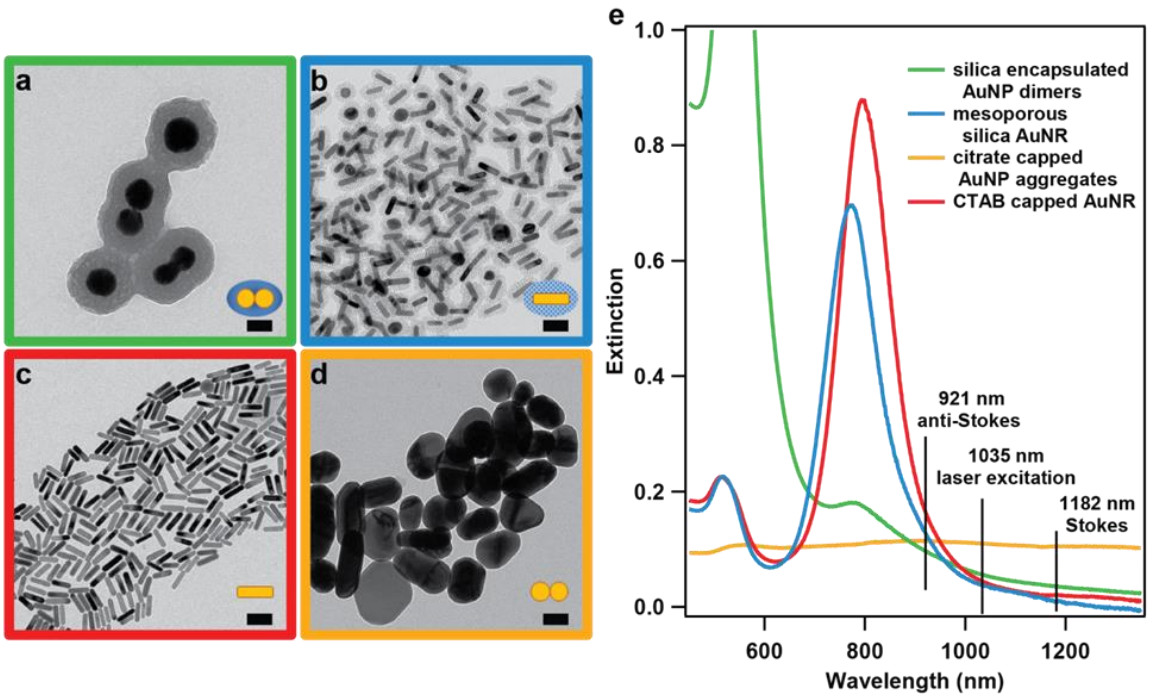

Figure 5.1 Sample characterization (a-d) Transmission electron micrographs of each sample alongside schematic depiction. The scale bar is equivalent to 50 nm. (e) extinction spectrum of each sample showing the localized surface plasmon resonance, with relevant SERS wavelengths indicated. The anti-Stokes and Stokes wavelengths correspond to the ethylenic symmetric stretch of *trans*-1,2-bis(4-pyridyl)ethylene.

In Figure 5.1e, we show the extinction spectra depicting the localized surface plasmon resonance (LSPR) for each nanomaterial. The size of the samples was chosen to ensure that the localized surface plasmon resonance overlapped with the near infrared SERS probe beam. The two samples consisting of AuNRs show a transverse plasmon resonance at 515 nm, and a longitudinal plasmon resonance at 770 nm for the mesoporous silica AuNRs (blue) and 793 nm for the CTAB-capped AuNRs (red). The blue shift of the mesoporous silica AuNRs upon silica formation arises from the change in refractive index. For the silica encapsulated AuNP dimers (green), the monomer plasmon resonance occurs at 538 nm, with the multimer plasmon resonance centered at 782 nm. For the aggregated citrate-capped AuNPs (yellow), a small monomer plasmon resonance peak is present at 557 nm and the aggregate plasmon resonance is very broad, signifying a diverse population of aggregates and thus plasmonic hotspots available in this sample. The three wavelengths denoted on the plot refer to the relevant wavelengths for the SERS measurement. The laser excitation wavelength is 1035 nm, and the anti-Stokes and Stokes wavelengths for the 1200 cm^{-1} ethylenic symmetric stretch in BPE at this excitation wavelength occur at 921 nm and 1182 nm, respectively.

Representative anti-Stokes and Stokes Raman spectra for each sample, obtained at a flux of 350 W/cm^2, appear in Figure 5.2a and Figure 5.2b, respectively. Additional spectra were taken at fluxes ranging between 210 W/cm^2 and 1050 W/cm^2 for each sample (Figure C2-C5). The scale bar in the upper left corner denotes the relative signal magnitudes between the two sets of spectra and reports the signal intensity as counts/s. Four major peaks in BPE are marked by dotted lines and appear at 1015, 1200, 1608, and

1638 cm^{-1}. The 1608 and 1638 cm^{-1} modes correspond to the CC ring stretching modes, the 1200 cm^{-1} mode corresponds to the ethylenic symmetric stretch, and the 1015 cm^{-1} mode corresponds to the ring breathing mode.[64,140] The relative SERS signal magnitudes track with the LSPR magnitudes of each sample (Figure 5.1e), which is most apparent when comparing the Stokes SERS magnitude of the AuNP aggregates to the other samples. The Stokes SERS signal magnitude for the AuNP aggregates is approximately 10x higher than any other sample and also has the highest LSPR magnitude for both the laser excitation wavelength and the Raman Stokes wavelength corresponding to the 1200 cm^{-1} mode (Figure 5.1e). For quantitative analysis of vibrational energy deposition, we account for the LSPR magnitude differences as described in the following paragraph and will focus our analysis on the most intense peak at 1200 cm^{-1} for all samples.

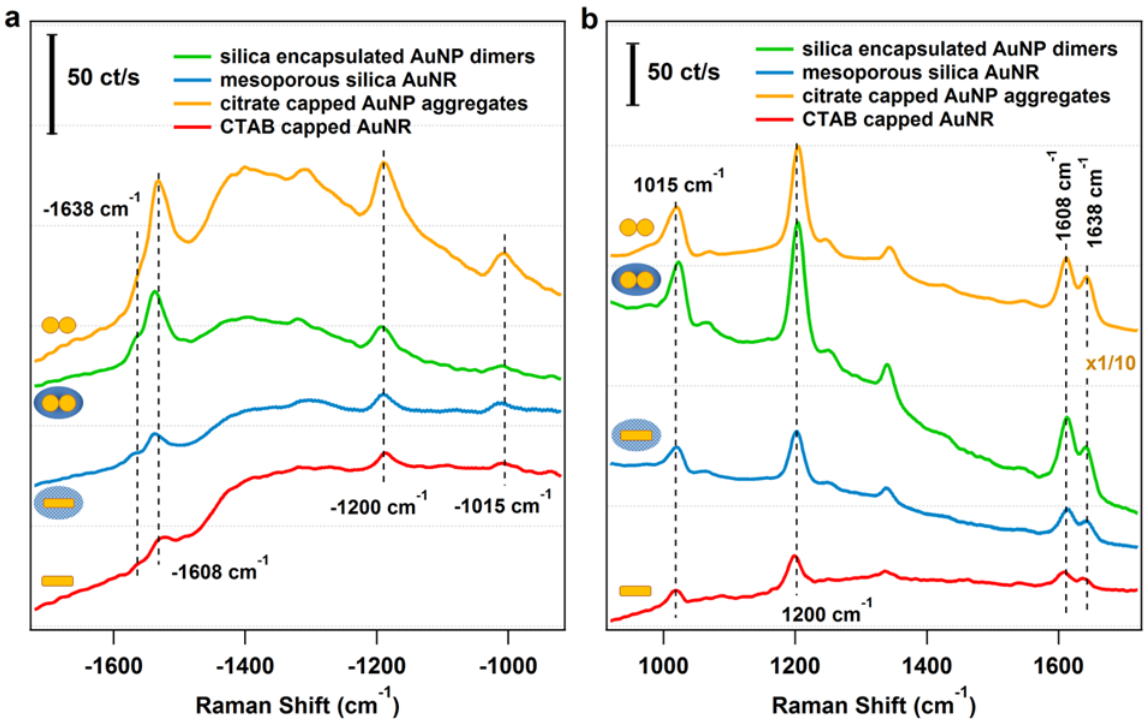

Figure 5.2 Surface enhanced (a) anti-Stokes and (b) Stokes Raman spectra obtained with a picosecond probe beam at 350 W/cm^2.

During both plasmon excitation and SERS probing, energy is transferred from the photoexcited plasmon to the vibrational levels of the molecular adsorbates. To calculate the effective temperature of reporter molecules in each sample, we apply a Boltzmann distribution analysis. From the spectra obtained in Figure 5.2, we fit the 1200 cm^{-1} peak to a Gaussian function to obtain the peak amplitude. We account for the wavelength dependent enhancement in SERS[101] by scaling the peak amplitude with respect to the LSPR magnitude at the wavelength relevant to the Raman signal for each mode (Figure 5.1e). We also include an additional scaling factor to account for the wavelength dependence of the detector efficiency at each wavelength. We then apply a Boltzmann distribution as described in Equation 5.1:[136]

$$\text{Effective Temperature (K)} = \frac{-\text{Energy of Vibration (J)}}{k_b * \ln\left(\frac{\text{Intensity}_{\text{anti-Stokes}}}{C * \text{Intensity}_{\text{Stokes}}}\right)} \quad (5.1)$$

where k_b is the Boltzmann constant, and C accounts for the wavelength dependence of Raman scattering. From the Boltzmann distribution, we obtain an effective temperature for each sample. We then can apply this analysis to our ultrafast SERS technique to track energy deposition into the adsorbates as a function of time on the picosecond time scale. Due to the ultrafast time scale, the system is no longer at equilibrium, thus we report the energy deposition as an effective temperature, equivalent to the vibrational kinetic energy deposited into the vibrational mode of the adsorbate.

Using ultrafast SERS, we track the energy deposition into the ethylenic symmetric stretch of the molecular probe after pump-induced photoexcitation to examine the effect of silica supports on energy partitioning after plasmon excitation (Figure C1). By

applying the Boltzmann distribution analysis, we can plot the time-resolved response (Figure 5.3a), which displays the transient effective temperature following photoexcitation for the two silica coated samples and the citrate-capped AuNP aggregates. Due to a strong scattering background, we were unable to fit the ultrafast SER spectra for the CTAB-capped AuNRs. In addition to the effective temperature plots for the three substrates, Figure 5.3a also shows two response functions. The instrument response function, as measured by the optical Kerr effect in toluene, determines the time resolution of the instrument and is shown as the gray dashed Gaussian peak. The solvent response (grey), as measured by monitoring the 818 cm^{-1} peak in isopropyl alcohol (IPA) of a sample containing aggregated gold nanoparticles suspended in IPA with no analyte, shows the amount of heating due to only the intensity of the two pulsed laser beams. The solvent response shows minimal heating due to the laser pulses and has no time dependent features.

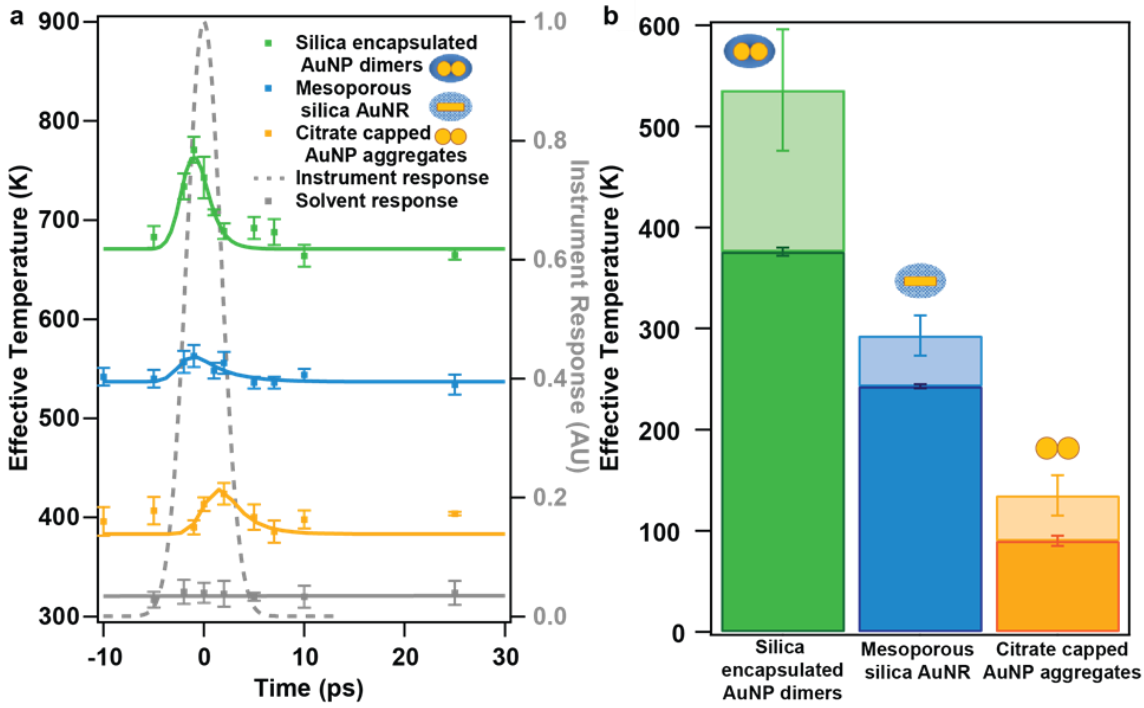

Figure 5.3 Energy deposition into the ethylenic symmetric stretch of *trans*-1,2-bis(4-pyridyl)ethylene (a) for silica encapsulated AuNP dimers (green) and mesoporous silica AuNRs (blue), and citrate-capped AuNP aggregates (yellow) excited with 50 W/cm^2 photoexcitation pulse (b) Comparison between the effective temperature baseline (darker bars) and transient effective temperature changes (lighter bars) from room temperature (294 K) for silica encapsulated AuNP dimers, mesoporous silica AuNRs, and citrate-capped AuNP aggregates

In Figure 5.3a, each sample is photoexcited with a 50 W/cm^2 (8 MW/cm^2) 1035 nm femtosecond pump pulse and the spectra are collected with a 350 mW/cm^2 picosecond probe pulse. As can be seen in Figure 5.3a, each sample has a baseline effective temperature elevated from room temperature, even at negative time points well before pump-induced photoexcitation. This baseline effective temperature arises due to plasmonic heating from the SERS probing process and correlates to the overall efficiency of energy deposition into the adsorbate due to coupling between the plasmon and the specific vibrational mode.[136] Upon photoexcitation, the effective temperature for the samples increases and, surprisingly, the energy dissipates extremely quickly. By fitting

each peak to a Gaussian function convoluted with an exponential function, we can extrapolate out a time constant for each substrate. For the silica encapsulated AuNP dimers, the time constant is 1.1 ± 0.5 ps, while the time constant for the mesoporous silica AuNRs is 3 ± 2 ps. These values are similar to those obtained for AuNP aggregates,[136] and are within the instrument response. This energy clearly dissipates very quickly from the adsorbates and must transfer to the environment around the adsorbates, which may include the surrounding ligands, solvent, silica shell, or most likely back into the gold nanostructure. The addition of silica and mesoporous silica does not appear to affect the dynamics of the plasmonic heating response on the picosecond time scale. However, the silica and mesoporous silica coated samples exhibit different behaviors in regard to overall effective temperature differences.

In Figure 5.3b, we compare the baseline effective temperature and the transient effective temperature differences for each sample in Figure 5.3a relative to room temperature (294 K). The darker bars represent the baseline effective temperature that arises due to the SERS probing process and the lighter bars represent the effective temperature change upon pump-induced photoexcitation. In the silica encapsulated AuNP dimers, the transient effective temperature upon photoexcitation rises by over 100 K, while the mesoporous silica AuNRs have transient effective temperature differences that are much lower, at approximately 40 K. The silica and mesoporous silica samples also have baseline effective temperatures which differ by 120 K. Adsorbates on the citrate-capped AuNP aggregates have an even lower baseline effective temperature, which is 150 K lower than adsorbates on the mesoporous silica AuNRs. The temperature

differences of the baseline effective temperature between these substrates must arise from a difference in the thermal properties of the local environment around the adsorbates.

To further explore the effect of the local environment on the steady state heating response seen in the different baseline effective temperatures, we obtained spectra for the four samples in Figure 5.2 at a range of SERS probe powers (Figure C2-C5). Effective temperatures for each sample at each flux, obtained by applying the Boltzmann distribution analysis described previously, appear in Figure 5.4 for the 1200 cm^{-1} ethylenic symmetric stretch. The solvent response is shown in grey and represents aggregated gold nanoparticles suspended in IPA. The effective temperatures are obtained by fitting the 818 cm^{-1} peak in IPA. The solvent response shows minimal heating due to the probe pulse with an average effective temperature of 320 ± 10 K over the range of fluxes measured.

For all samples, the effective temperatures increase linearly with increasing flux, suggesting a one photon process for the energy transfer. Although all of the samples have increasing effective temperatures with increased flux, the slope of the temperature increase as a function of laser power is dramatically different. Adsorbates on silica encapsulated AuNP dimers (green) and the mesoporous silica AuNRs (blue) experience significantly higher temperatures than the adsorbates on the particles without a silica shell across all fluxes. By fitting the data for each sample to a linear regression, we can extrapolate out the baseline temperature for each system. The baseline temperature describes the relative energy deposition into each mode for each nanoparticle substrate. The difference in baseline temperatures between the silica and mesoporous silica substrates and the ligand-capped particles range from 130 to 250 K (Table 5.1). The higher temperatures achieved in the presence of an oxide

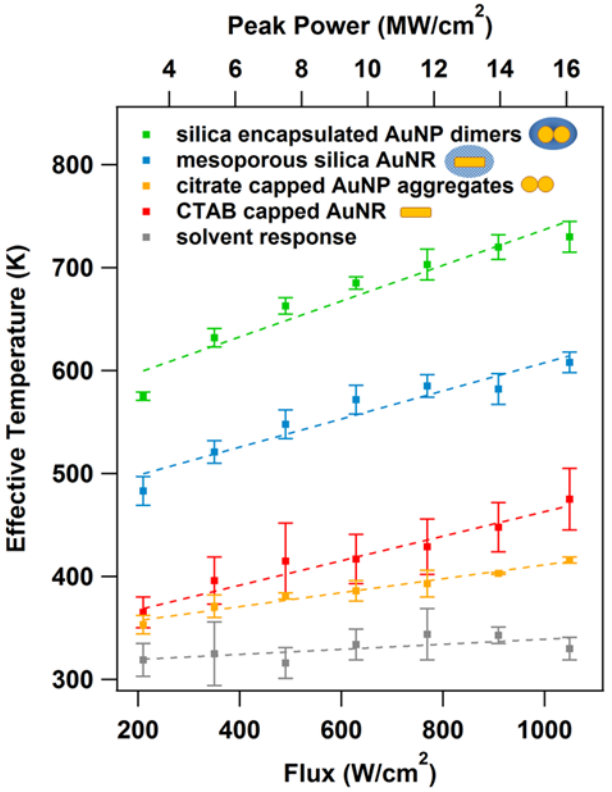

Figure 5.4 Localized plasmonic heating for silica coated and ligand coated samples. Temperature of the ethylenic symmetric stretch (1200 cm^{-1}) of *trans*-1,2-bis(4-pyridyl)ethylene (BPE) for each plasmonic substrate plotted against flux and peak power of the picosecond probe beam. BPE on particles encapsulated in silica have higher temperatures than those molecules on particles without silica.

support suggests that the role of heating in plasmonic photocatalysis may vary based on the presence and composition of the support.

Table 5.1 Effective temperatures at select fluxes for each substrate with corresponding thermal conductivity and specific heat capacity values

	Citrate-capped AuNP Aggregates	**CTAB-capped AuNRs**	**Mesoporous silica AuNRs**	**Silica encapsulated AuNP dimers**
Temperature (K) at 210 W/cm^2	353 ± 9	365 ± 15	483 ± 14	575 ± 4
Temperature (K) at 350 W/cm^2	371 ± 11	396 ± 23	521 ± 11	632 ± 9
Temperature (K) at 1050 W/cm^2	416 ± 3	475 ± 30	608 ± 10	730 ± 15
Baseline Temperature (K) (Figure 5.4)	343 ± 3	349 ± 6	470 ± 10	563 ± 15
Thermal Conductivity (W/m K)	0.2 – 0.3**	0.22 – 0.24[141,142]	0.2 – 0.3[143,144]	1.0 – 1.4[145,146]
Specific Heat Capacity (J/ K)	1.3 – 4.18** g^{-1}	1.6 – 4.18 mL^{-1} [141,142]	0.8 – 1.4* g^{-1} [147]	0.733 g^{-1} [147]

*Heat capacity for mesoporous silica AuNRs were estimated based on pore size where the range given estimates a 25-33% solvent (EtOH) contribution to the heat capacity
**Estimated citrate-capped AuNP thermal property values based upon measurements of other ligand shells, including CTAB, PEG, and polystyrene[141,148,149]

There are several possible explanations for the observed effective temperature differences in these four nanoparticle materials, which likely result from the different thermal properties of the encapsulant material. A key component of nanoscale thermal transport is the thermal conductivity of a material.[150] However, the heating response observed in Figure 5.4 cannot be fully explained by thermal conductivity due to the

reported values for thermal conductivity of the media surrounding each sample (Table 5.1). For these values, silica has the highest thermal conductivity and the mesoporous silica has one of the lowest.[145,151] If thermal conductivity fully explained the heating response for the various local environments, the adsorbates on the silica encapsulated AuNP dimers would have the lowest effective temperatures, while the adsorbates on the mesoporous silica AuNRs would have the highest temperatures. The ligand capped nanoparticle substrates would fall somewhere in between the silica and mesoporous silica samples.

The more likely explanation for the dramatic temperature differences between the ligand coated and silica coated samples is the different heat capacities of the surrounding media. Nanoscale silica materials have specific heat capacities below 1 J/g K,[147] whereas solvents typically have higher heat capacities. In these specific nanomaterials, the estimated specific heat capacity for the silica in the coated silica samples ranges from 0.73 to 0.84 J/g K,[147] depending on porosity, and the heat capacity of the ligand coated substrates can range between 1.6 J/mL K and 4.18 J/g K (Table 5.1 & C2).[141] Additional information about the heat capacity estimates for these samples can be found in Appendix C. In Raman thermometry, the molecule adsorbed to the surface of the metal acts as a thermometer at the interface between the gold surface and the environment surrounding the gold particle. As the environment around the gold particle changes, through the addition of protective oxide layers, or changes in solvent and capping ligands, the molecule can report on the effects of these changes through the spectra we obtain. If the local medium from a material around the gold nanoparticle has a high heat capacity, the

temperature reported by the adsorbed molecule is relatively small. With a high heat capacity, a large amount of energy is needed to increase the temperature of the material. If the local medium has a lower heat capacity, less energy is required to raise the temperature of the material to the same degree. The reporter molecule, surrounded by a material with a lower heat capacity, experiences a larger change in temperature, even when the same amount of energy is added to the system. Thus, the temperature differences arising between the silica coated and ligand coated samples is likely due to the heat capacity of the medium surrounding the adsorbates.

In Figure 5.4, it is clear that the energy deposition into molecular adsorbates on silica and mesoporous silica samples differs by ~ 100K. This difference is not accounted for by the different shape of the particles or hot spots between the two sample types, as can be seen with the comparison between the ligand capped nanoparticle aggregates and nanorods. The most likely cause for the temperature differences between the silica encapsulated AuNP dimers and mesoporous silica AuNRs is in the structural differences of the silica coating leading to changes in the overall heat capacity. The mesoporous silica coating consists of pores with diameters approximately 7 ± 3 nm. These pores allowed for the migration of the analyte to the gold surface, and also contain solvent molecules. The addition of solvent to the silica structure changes the thermal properties of the material as experienced by the adsorbates.[152] Essentially the heat capacity for the mesoporous silica, as perceived by the adsorbates, becomes a weighted average between the mesoporous silica (~0.8 J/g K) and the solvent, ethanol (2.46 J/g K). Based on the pore size and surface area of the mesoporous silica shell, the solvent contribution for the

thermal properties of the mesoporous silica AuNRs is estimated to be between 25-33%. This change in the surrounding medium of the adsorbate results in the ~100 K difference between the two types of silica coated substrates. Thus, mesoporous silica coatings used for catalysis may also affect selectivity due to increased localized heating in the pores as compared to substrates without a mesoporous silica shell.

5.4 Conclusion

Here, we compared the plasmonic heating for adsorbates on gold nanostructures with local environments ranging from ligands (CTAB or citrate), a mesoporous silica shell, to a non-porous silica shell using ultrafast surface-enhanced Raman thermometry. Upon photoexcitation, the effective temperature, which corresponds to the vibrational kinetic energy, increased for silica and mesoporous silica samples and the energy quickly dissipated in less than 3 ps. The effective baseline temperatures, which arise from the SERS probing process, varied significantly between the silica, mesoporous silica, and ligand samples. The difference in heating response between the silica, mesoporous silica, and ligand coated substrates most likely arises due to differences in the heat capacity of the local environments around the molecules adsorbed to the gold surface. Clearly, silica supports affect the localized heating of molecules adsorbed to plasmonic surfaces and may also dramatically affect catalytic activity of plasmonic photocatalysts due to increased thermal contributions.

5.5 Methods

Sample Preparation. Gold nanoparticles (AuNPs) were synthesized *via* the Frens method.[84] Samples for SERS and ultrafast Raman thermometry measurements were prepared by centrifuging 3 mL of as-synthesized AuNPs and removing 2.95 mL of the supernatant. The AuNPs were aggregated by adding 350 µL of 0.032 M aqueous potassium nitrate and 50 µL of 0.18 mM *trans*-1,2-bis(4-pyridyl)ethylene dissolved in ethanol. Mesoporous silica gold nanorods (AuNRs) were synthesized following a modified Stöber method.[138] Synthetic details can be found in Appendix C. For SERS and ultrafast Raman thermometry measurements, 5 µL of 1.8 mM *trans*-1,2-bis(4-pyridyl)ethylene dissolved in ethanol were added to 200 µL of 6 x 10^{11} nanorods/mL of mesoporous silica AuNRs. Measurements were performed 12 hours after addition of analyte. Additional details can be found in Appendix C.

Ultrafast SERS Instrumentation. A detailed description of this instrument has been published previously.[136] Briefly, < 250 fs pulses from a fiber amplifier (Clark MXR, Impulse), centered at 1035 nm, were split with a 50:50 beam splitter to a make a photoexcitation and a probe beam. To generate the picosecond probe pulse, 6 W was sent into a grating filter.[153] The femtosecond photoexcitation beam used a remaining portion of the fundamental without further modification and the power was controlled with a neutral density filter wheel. The timing between the pulses was controlled by a motorized stage in the photoexcitation beam line. After the sample, the spontaneous Raman signal was focused into a spectrograph and dispersed by a 300 gr/mm grating blazed at 1 µm.

The signal was detected by a liquid N_2 cooled, 1024 pixel InGaAs array. Stokes and anti-Stokes spectra were collected using a 1064 nm Razor Edge filter (Semrock) and 1000 nm short pass (Thorlabs FESH1000) filter, respectively.

5.6 Acknowledgements

We thank Professor Xiaojia Wang (University of Minnesota) for helpful discussions. This material is based on work supported by the Air Force Office of Scientific Research under AFOSR Award No. FA9550-15-1-0022 and by the University of Minnesota Doctoral Dissertation Fellowship. Parts of this work were carried out in the Characterization Facility at the University of Minnesota, which receives partial support from the NSF through the MRSEC program (DMR-1420013).

Chapter 6

Plasmon-Enhanced Chemical Sensing and Conversion using Copper Selenide Nanoparticles

Reprinted with permission from manuscript by Xing Yee Gan, Emily L. Keller, Scott E. Crawford, Renee R. Frontiera and Jill E. Millstone. To be published.

6.1 Synopsis

The ability of plasmonic materials to enhance electromagnetic fields, produce energetic carriers, and generate heat holds tremendous potential for a variety of applications. However, traditional plasmonic materials, such as gold and silver, are less earth-abundant and have limited catalytic activity, while the properties of non-traditional materials are not well understood. Here, we investigate the SERS activity on colloidal degenerately-doped copper selenide semiconductor nanoparticles, a promising alternative plasmonic material due to their near IR plasmon resonance, sub-20 nm size, and different surface chemistry as compared to traditional plasmonic materials. We report that copper selenide nanoparticles have a SERS enhancement factor of 10^4. In the presence of light, the plasmon-driven dimerization of 4-nitrobenzenethiol to 4,4'-dimercaptoazobenzene occurs on the nanoparticle surfaces. Importantly, we quantify the SERS enhancement factor for and provide first observation of chemical detection and plasmon-mediated chemistry by these non-noble metal plasmonic substrates. Taken together, our results indicate that degenerately-doped semiconductor nanoparticles show tremendous promise in becoming cost-effective alternatives for plasmonic sensing and catalytic technologies in real-world applications.

6.2 Introduction

Localized surface plasmon resonances (LSPRs) have been broadly studied and are a property of nanomaterials that can be used to enhance or enable a wide variety of technologies including cancer treatment,[2,154] light-driven catalysis,[5,155] and ultrasensitive

detection.[34,89] While traditionally studied in noble metal nanomaterials, such as gold and silver, a broader selection of nanoscale materials support LSPRs.[156] Apart from being more earth-abundant and cost-effective alternatives, non-noble metal nanomaterials such as aluminum[157] and degenerately-doped semiconductor nanoparticles (i.e. metal oxides,[158] metal nitrides,[159] and metal chalcogenides[160,161]) enable plasmonic properties that span a wider range of the electromagnetic spectrum, from the ultraviolet to the infrared region. Similar to their noble metal counterparts, the observed LSPRs of degenerately-doped semiconductor NPs can be tuned via particle size,[156] shape,[162] and surface chemistry,[163] as well as by the additional handle of free carrier density and distribution.[164–166] However, it is yet unclear whether the plasmonic features of these alternative plasmonic materials will perform in a comparable, inferior, or superior manner to their noble metal counterparts.

A common plasmon-enhanced technique, frequently used to study noble metal nanomatierals in a variety of sensing applications, is surface-enhanced Raman spectroscopy (SERS).[34] The enhanced signal observed with SERS arises from the coupling of a material's LSPR with incoming resonant light and scattered Raman photons.[34] A common metric by which to compare SERS substrates is using an enhancement factor (EF), which estimates the order of magnitude enhancement of the normal Raman signal due to interaction with the plasmonic substrate.[13] The EF is a key component in determining the sensitivity of a chemical sensing device. For example, CuTe nanoplates and nanocubes have been reported to exhibit photothermal properties and a SERS EF of ~10^6.[167] However, to our knowledge, a SERS EF has not been reported

specifically for psuedospherical copper selenide ($Cu_{2-x}Se$) NPs, which is vital for determining the viability of these materials as chemical sensors.

Beyond sensing applications, another exciting avenue for plasmonic materials is the ability to drive selective photochemical catalytic reactions.[4] In traditional plasmonic materials, one decay pathway following plasmon excitation is the generation of energetic or hot carriers.[44,48,155] Though short-lived,[12,44] these energetic carriers can be transferred to adsorbates, where the adsorbates could be either a semiconductor,[26,168] a catalytically active secondary metal,[4,169] or a molecule.[11,12,44] Depending on the energy distribution, lifetime, number, and charge of the energetic carriers, a plasmonically-driven chemical conversion may occur.[48] While other plasmonic materials have driven various photocatalytic reactions, chemical conversions using plasmonically active degenerately doped semiconductor NPs alone have not yet been observed.[5,44,155,170] Instead, several reports have observed that hybrid structures made from plasmonically active semiconductor NPs and catalytically active metals could be used to enhance catalytic efficiencies.[171] For example, Cui and coworkers have reported that by decorating plasmonic copper sulfide NPs with catalytically active metals such as Pt and Pd, chemical conversions such as the reduction of CO_2 and Suzuki coupling reactions were enhanced.[172]

In the present work, we demonstrate that degenerately-doped $Cu_{2-x}Se$ NPs with an LSPR in the near infrared (NIR) region can be used to enhance the Raman signatures of analyte molecules using SERS. By measuring the enhanced amplitudes of the Raman peaks, we report a SERS EF. We then demonstrate the functionality of this optical

response, by monitoring the plasmon-mediated chemical conversion of 4-nitrobenzenethiol to 4,4'-dimercaptoazobenzene. Importantly, these observations show the efficacy of semiconductor NPs as one of the non-noble metal alternatives in plasmonic technologies.

6.3 Results and Discussion

We prepared $Cu_{2-x}Se$ NPs *via* a hot injection method according to a modified literature procedure using standard air-free techniques (see Appendix D for experimental details).[165,173] Briefly, this synthesis produces colloidally stable $Cu_{2-x}Se$ NPs with oleylamine (OAm) acting as the surface passivating ligands. Similar to what was reported previously, transmission electron micrographs show that purified OAm capped $Cu_{2-x}Se$ NPs are pseudospherical in shape with an average diameter of 16.4 ± 1.5 nm

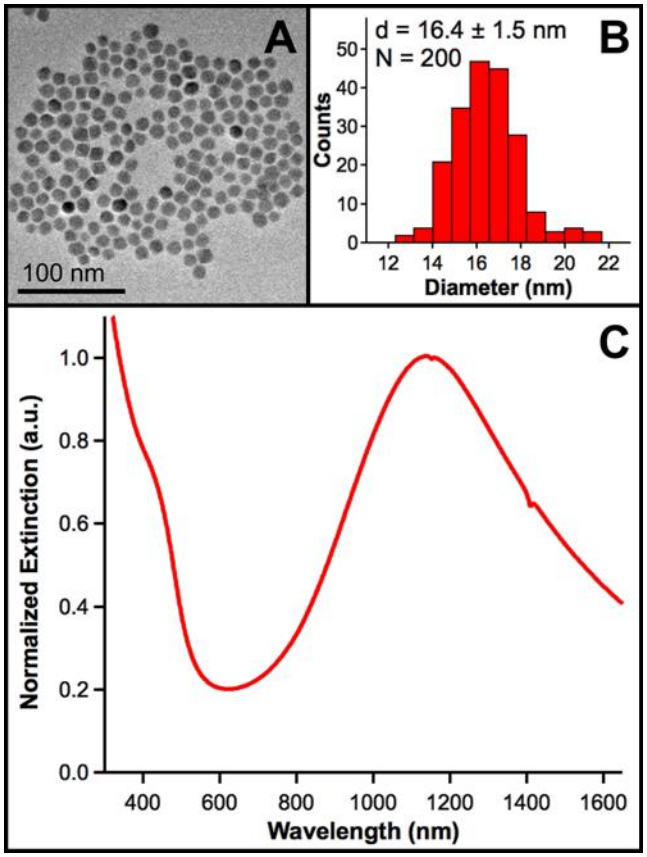

Figure 6.1 Characterization of $Cu_{2-x}Se$ NPs *via* transmission electron microscopy and UV-Visible-NIR spectroscopy. (A) High resolution transmission electron micrograph shows monodispersed, pseudospherical oleylamine capped $Cu_{2-x}Se$ NPs (B) with its size distribution represented in the histogram, and (C) extinction spectrum of the NPs dispersed in $CHCl_3$.

(Figure 6.1A-B) and an antifluorite crystal structure (Figure D1, PDF # 00-006-0680).[165] When the NPs are exposed to ambient conditions, the NPs undergo a self-doping process where Cu^{+} is oxidized to Cu^{2+}, which results in the formation of valence band holes.[156] The presence of degenerate holes generates an LSPR at approximately 1100 nm and an onset of absorption at approximately 500 nm which we assign to the direct bandgap of $Cu_{2-x}Se$ NPs (Figure 6.1C). The concentration of degenerate holes formed in the NPs (i.e. carrier density, N_h) can be extracted from the extinction spectrum and quantified using the Drude model ($N_h = 6.3x10^{21}$ cm^{-3}).[156,158,165]

Next, we examined the interactions between the LSPR of $Cu_{2-x}Se$ NPs and Raman active molecules using SERS. Here, we introduce benzenethiol (BT) solutions of various concentrations to a $CHCl_3$ solution containing colloidally dispersed OAm capped $Cu_{2-x}Se$ NPs. BT acts as a reporter molecule for the SERS measurement and Figure 6.2A depicts the resulting SER spectra in various shades of red. The grey spectrum represents the unenhanced Raman spectrum of BT in $CHCl_3$ without the presence of plasmonic $Cu_{2-x}Se$ NPs. The peaks marked by the dashed lines correspond to the BT ring breathing modes at 1002 and 1024 cm^{-1}.[88] Additionally, the black spectrum in Figure 6.2A is a control sample consisting of $Cu_{2-x}Se$ NPs without BT dispersed in $CHCl_3$. Note that the spectral region at 1000 cm^{-1} does not exhibit BT features that appear in solutions containing BT.

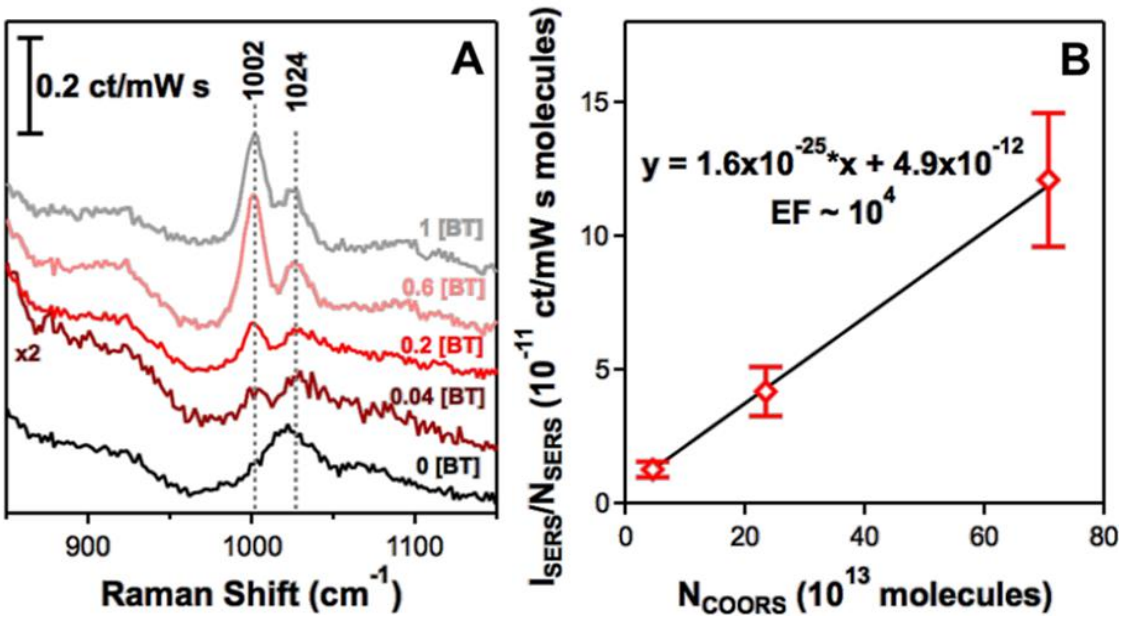

Figure 6.2 Determination of the enhancement factor for $Cu_{2-x}Se$ NPs using benzenethiol (BT) as a reporter molecule (A) SER spectrum of BT adsorbed onto colloidal $Cu_{2-x}Se$ NPs at indicated concentrations and (B) linear fit of the SERS intensity per molecule versus BT molecules in solution from which the enhancement factor is extrapolated as 10^4 for $Cu_{2-x}Se$ NPs.

From the spectra in Figure 6.2A, we can calculate a SERS EF for $Cu_{2-x}Se$ NPs using the equation described below:[13,125]

$$EF = \frac{I_{SERS}N_{NRS}}{N_{SERS}I_{NRS}} \tag{6.1}$$

where I_{SERS} and I_{NRS} are the Raman intensities of BT at 1002 cm^{-1} for the SERS and normal Raman measurement, respectively, while N_{SERS} and N_{NRS} correspond to number of BT molecules adsorbed on the plasmonic substrate and in solution, respectively, for the probed volume. The spectra in Figure 6.2A consist of samples with the same particle concentration, thus we can assume that N_{SERS} is the same for the three samples, due to the

excess BT in solution. Nonetheless, since there is an increase in concentration of excess BT in solution in each aliquot, the signal intensity in I_{SERS} also increases.

The ratios between I_{SERS} and N_{SERS} plotted against the number of excess BT molecules (N_{NRS}) that would be present in the probed volume if there were no NPs in the sample at various BT aliquots can be fit to a linear regression (Figure 6.2B). Using the y-intercept of the fitted linear regression, we can extrapolate an idealized I_{SERS}/N_{SERS} ratio that accounts for the excess BT in solution. By using this ratio in Equation 1 and reporting only to the order of magnitude due to estimates of surface area and surface packing, we calculated an EF of 10^4 for $Cu_{2-x}Se$ NPs. Further details for quantifying the SERS EF for $Cu_{2-x}Se$ NPs can be found in Appendix D. This EF is comparable to traditional noble metal SERS substrates, which have EFs between 10^3 and 10^7 depending on size, shape and aggregation conditions.[13]

Scheme 6.1 Depiction of plasmonically driven chemical conversion from 4-NBT to DMAB.

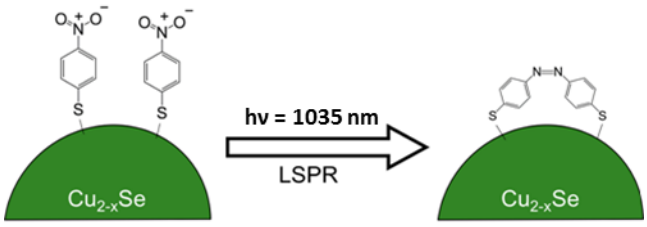

In addition to having a measureable SERS EF, $Cu_{2-x}Se$ NPs can mediate the plasmon-driven dimerization of 4-nitrobenzenethiol (NBT) to 4,4'-dimercaptoazobenzene (DMAB), shown in Scheme 6.1 (*N.B.* the schematic shows the adsorption of both NBT and DMAB molecules on a bare NP for clarity.) NBT

dimerization is a plasmon-mediated reaction that is well-characterized on noble metal plasmonic substrates and is known to be mediated by the generation of plasmon-derived hot electrons to initiate the multi-electron reduction reaction.[85,125] Upon irradiation of a solution containing NBT adsorbed to either OAm capped (navy) or polyvinylpyrrolidone (PVP) capped (teal) $Cu_{2-x}Se$ NPs dispersed in $CHCl_3$, a DMAB product peak appears at 1458 cm^{-1} in the SER difference spectra within 5 minutes of photoirradiation (Figure 6.3, D5). The spectra in Figure 6.3 indicate that the presence of a bulky polymeric ligand (e.g. polyvinylpyrrolidone) on NP surface does not inhibit the absorption of NBT, nor the dimerization process. The highlighted NBT modes (black dashed lines) at 1102, 1344, and 1580 cm^{-1} correspond to the ring breathing, NO_2 symmetric stretch and C-C stretch,[88] respectively, and match the normal Raman spectrum shown in light grey (Figure 6.3). The product peak at 1458 cm^{-1}, which is labelled in red, corresponds to the N=N stretch of DMAB. DMAB does not form without the presence of

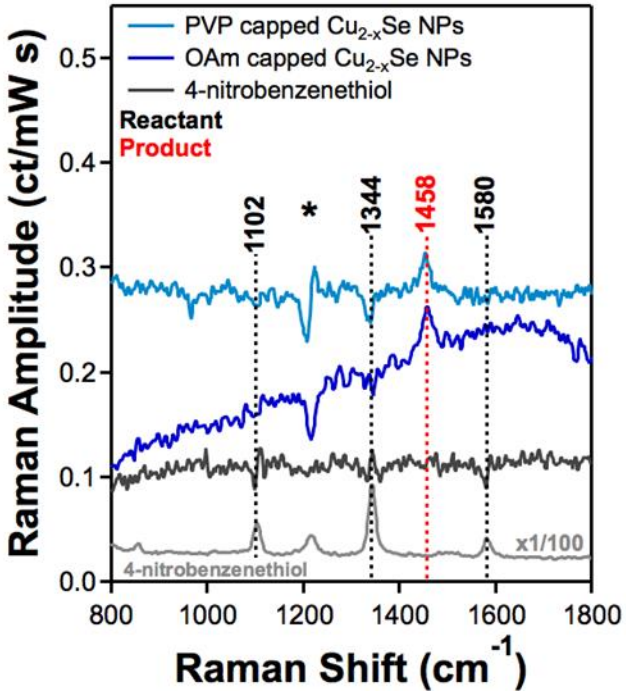

Figure 6.3 SER difference spectra of PVP (teal) and OAm (navy) capped $Cu_{2-x}Se$ NPs, as well as 4-NBT in absence of NPs (dark grey) showing the plasmon-driven dimerization of 4-nitrobenzenethiol (black dashed lines) to 4,4'-dimercaptoazobenzene (red dashed lines). Light grey spectrum shows Raman spectrum for NBT.

plasmonically active $Cu_{2-x}Se$ NPs at the concentrations used for this experiment as shown by the dark grey spectrum in Figure 6.3 (Figure D6). The photoinduced dimerization of NBT is the first reported evidence of plasmonically driven chemical conversion using plasmonic semiconductor $Cu_{2-x}Se$ NPs.

This plasmon-driven chemical conversion is particularly remarkable because the dimerization of NBT undergoes a reduction based mechanism (i.e. hot electrons by noble metal NPs),[11] while the LSPRs of $Cu_{2-x}Se$ NPs are generated by the coherent oscillation of delocalized holes in the valence band. Though these particles primarily produce hot holes, the electrons of the initial electron-hole pairs may be energetic enough to drive these reactions, even though they are not as energetic as hot electrons produced on noble metals. We can estimate a percent yield for this reaction by comparing the final peak amplitude ratio of the 1344 cm^{-1} reactant peak and the 1458 cm^{-1} product peak in Figure D5. The percent yield for this reaction on $Cu_{2-x}Se$ NPs is 24 ± 3%, which is comparable to that seen with SERS on gold nanoparticles.[125] This estimate implies that the reaction goes to completion as limited by the sterics of the proximity of two nitro groups. Further studies need to be conducted using different Raman analytes to probe the efficacies of using hot holes in $Cu_{2-x}Se$ NPs to promote plasmonically powered chemical conversion.

6.4 Conclusion

In summary, we demonstrate that degenerately doped $Cu_{2-x}Se$ NPs exhibit LSPRs that enhance Raman signatures of adsorbed molecules, with an enhancement factor of 10^4, which is comparable for sensing applications. More importantly, this is the first reported SERS EF for $Cu_{2-x}Se$ NPs and the first observation of plasmon-mediated dimerization of NBT using these alternative plasmonic NPs. Taken together, this is a substantial leap forward towards the transition to non-noble metal, specifically semiconductor, alternatives in the commercialization of plasmonic technologies.

6.5 Acknowledgements

This work was supported by the Defense Threat Reduction Agency (Grant No. HDTRA1-16-1-0044, X.Y.G., J.E.M.) and the Air Force Office of Scientific Research (AFOSR Award No. FA9550-15-1-0022, E.L.K., R.R.F.). X.Y.G. acknowledges support from Pittsburgh Quantum Institute Graduate Research Fellowship, E.L.K. acknowledges support from University of Minnesota Doctoral Dissertation Fellowship, and S.E.C. acknowledges support from National Energy Technology Laboratory Professional Internship Program. We thank Dr. Michelle Ward for the generous access to the ICP-OES.

Chapter 7

Prospects

7.1 Absorption-Induced Plasmonic Heating

Most plasmonic photocatalysts reported in the literature drive reactions with visible light.[4,5,105,109] Visible wavelengths are preferable for light-driven catalysis due to their abundance in the solar spectrum. However, the scattering and absorption efficiencies of plasmonic materials is dependent on the specific wavelength, which leads to changes in the efficiencies of a variety of plasmonic processes, including hot carrier generation and heating. Recently, a group monitoring the plasmon-driven oxidation of ferrocyanide to ferricyanide by scanning electrochemical microscopy (SECM) separated the catalytic contribution between plasmon-generated hot carriers and plasmonic heating.[174] They measured temperature changes between 0 to 30 K on gold substrates excited with 532 nm at significantly lower fluxes than discussed in Chapter 4.[175] One of the primary differences between the SECM experiments and the work in the previous chapters is the excitation wavelength. The different excitation wavelength have different scattering and absorption efficiencies, which affects plasmonic heating. The work presented in previous chapters only addresses scattering-induced plasmonic heating, and further examination of absorption-induced heating is needed to truly account for the effect of heating processes on plasmonic photocatalysis.

There are several possible approaches for these types of studies, including modifying the plasmonic substrate so that we are able excite and probe the same subset of adsorbates using visible photoexcitation, and modifying the instrument used to obtain Raman thermometry data in the visible region. I will discuss these two approaches below.

The first approach uses AuNRs or another plasmonic substrate with a controlled plasmon resonance, such that the wavelengths over which excitation and probing of the adsorbates on the plasmonic substrate occurs are dependent on the same plasmon mode. By exciting and probing the same plasmon mode, the measurements will sample the same subset of adsorbates on the plasmonic substrate. Using AuNRs similar to those discussed in Chapter 5, the longitudinal plasmon resonance is centered around 800 nm. This plasmon resonance is primarily responsible for SERS signal obtained upon probing at 1035 nm. By tuning the pump wavelengths, using a non-colinear parametric amplifier (NOPA), between 650 to 850 nm (described in Chapter 3), we will be able to measure the effective temperature at several points across the plasmon resonance of the AuNRs. Using UV-Vis spectroscopy, we can extract the contribution of absorption and scattering in the extinction spectrum from the AuNRs, and relate that to the heating measured using our ultrafast Raman thermometry technique. From these measurements, I expect the effective temperatures to increase as the pump wavelength becomes more visible if absorption plays an important role in plasmonic heating.

Another approach to examine absorption-induced heating would be to perform the analogous experiment to the one in Chapter 4, but at a visible wavelength by modifying the ultrafast SERS instrument. In Figure 4.3a, I describe an experiment with a cross-polarized pump beam at 518 nm and observe no transient temperature changes in the adsorbates due to the pump transferring energy to a different subset of adsorbates. By modifying the ultrafast SERS instrument, we can double the picosecond probe pulse through second harmonic generation by focusing the beam into a BBO crystal to generate

a probe pulse at 518 nm. This modification would allow us to pump and probe the same set of adsorbates using a visible beam where absorption-induced heating may play a larger role than scattering-induced heating.

From these experiments, we can quantify the absorption-induced plasmonic heating and combine it with our measurements of the scattering-induced plasmonic heating to determine the overall degree of plasmonic heating. Based on reports in the literature,[8,175] I suspect that the absorption-induced heating will be higher than that observed for scattering-induced heating processes.

7.2 Mode-Specific Energy Transfer to Adsorbates on Plasmonic Materials

Mode-specific energy transfer is an exciting potential application of molecular-plasmonic systems. One goal of selective chemical catalysis is the ability to preferentially transfer energy into a specific bond of an analyte to drive a chemical reaction.[120] This selective energy transfer may be possible with plasmon-molecule coupled systems. Selective plasmonic energy transfer may occur in several ways, including the coupling of a molecule-plasmonic material that generates hybridized orbitals that have a preferential resonance with a specific mode,[124] or through orientation of the molecule in the hot spot, where the energy transfers directly from the plasmonic surface to the adsorbed molecules *via* localized plasmonic heating.

To monitor mode-specific energy transfer in plasmonic-molecular systems, we need to be able to measure the energy flow into and through the adsorbates. As discussed in Chapter 4, the time resolution of the current instrument was unable to detect

intravibrational redistribution (IVR) within the two plasmon-molecule systems studied. Based on the comparison to IVR time scales in non-plasmonic systems, which occurs within 1-2 ps of photoexcitation with similar molecules,[127] the time scale for IVR for molecules adsorbed to plasmonic substrates may be faster than the time resolution of the current instrument as discussed in Chapter 4. The time resolution of the ultrafast SERS instrument is limited due to the inverse relationship between time and frequency, where an improvement in time resolution would lead to a decrease in spectral resolution. A possible solution would be to employ a stimulated Raman technique,[176] like SE-FSRS (discussed in Chapter 2), which has femtosecond time resolution. The enhanced time resolution would allow for the tracking of energy as it flows through the molecule and may provide insights into what type of energy transfer leads to plasmon-mediated catalysis.

Mode-specific energy transfer may also occur at later times after plasmon excitation. As discussed in Chapter 2, plasmons eventually dissipate their energy as heat in tens to hundreds of picoseconds.[80] In transient absorption studies of plasmonic nanoparticles,[79] the spectra showed a beating pattern at later time points associated with the breathing of the hot metal lattice after electron-phonon scattering.[9] As the metal lattice cools, some of this energy may transfer to adsorbed molecules on the surface. However, it is unknown if this energy would transfer preferentially to modes associated with bonds closet to the plasmonic substrate and then dissipate across the molecule or if the transferred energy would follow a different pathway. While this dissertation focuses upon early time dynamics of plasmonic heating, the current instrument can examine

dynamics up to 250 ps after plasmon excitation. If energy transfers from the phonon modes of the metal into the adsorbates, the spectra obtained from the molecules should reflect similar beating patterns as those observed in the transient absorption studies.

Preliminary studies of mode-specific energy transfer examined the transfer of energy from aggregated AuNPs to adsorbed 7-(trifluoromethyl)quinoline-4-thiol (CFQ) molecules between -10 and 200 ps. Similar to the experiments described in Chapter 4, the sample was photoexcited at 518 nm, and spectra were obtained with a 1035 nm probe pulse (Figure E2). The spectra were analyzed using a Boltzmann distribution analysis to obtain Figure 7.1. For these data, the effective temperature at each time point is normalized with respect to the temperature for each mode measured in the pump off spectrum. Thus, the scale bar reports the change in relative energy (Δ Energy) between the various modes and time points. As can be seen in Figure 7.1, three of the four modes for CFQ show no change in energy upon photoexcitation. However, the 751 cm^{-1} mode

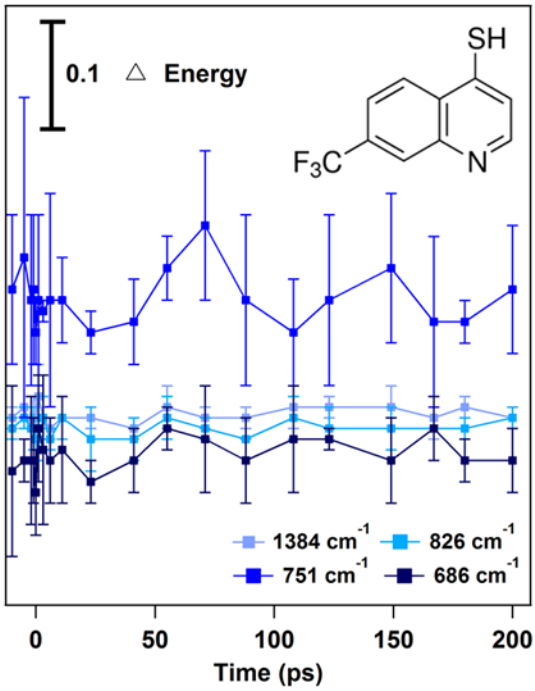

Figure 7.1 Energy distribution of various modes of 7-(trifluoromethyl)quinoline-4-thiol (CFQ, inset) adsorbed to aggregated AuNPs upon photoexcitation at 518 nm. Energy appears to transfer from the metal phonon mode to only one mode in CFQ.

exhibits an elevated baseline as well as oscillatory features after 50 ps. Potentially, these oscillations may arise from the breathing of the hot metal lattice, similar to the transient absorption studies mentioned previously.

Unfortunately, this experiment requires further optimization before any conclusions can be reached. The error bars for the 751 cm^{-1} mode are quite large and arise from sample instability over the course of the measurement. Sample stability for anti-Stokes and Stokes measurements is critical for extracting any useful information from the system. Additionally, sample heterogeneity also affects the resolution of the later time dynamics in these systems. Multiple samples exhibit these oscillatory features, however, the dynamics are slightly offset from each other (Figure E3), which makes sample averaging difficult. To monitor mode-specific energy transfers, further work needs to be done to optimize sample preparation, which may involve choosing a different analyte and plasmonic substrate for this measurement. By comparing various modes of an adsorbate, we can determine how energy transfers from the plasmonic substrate and flows through the molecules, leading to a better understanding of plasmon-molecule interactions that may occur during plasmonic photocatalysis.

7.3 Alternative Materials for Plasmonic Photocatalysis

Alternative plasmonic materials are of a great interest as they are more abundant, cost-effective, and support broader LSPRs, as compared to more traditional materials.[177] These alternative materials include aluminum,[157] metal oxides,[158] metal nitrides,[159] and metal chalcogenides.[160] The application of non-traditional plasmonic materials may

increase the viability of plasmonic processes for industrial applications due to newly accessible surface chemistry and plasmon decay pathways. While further characterization is needed, these new and exciting materials will allow for the increased efficacy of plasmonic materials in a broad range of applications.

In Chapter 6, I discussed the recent application of $Cu_{2-x}Se$ NPs as a plasmonic substrate capable of plasmon-mediated NBT dimerization that can be monitored with SERS. These initials measurements are extremely promising for the future application of these particles towards plasmonic photocatalysis. Unlike traditional plasmonic materials, like gold and silver, the plasmon supported by $Cu_{2-x}Se$ NPs consists of excess holes in the valence band, generated by copper deficiencies introduced during synthesis.[156] Upon photoexcitation, the plasmon is the collective oscillation of the excess holes in the valence band. The plasmon then decays to generate hot holes instead of hot electrons, which arise in more traditional materials.[178] Thus, $Cu_{2-x}Se$ NPs show promise as photocatalysts for oxidation reactions, like alcohol oxidation or ethylene epoxidation. Additionally, we can potentially quantify the hot holes produced upon plasmon excitation by using a hole acceptor, like catechol, as an analyte. By monitoring Raman modes of catechol for frequency shifts, we can correlate the frequency shifts to the addition of holes to the molecules.

In addition to chemistry mediated by hot holes, Figure 6.3 shows that $Cu_{2-x}Se$ NPs can dimerize NBT to DMAB, which is a multi-electron reaction. Though these particles primarily produce hot holes, the electrons of the initial electron-hole pairs may be energetic enough to drive these reactions, even though they are not as energetic as hot

electrons produced on noble metals. Due to the successful NBT dimerization, $Cu_{2-x}Se$ NPs may be capable of catalyzing other plasmon-mediated processes, such as CO_2 reduction.

Beyond plasmon-mediated catalysis, $Cu_{2-x}Se$ NPs show promise as photothermal therapy agents,[161] which suggests that heating may play a larger role in plasmonic photocatalysis for these particles as compared to AuNPs. Due to the strong LSPR in the NIR, the plasmonic heating response may differ from that of similar gold nanoparticles. Measuring the localized heating of the adsorbates, similar to the experiments described in Chapter 4, would help to characterize these new materials and allow for a better comparison to more traditional materials.

Besides copper chalcogenides, there are various other non-noble metal materials that can support plasmons, like aluminum. Aluminum, similar to copper chalcogenides, is a cost-effective, earth-abundant alternative for plasmonic applications, with great promise as a highly selective plasmon photocatalyst. For example, aluminum nanocrystals (AlNCs), coupled with small amounts of catalytic metals,[179] like Pd, can efficiently drive industrial relevant reactions, like acetylene hydrogenation, with greater selectivity than traditional catalysts.[4] The suggested mechanism for this selectivity is that the plasmon of the AlNCs is excited with resonant light. The plasmon decays into hot carriers and the hot electrons transfer to the Pd catalysts. The presence of the electrons injected into the Pd modifies the reaction dynamics of the hydrogenation at the Pd reaction sites, leading to greater selectivity.

Using ultrafast SERS, we can further elucidate this mechanism for increased selectivity of AlNC-Pd nano-antenna reactors by monitoring the formation of intermediates and products upon plasmon excitation. The electromagnetic field enhancement of AlNCs is sufficient for SERS,[180] and based on theoretical predictions, the maximum field enhancement should occur near the interface between the Pd catalytic islands and the AlNC surface (Figure E4). In collaboration with the Halas group, we obtained AlNC-Pd nano-antenna reactors and prepared samples for ultrafast SERS measurements by dropcasting the particles onto a glass slide with an analyte. Initial studies were hampered by lack of analyte binding to the surface of the particles, most likely due to the presence of a self-terminating amorphous alumina layer on the AlNCs.[157] Preliminary studies for ultrafast SERS on AlNC-Pd nano-antenna reactors focused on obtaining measurable SERS signal in the NIR and monitoring for any plasmon-induced transient effects that may be probed by an adsorbed analyte. Figure 7.2a shows ultrafast SER difference spectra for catechol adsorbed to AlNC-Pd after excitation at 518 nm in various shades of red. Three catechol peaks appear in the pump-off spectrum (black). The difference spectra in Figure 7.2a can be described as 'ultraflat', where there are no transient dynamics in the form of peak growths or depletions at any time points. There may be some depletion arising around time zero, however due to the signal-to-noise we are unable to extract any additional information.

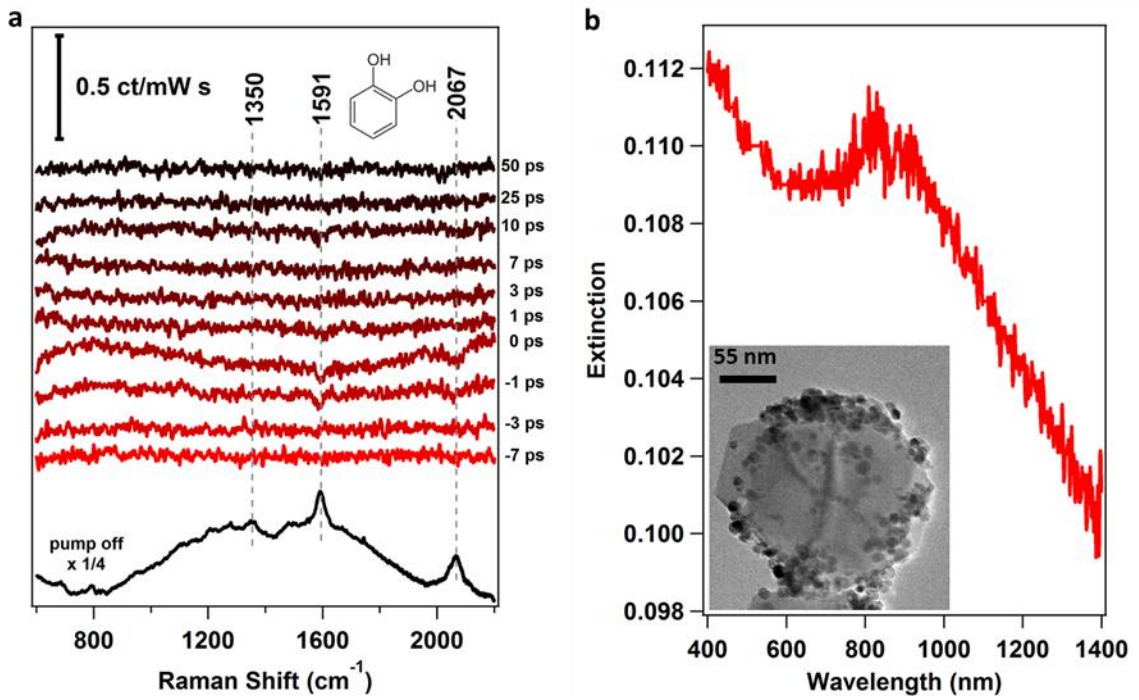

Figure 7.2 Catechol adsorbed to AlNC-Pd nano-antenna reactors monitored with ultrafast SERS and UV-Vis spectroscopy. (a) ultrafast surface-enhanced Raman difference spectra show minimal response upon photoexcitation with 518 nm. (b) Extinction spectrum of AlNC-Pd nano-reactors with catechol has decreasing LSPR magnitude in the NIR. The inset is a transmission electron micrograph of the AlNC-Pd nano-antenna reactors.

Although initial ultrafast SERS studies of AlNC-Pd nano-antenna reactors were not fully successful, future studies are still possible with the following modifications. One issue with the measurement described in Figure 7.2a is the coupling of the SERS probe pulse with the LSPR of the AlNCs. Primarily, the LSPR of AlNCs appears in the visible region of the electromagnetic spectrum. Figure 7.2b is an extinction spectrum of the sample used for the experiment in Figure 7.2a and the inset of Figure 7.2b is a transmission electron micrograph of the AlNC-Pd nano-antenna reactors. As can be seen in Figure 7.2b, the LSPR magnitude begins to decay rapidly in the NIR, which hinders SERS measurements at 1035 nm. With the modifications to the SERS instrument, as

described in 7.1, the ability to successfully probe this system significantly increases. Additionally, the nano-antenna reactors are being continuously improved for plasmonic applications by the Halas group.[179,181] Further modifications include changing the structure of the amorphous alumina layer to γ-alumina through an annealing process, as well as changing the synthetic procedure to make the AlNCs more hydrophilic. These modifications will allow for further characterization of these materials using ultrafast SERS as well as increasing their applicability to plasmonic photocatalytic processes.

In conclusion, I have shown that ultrafast SERS is a useful technique for advancing the understanding of the mechanism for plasmon-mediated photochemistry. Ultrafast SERS can measure the partitioning of energy into both hot carriers and into localized heating, and the impacts of these energy pathways on plasmonic photocatalysis. Additionally, ultrafast SERS can be used as a tool to quantify various plasmonic responses, from localized heating to plasmon-driven chemistry, on a variety of materials and in various local environments. This information is vital for the further development of more efficient and selective plasmonic photocatalysts and their integration into industrial relevant processes.

References

(1) Atwater, H. A.; Polman, A. Plasmonics for Improved Photovoltaic Devices. *Nat. Mater.* **2010**, *9* (10), 865–865.

(2) Huang, X.; Jain, P. K.; El-Sayed, I. H.; El-Sayed, M. A. Plasmonic Photothermal Therapy (PPTT) Using Gold Nanoparticles. *Lasers Med. Sci.* **2008**, *23* (3), 217–228.

(3) Neumann, O.; Urban, A. S.; Day, J.; Lal, S.; Nordlander, P. Solar Vapor Generation Enabled by Nanoparticles. *ACS Nano* **2012**, *7* (1), 42–49.

(4) Swearer, D. F.; Zhao, H.; Zhou, L.; Zhang, C.; Robatjazi, H.; Mark, J.; Martirez, P. Heterometallic Antenna − Reactor Complexes for Photocatalysis. *Proc. Natl. Acad. Sci. U. S. A.* **2016**, *113* (32), 8916–8920.

(5) Zhang, Y.; He, S.; Guo, W.; Hu, Y.; Huang, J.; Mulcahy, J. R.; Wei, W. D. Surface-Plasmon-Driven Hot Electron Photochemistry. *Chem. Rev.* **2018**, *118* (6), 2927–2954.

(6) Hartland, G. V; Besteiro, L. V; Johns, P.; Govorov, A. O. What's so Hot about Electrons in Metal Nanoparticles? *ACS Energy Lett.* **2017**, *2* (7), 1641–1653.

(7) Aruda, K. O.; Tagliazucchi, M.; Sweeney, C. M.; Hannah, D. C.; Weiss, E. A. The Role of Interfacial Charge Transfer-Type Interactions in the Decay of Plasmon Excitations in Metal Nanoparticles. *Phys. Chem. Chem. Phys.* **2013**, *15* (20), 7441–7449.

(8) Boerigter, C.; Aslam, U.; Linic, S. Mechanism of Charge Transfer from Plasmonic Nanostructures to Chemically Attached Materials. *ACS Nano* **2016**, *10* (6), 6108–6115.

(9) Hartland, G. V. Optical Studies of Dynamics in Noble Metal Nanostructures. *Chem. Rev.* **2011**, *111* (6), 3858–3887.

(10) Manjavacas, A.; Nordlander, P.; Kulkarni, V.; Liu, J. G. Plasmon-Induced Hot Carriers in Metallic Nanoparticles. *ACS Nano* **2014**, *8* (8), 7630–7638.

(11) Brandt, N. C.; Keller, E. L.; Frontiera, R. R. Ultrafast Surface-Enhanced Raman Probing of the Role of Hot Electrons in Plasmon-Driven Chemistry. *J. Phys. Chem. Lett.* **2016**, *7* (16), 3179–3185.

(12) Keller, E. L.; Frontiera, R. R. Monitoring Charge Density Delocalization upon Plasmon Excitation with Ultrafast Surface-Enhanced Raman Spectroscopy. *ACS Photonics* **2017**, *4* (5), 1033–1039.

(13) Kleinman, S. L.; Frontiera, R. R.; Henry, A.-I.; Dieringer, J. A.; Van Duyne, R. P. Creating, Characterizing, and Controlling Chemistry with SERS Hot Spots. *Phys. Chem. Chem. Phys.* **2013**, *15* (1), 21–36.

(14) Jeanmaire, D. L.; Van Duyne, R. P. Surface Raman Spectroelectrochemistry. *J. Electroanal. Chem.* **1977**, *84* (1), 1–20.

(15) Albrecht, M. G.; Creighton, J. A. Anomalously Intense Raman Spectra of Pyridine at a Silver Electrode. *J. Am. Chem. Soc.* **1977**, *99* (15), 5215–5217.

(16) Le Ru, E. C.; Meyer, M.; Etchegoin, P. G. Proof of Single-Molecule Sensitivity in Surface Enhanced Raman Scattering (SERS) by Means of a Two-Analyte Technique. *J. Phys. Chem. B* **2006**, *110* (4), 1944–1948.

(17) Moskovits, M. Surface-Enhanced Raman Spectroscopy: A Brief Retrospective. *J. Raman Spectrosc.* **2005**, *36* (6–7), 485–496.

(18) Ausman, L. K.; Li, S.; Schatz, G. C. Structural Effects in the Electromagnetic Enhancement Mechanism of Surface-Enhanced Raman Scattering: Dipole Reradiation and Rectangular Symmetry Effects for Nanoparticle Arrays. *J. Phys. Chem. C* **2012**, *116* (33), 17318–17327.

(19) Ko, H.; Singamaneni, S.; Tsukruk, V. V. Nanostructured Surfaces and Assemblies as SERS Media. *Small* **2008**, *4* (10), 1576–1599.

(20) Hoppmann, E. P.; Yu, W. W.; White, I. M. Highly Sensitive and Flexible Inkjet Printed SERS Sensors on Paper. *Methods* **2013**, *63* (3), 219–224.

(21) Thomann, I.; Pinaud, B. A.; Chen, Z.; Clemens, B. M.; Jaramillo, T. F.; Brongersma, M. L. Plasmon Enhanced Solar-to-Fuel Energy Conversion. *Nano Lett.* **2011**, *11* (8), 3440–3446.

(22) Hou, W.; Cronin, S. B. A Review of Surface Plasmon Resonance-Enhanced Photocatalysis. *Adv. Funct. Mater.* **2013**, *23* (13), 1612–1619.

(23) Hou, W.; Pavaskar, P.; Liu, Z.; Theiss, J.; Aykol, M.; Cronin, S. B. Plasmon Resonant Enhancement of Dye Sensitized Solar Cells. *Energy Environ. Sci.* **2011**, *4* (11), 4650–4655.

(24) Mubeen, S.; Lee, J.; Lee, W. R.; Singh, N.; Stucky, G. D.; Moskovits, M. On the Plasmonic Photovoltaic. *ACS Nano* **2014**, *8* (6), 6066–6073.

(25) Liu, Z.; Hou, W.; Pavaskar, P.; Aykol, M.; Cronin, S. B. Plasmon Resonant Enhancement of Photocatalytic Water Splitting under Visible Illumination. *Nano Lett.* **2011**, *11* (3), 1111–1116.

(26) Mubeen, S.; Lee, J.; Singh, N.; Krämer, S.; Stucky, G. D.; Moskovits, M. An Autonomous Photosynthetic Device in Which All Charge Carriers Derive from Surface Plasmons. *Nat. Nanotechnol.* **2013**, *8* (4), 247–251.

(27) Hou, W.; Liu, Z.; Pavaskar, P.; Hung, W. H.; Cronin, S. B. Plasmonic Enhancement of Photocatalytic Decomposition of Methyl Orange under Visible

Light. *J. Catal.* **2011**, *277* (2), 149–153.

(28) Zhou, X.; Hu, C.; Hu, X.; Peng, T.; Qu, J. Plasmon-Assisted Degradation of Toxic Pollutants with Ag− AgBr/Al_2O_3 under Visible-Light Irradiation. *J. Phys. Chem. C* **2010**, *114* (6), 2746–2750.

(29) Heritage, J. P.; Bergman, J. G.; Pinczuk, A.; Worlock, J. M. Surface Picosecond Raman Gain Spectroscopy of a Cyanide Monolayer on Silver. *Chem. Phys. Lett.* **1979**, *67* (2), 229–232.

(30) Kozich, V.; Werncke, W. The Vibrational Pumping Mechanism in Surface-Enhanced Raman Scattering: A Subpicosecond Time-Resolved Study. *J. Phys. Chem. C* **2010**, *114* (23), 10484–10488.

(31) Ichimura, T.; Hayazawa, N.; Hashimoto, M.; Inouye, Y.; Kawata, S. Tip-Enhanced Coherent Anti-Stokes Raman Scattering for Vibrational Nanoimaging. *Phys. Rev. Lett.* **2004**, *92* (22), 20–23.

(32) Galloway, C. M.; Etchegoin, P. G.; Le Ru, E. C. Ultrafast Nonradiative Decay Rates on Metallic Surfaces by Comparing Surface-Enhanced Raman and Fluorescence Signals of Single Molecules. *Phys. Rev. Lett.* **2009**, *103* (6), 1–4.

(33) Shibamoto, K.; Katayama, K.; Sawada, T. Ultrafast Charge Transfer in Surface-Enhanced Raman Scattering (SERS) Processes Using Transient Reflecting Grating (TRG) Spectroscopy. *Chem. Phys. Lett.* **2007**, *433* (4–6), 385–389.

(34) Stiles, P. L.; Dieringer, J. A.; Shah, N. C.; Van Duyne, R. P. Surface-Enhanced Raman Spectroscopy. *Annu. Rev. Anal. Chem.* **2008**, *1* (1), 601–626.

(35) Campion, A.; Kambhampati, P. Surface-Enhanced Raman Scattering. *Chem. Soc. Rev.* **1998**, *27* (4), 241–250.

(36) Kelly, K. L.; Coronado, E.; Zhao, L. L.; Schatz, G. C. The Optical Properties of Metal Nanoparticles: The Influence of Size, Shape, and Dielectric Environment. *J. Phys. Chem. B* **2003**, *107* (3), 668–677.

(37) Le Ru, E. C.; Etchegoin, P. G. *Principles of Surface-Enhanced Raman Spectroscopy and Related Plasmonic Effects*; Elsevier: Amsterdam, 2009.

(38) Hao, E.; Schatz, G. C. Electromagnetic Fields around Silver Nanoparticles and Dimers. *J. Chem. Phys.* **2004**, *120* (1), 357–366.

(39) Le Ru, E. C.; Etchegoin, P. G. Single-Molecule Surface-Enhanced Raman Spectroscopy. *Annu. Rev. Phys. Chem.* **2012**, *63* (1), 65–87.

(40) Nordlander, P.; Prodan, E. Plasmon Hybridization in Nanoparticles near Metallic Surfaces. *Nano Lett.* **2004**, *4* (11), 2209–2213.

(41) Jain, P. K.; El-Sayed, M. A. Plasmonic Coupling in Noble Metal Nanostructures. *Chem. Phys. Lett.* **2010**, *487* (4–6), 153–164.

(42) Zhu, W.; Crozier, K. B. Quantum Mechanical Limit to Plasmonic Enhancement as Observed by Surface-Enhanced Raman Scattering. *Nat. Commun.* **2014**, *5* (5228), 1–8.

(43) Brus, L. Noble Metal Nanoparticles: Plasmon Electron Transfer Photochemistry and Single-Molecule Raman Spectroscopy. *Acc. Chem. Res.* **2008**, *41* (12), 1742–1749.

(44) Brongersma, M. L.; Halas, N. J.; Nordlander, P. Plasmon-Induced Hot Carrier Science and Technology. *Nat. Nanotechnol.* **2015**, *10* (1), 25–34.

(45) Link, S.; El-Sayed, M. A. Size and Temperature Dependence of the Plasmon Absorption of Colloidal Gold Nanoparticles. *J. Phys. Chem. B* **1999**, *103* (21), 4212–4217.

(46) Sönnichsen, C.; Franzl, T.; Wilk, T.; von Plessen, G.; Feldmann, J.; Wilson, O.; Mulvaney, P. Drastic Reduction of Plasmon Damping in Gold Nanorods. *Phys. Rev. Lett.* **2002**, *88* (7), 774021–774024.

(47) Frischorn, C.; Wolf, M. Femtochemistry at Metal Surfaces: Nonadiabatic Reaction Dynamics. *Chem. Rev.* **2006**, *106* (10), 4207–4233.

(48) Sundararaman, R.; Narang, P.; Jermyn, A. S.; Goddard, W. A.; Atwater, H. A. Theoretical Predictions for Hot-Carrier Generation from Surface Plasmon Decay. *Nat. Commun.* **2014**, *5* (5788), 1–8.

(49) Ahmadi, T. S.; Logunov, S. L.; El-Sayed, M. A. Picosecond Dynamics of Colloidal Gold Nanoparticles. *J. Phys. Chem.* **1996**, *100* (20), 8053–8056.

(50) Hodak, J. H.; Henglein, A.; Hartland, G. V. Photophysics of Nanometer Sized Metal Particles: Electron-Phonon Coupling and Coherent Excitation of Breathing Vibrational Modes. *J. Phys. Chem. B* **2000**, *104* (43), 9954–9965.

(51) Aruda, K. O.; Tagliazucchi, M.; Sweeney, C. M.; Hannah, D. C.; Schatz, G. C.; Weiss, E. A. Identification of Parameters through Which Surface Chemistry Determines the Lifetimes of Hot Electrons in Small Au Nanoparticles. *Proc. Natl. Acad. Sci. U. S. A.* **2013**, *110* (11), 1–6.

(52) Hartland, G. Measurements of the Material Properties of Metal Nanoparticles by Time-Resolved Spectroscopy. *Phys. Chem. Chem. Phys.* **2004**, *6* (23), 5263–5274.

(53) Liu, M.; Lee, T. W.; Gray, S. K.; Guyot-Sionnest, P.; Pelton, M. Excitation of Dark Plasmons in Metal Nanoparticles by a Localized Emitter. *Phys. Rev. Lett.* **2009**, *102* (10), 1–4.

(54) Gomez, D. E.; Teo, Z. Q.; Altissimo, M.; Davis, T. J.; Earl, S.; Roberts, A. The Dark Side of Plasmonics. *Nano Lett.* **2013**, *13* (8), 3722–3728.

(55) Nordlander, P. Plasmonics: The Dark Side of the Ring. *Nat. Nanotechnol.* **2013**, *8* (2), 76–77.

(56) Herzog, J. B.; Knight, M. W.; Li, Y.; Evans, K. M.; Halas, N. J.; Natelson, D. Dark Plasmons in Hot Spot Generation and Polarization in Interelectrode Nanoscale Junctions. *Nano Lett.* **2013**, *13* (3), 1359–1364.

(57) Kleinman, S. L.; Sharma, B.; Blaber, M. G.; Henry, A. I.; Valley, N.; Freeman, R. G.; Natan, M. J.; Schatz, G. C.; Van Duyne, R. P. Structure Enhancement Factor Relationships in Single Gold Nanoantennas by Surface-Enhanced Raman Excitation Spectroscopy. *J. Am. Chem. Soc.* **2013**, *135* (1), 301–308.

(58) Frontiera, R. R.; Mathies, R. A. Femtosecond Stimulated Raman Spectroscopy. *Laser Photonics Rev.* **2011**, *5* (1), 102–113.

(59) Kukura, P.; McCamant, D. W.; Mathies, R. A. Femtosecond Stimulated Raman Spectroscopy. *Annu. Rev. Phys. Chem.* **2007**, *58* (1), 461–488.

(60) Cheng, J.; Xie, X. S. Coherent Anti-Stokes Raman Scattering Microscopy: Instrumentation, Theory, and Applications. *J. Phys. Chem. B* **2004**, *108* (1), 827–840.

(61) Oron, D.; Dudovich, N.; Silberberg, Y. Femtosecond Phase-and-Polarization Control for Background-Free Coherent Anti-Stokes Raman Spectroscopy. *Phys. Rev. Lett.* **2003**, *90* (21), 4.

(62) Ploetz, E. C.; Gellner, M.; Schütz, M.; Marx, B.; Schlücker, S.; Gilch, P. Surface Enhancement in Femtosecond Stimulated Raman Scattering. In *International Conference of Raman Spectroscopy XXII*; 2010; Vol. 1267, pp 88–89.

(63) Frontiera, R. R.; Henry, A. I.; Gruenke, N. L.; Van Duyne, R. P. Surface-Enhanced Femtosecond Stimulated Raman Spectroscopy. *J. Phys. Chem. Lett.* **2011**, *2* (10), 1199–1203.

(64) Frontiera, R. R.; Gruenke, N. L.; Van Duyne, R. P. Fano-like Resonances Arising from Long-Lived Molecule-Plasmon Interactions in Colloidal Nanoantennas. *Nano Lett.* **2012**, *12* (11), 5989–5994.

(65) Wustholz, K. L.; Henry, A.; Mcmahon, J. M.; Freeman, R. G.; Valley, N.; Piotti, M. E.; Natan, M. J.; Cuyne, R. P. Van. Structure-Activity Relationships in Gold Nanoparticle Dimers and Trimers for Surface-Enhanced Raman Spectroscopy. *J. Am. Chem. Soc.* **2010**, *132* (17), 10903–10910.

(66) Liang, E. J.; Weippert, A.; Funk, J.; Materny, A.; Kiefer, W. Experimental

Observation of Surface-Enhanced Coherent Anti-Stokes Raman Scattering. *Chem. Phys. Lett.* **1994**, *227* (1–2), 115–120.

(67) Ichimura, T.; Hayazawa, N.; Hashimoto, M.; Inouye, Y.; Kawata, S. Local Enhancement of Coherent Anti-Stokes Raman Scattering by Isolated Gold Nanoparticles. *J. Raman Spectrosc.* **2003**, *34* (9), 651–654.

(68) Zhang, Y.; Zhen, Y.; Neumann, O.; Day, J. K.; Nordlander, P.; Halas, N. J. Coherent Anti-Stokes Raman Scattering with Single-Molecule Sensitivity Using a Plasmonic Fano Resonance. *Nat. Commun.* **2014**, *5* (4424), 1–7.

(69) Yampolsky, S.; Fishman, D. A.; Dey, S.; Hulkko, E.; Banik, M.; Potma, E. O.; Apkarian, V. A. Seeing a Single Molecule Vibrate through Time-Resolved Coherent Anti-Stokes Raman Scattering. *Nat. Photonics* **2014**, *8* (8), 650–656.

(70) Piatkowski, L.; Hugall, J. T.; Van Hulst, N. F. Raman Spectroscopy: Watching a Molecule Breathe. *Nat. Photonics* **2014**, *8* (8), 589–591.

(71) Mukherjee, S.; Libisch, F.; Large, N.; Neumann, O.; Brown, L. V; Cheng, J.; Lassiter, J. B.; Carter, E. A.; Nordlander, P.; Halas, N. J. Hot Electrons Do the Impossible: Plasmon-Induced Dissociation of H_2 on Au. *Nano Lett.* **2012**, *13* (1), 240–247.

(72) Mukherjee, S.; Zhou, L.; Goodman, A. M.; Large, N.; Ayala-Orozco, C.; Zhang, Y.; Nordlander, P.; Halas, N. J. Hot-Electron-Induced Dissociation of H_2 on Gold Nanoparticles Supported on SiO_2. *J. Am. Chem. Soc.* **2014**, *136* (1), 64–67.

(73) Neumann, O.; Feronti, C.; Neumann, A. D.; Dong, A.; Schell, K.; Lu, B.; Kim, E.; Quinn, M.; Thompson, S.; Grady, N.; et al. Compact Solar Autoclave Based on Steam Generation Using Broadband Light-Harvesting Nanoparticles. *Proc. Natl. Acad. Sci.* **2013**, *110* (29), 11677–11681.

(74) Hogan, N. J.; Urban, A. S.; Ayala-Orozco, C.; Pimpinelli, A.; Nordlander, P.; Halas, N. J. Nanoparticles Heat through Light Localization. *Nano Lett.* **2014**, *14* (8), 4640–4645.

(75) Baral, S.; Green, A. J.; Livshits, M. Y.; Govorov, A. O.; Richardson, H. H. Comparison of Vapor Formation of Water at the Solid/Water Interface to Colloidal Solutions Using Optically Excited Gold Nanostructures. *ACS Nano* **2014**, *8* (2), 1439–1448.

(76) Moskovits, M. The Case for Plasmon-Derived Hot Carrier Devices. *Nat. Nanotechnol.* **2015**, *10* (1), 6–8.

(77) Wu, J.-L.; Chen, F.-C.; Hsiao, Y.-S.; Chien, F.-C.; Chen, P.; Kuo, C.-H.; Huang, M. H.; Hsu, C.-S. Surface Plasmonic Effects of Metallic Nanoparticles on the Performance of Polymer Bulk Heterojunction. *ACS Nano* **2011**, *5* (2), 959–967.

(78) Jain, P. K.; Huang, X.; El-Sayed, I. H.; El-Sayed, M. A. Noble Metals on the Nanoscale: Optical and Photothermal Properties and Some Applications in Imaging, Sensing, Biology, and Medicine. *Acc. Chem. Res.* **2008**, *14* (12), 1578–1586.

(79) Link, S.; El-Sayed, M. A. Shape and Size Dependence of Radiative, Non-Radiative and Photothermal Properties of Gold Nanocrystals. *Int. Rev. Phys. Chem.* **2000**, *19* (3), 409–453.

(80) Keller, E. L.; Brandt, N. C.; Cassabaum, A. A.; Frontiera, R. R. Ultrafast Surface-Enhanced Raman Spectroscopy. *Analyst* **2015**, *140* (15), 4922–4931.

(81) Feldstein, M. J.; Keating, C. D.; Liau, Y. H.; Natan, M. J.; Scherer, N. F. Electronic Relaxation Dynamics in Coupled Metal Nanoparticles. *J. Am. Chem. Soc.* **1997**, *119* (28), 6638–6647.

(82) Muskens, O. L.; Del Fatti, N.; Vallée, F. Femtosecond Response of a Single Metal Nanoparticle. *Nano Lett.* **2006**, *6* (3), 552–556.

(83) Jain, P. K.; Qian, W.; El-Sayed, M. A. Ultrafast Electron Relaxation Dynamics in Coupled Metal Nanoparticles in Aggregates. *J. Phys. Chem. B* **2006**, *110* (1), 136–142.

(84) Frens, G. Controlled Nucleation for the Regulation of the Particle Size in Monodisperse Gold Suspensions. *Nat. Phys. Sci.* **1973**, *241*, 20–22.

(85) van Schrojenstein Lantman, E. M.; Deckert-Gaudig, T.; Mank, A. J. G.; Deckert, V.; Weckhuysen, B. M. Catalytic Processes Monitored at the Nanoscale with Tip-Enhanced Raman Spectroscopy. *Nat. Nanotechnol.* **2012**, *7* (9), 583–586.

(86) Sun, M.; Xu, H. A Novel Application of Plasmonics: Plasmon-Driven Surface-Catalyzed Reactions. *Small* **2012**, *8* (18), 2777–2786.

(87) Futamata, M. Surface-Plasmon-Polariton-Enhanced Raman Scattering from Self-Assembled Monolayers of p-Nitrothiophenol and p-Aminothiophenol on Silver. *J.Phys.Chem.* **1995**, *99* (31), 11901–11908.

(88) Valley, N.; Greeneltch, N.; Van Duyne, R. P.; Schatz, G. C. A Look at the Origin and Magnitude of the Chemical Contribution to the Enhancement Mechanism of Surface-Enhanced Raman Spectroscopy (SERS): Theory and Experiment. *J. Phys. Chem. Lett.* **2013**, *4* (16), 2599–2604.

(89) Willets, K. A.; Van Duyne, R. P. Localized Surface Plasmon Resonance Spectroscopy and Sensing. *Annu. Rev. Phys. Chem.* **2007**, *58* (1), 267–297.

(90) Hodak, J. H.; Martini, I.; Hartland, G. V. Spectroscopy and Dynamics of Nanometer-Sized Noble Metal Particles. *J. Phys. Chem. B* **1998**, *102* (36), 6958–

6967.

(91) Hodak, J.; Martini, I.; Hartland, G. V. Ultrafast Study of Electron–Phonon Coupling in Colloidal Gold Particles. *Chem. Phys. Lett.* **1998**, *284* (1–2), 135–141.

(92) Link, S.; Burda, C.; Mohamed, M.; Nikoobakht, B.; El-Sayed, M. A. Femtosecond Transient-Absorption Dynamics of Colloidal Gold Nanorods: Shape Independence of the Electron-Phonon Relaxation Time. *Phys. Rev. B* **2000**, *61* (9), 6086–6090.

(93) Del Fatti, N.; Vallée, F.; Flytzanis, C.; Hamanaka, Y.; Nakamura, A. Electron Dynamics and Surface Plasmon Resonance Nonlinearities in Metal Nanoparticles. *Chem. Phys.* **2000**, *251* (1–3), 215–226.

(94) Weisstein, E. W. Sphere Packing http://mathworld.wolfram.com/SpherePacking.html (accessed Dec 16, 2016).

(95) Voisin, C.; Christofilos, D.; Loukakos, P. A.; Del Fatti, N.; Vallée, F.; Lermé, J.; Gaudry, M.; Cottancin, E.; Pellarin, M.; Broyer, M. Ultrafast Electron-Electron Scattering and Energy Exchanges in Noble-Metal Nanoparticles. *Phys. Rev. B* **2004**, *69* (19), 1–13.

(96) Collins, S. S. E.; Wei, X.; McKenzie, T. G.; Funston, A. M.; Mulvaney, P. Single Gold Nanorod Charge Modulation in an Ion Gel Device. *Nano Lett.* **2016**, *16* (11), 6863–6869.

(97) Brown, A. M.; Sheldon, M. T.; Atwater, H. A. Electrochemical Tuning of the Dielectric Function of Au Nanoparticles. *ACS Photonics* **2015**, *2* (4), 459–464.

(98) Mulvaney, P.; Pérez-Juste, J.; Giersig, M.; Liz-Marzán, L. M.; Pecharromán, C. Drastic Surface Plasmon Mode Shifts in Gold Nanorods Due to Electron Charging. *Plasmonics* **2006**, *1* (1), 61–66.

(99) Ung, T.; Giersig, M.; Dunstan, D.; Mulvaney, P. Spectroelectrochemistry of Colloidal Silver. *Langmuir* **1997**, *13* (6), 1773–1782.

(100) Pelton, M.; Liu, M.; Park, S.; Scherer, N. F.; Guyot-Sionnest, P. Ultrafast Resonant Optical Scattering from Single Gold Nanorods: Large Nonlinearities and Plasmon Saturation. *Phys. Rev. B* **2006**, *73* (15), 1–6.

(101) McFarland, A. D.; Young, M. A.; Dieringer, J. A.; Van Duyne, R. P. Wavelength-Scanned Surface-Enhanced Resonance Raman Excitation Spectroscopy. *J. Phys. Chem. B* **2005**, *109* (22), 11279–11285.

(102) Fang, Y.; Seong, N.-H.; Dlott, D. D. Measurement of the Distribution of Site Enhancements in Surface-Enhanced Raman Scattering. *Science* **2008**, *321* (5887), 388–393.

(103) Robatjazi, H.; Zhao, H.; Swearer, D. F.; Hogan, N. J.; Zhou, L.; Alabastri, A.;

McClain, M. J.; Nordlander, P.; Halas, N. J. Plasmon-Induced Selective Carbon Dioxide Conversion on Earth-Abundant Aluminum-Cuprous Oxide Antenna-Reactor Nanoparticles. *Nat. Commun.* **2017**, *8* (27), 1–10.

(104) Porosoff, M. D.; Yan, B.; Chen, J. G. Catalytic Reduction of CO_2 by H_2 for Synthesis of CO, Methanol and Hydrocarbons: Challenges and Opportunities. *Energy Environ. Sci.* **2016**, *9* (1), 62–73.

(105) Lee, J.; Mubeen, S.; Ji, X.; Stucky, G. D.; Moskovits, M. Plasmonic Photoanodes for Solar Water Splitting with Visible Light. *Nano Lett.* **2012**, *12* (9), 5014–5019.

(106) Khlebtsov, B.; Zharov, V.; Melnikov, A.; Tuchin, V.; Khlebtsov, N. G. Optical Amplification of Photothermal Therapy with Gold Nanoparticles and Nanoclusters. *Nanotechnol.* **2006**, *17* (20), 5167–5179.

(107) Somorjai, G. A.; Li, Y. *Introduction to Surface Chemistry and Catalysis*, 2nd ed.; John Wiley & Sons, Inc.: Hoboken, NJ, 2010.

(108) Wang, F.; Li, C.; Chen, H.; Jiang, R.; Sun, L. D.; Li, Q.; Wang, J.; Yu, J. C.; Yan, C. H. Plasmonic Harvesting of Light Energy for Suzuki Coupling Reactions. *J. Am. Chem. Soc.* **2013**, *135* (15), 5588–5601.

(109) Christopher, P.; Xin, H.; Linic, S. Visible-Light-Enhanced Catalytic Oxidation Reactions on Plasmonic Silver Nanostructures. *Nat. Chem.* **2011**, *3* (6), 467–472.

(110) Huschka, R.; Zuloaga, J.; Knight, M. W.; Brown, L. V.; Nordlander, P.; Halas, N. J. Light-Induced Release of DNA from Gold Nanoparticles: Nanoshells and Nanorods. *J. Am. Chem. Soc.* **2011**, *133* (31), 12247–12255.

(111) Khosravi Khorashad, L.; Besteiro, L. V.; Wang, Z.; Valentine, J.; Govorov, A. O. Localization of Excess Temperature Using Plasmonic Hot Spots in Metal Nanostructures: Combining Nano-Optical Antennas with the Fano Effect. *J. Phys. Chem. C* **2016**, *120* (24), 13215–13226.

(112) Chen, H.; Shao, L.; Ming, T.; Sun, Z.; Zhao, C.; Yang, B.; Wang, J. Understanding the Photothermal Conversion Efficiency of Gold Nanocrystals. *Small* **2010**, *6* (20), 2272–2280.

(113) Guler, U.; Ndukaife, J. C.; Naik, G. V.; Nnanna, A. G. A.; Kildishev, A. V.; Shalaev, V. M.; Boltasseva, A. Local Heating with Lithographically Fabricated Plasmonic Titanium Nitride Nanoparticles. *Nano Lett.* **2013**, *13* (12), 6078–6083.

(114) Baffou, G.; Quidant, R. Thermo-Plasmonics: Using Metallic Nanostructures as Nano-Sources of Heat. *Laser Photonics Rev.* **2013**, *7* (2), 171–187.

(115) Nachman, N.; Selzer, Y. Thermometry of Plasmonic Heating by Inelastic Electron Tunneling Spectroscopy (IETS). *Nano Lett.* **2017**, *17* (9), 5855–5861.

(116) Kip, B. J.; Meier, R. J. Determination of the Local Temperature at a Sample during Raman Experiments Using Stokes and Anti-Stokes Raman Bands. *Appl. Spectrosc.* **1990**, *44* (4), 707–711.

(117) Maher, R. C.; Cohen, L. F.; Gallop, J. C.; Le Ru, E. C.; Etchegoin, P. G. Temperature-Dependent Anti-Stokes/Stokes Ratios under Surface-Enhanced Raman Scattering Conditions. *J. Phys. Chem. B* **2006**, *110* (13), 6797–6803.

(118) Pozzi, E. A.; Zrimsek, A. B.; Lethiec, C. M.; Schatz, G. C.; Hersam, M. C.; Van Duyne, R. P. Evaluating Single-Molecule Stokes and Anti-Stokes SERS for Nanoscale Thermometry. *J. Phys. Chem. C* **2015**, *119* (36), 21116–21124.

(119) Frontiera, R. R.; Fang, C.; Dasgupta, J.; Mathies, R. A. Probing Structural Evolution along Multidimensional Reaction Coordinates with Femtosecond Stimulated Raman Spectroscopy. *Phys. Chem. Chem. Phys.* **2012**, *14* (2), 405–414.

(120) Crim, F. F. Chemical Dynamics of Vibrationally Excited Molecules: Controlling Reactions in Gases and on Surfaces. *Proc. Natl. Acad. Sci. U. S. A.* **2008**, *105* (35), 12654–12661.

(121) Fujimori, H.; Kakihana, M.; Ioku, K.; Goto, S.; Yoshimura, M. Advantage of Anti-Stokes Raman Scattering for High-Temperature Measurements. *Appl. Phys. Lett.* **2001**, *79* (7), 937–939.

(122) Ornstein, L. S.; Rekveld, J. Intensity Measurements in the Raman Effect and the Distribution Law of Maxwell-Boltzmann. *Phys. Rev.* **1929**, *34* (5), 720–725.

(123) Ferrante, C.; Virga, A.; Benfatto, L.; Martinati, M.; De Fazio, D.; Sassi, U.; Fasolato, C.; Ott, A. K.; Postorino, P.; Yoon, D.; et al. Raman Spectroscopy of Graphene under Ultrafast Laser Excitation. *Nat. Commun.* **2018**, *9* (308), 1–8.

(124) Boerigter, C.; Campana, R.; Morabito, M.; Linic, S. Evidence and Implications of Direct Charge Excitation as the Dominant Mechanism in Plasmon-Mediated Photocatalysis. *Nat. Commun.* **2016**, *7* (10545), 1–9.

(125) Brooks, J. L.; Frontiera, R. R. Competition between Reaction and Degradation Pathways in Plasmon-Driven Photochemistry. *J. Phys. Chem. C* **2016**, *120* (37), 20869–20876.

(126) Berg, C. M.; Sun, Y.; Dlott, D. D. Temperature-Dependent Dynamic Response to Flash Heating of Molecular Monolayers on Metal Surfaces: Vibrational Energy Exchange. *J. Phys. Chem. B* **2014**, *118* (28), 7770–7776.

(127) Pein, B. C.; Sun, Y.; Dlott, D. D. Unidirectional Vibrational Energy Flow in Nitrobenzene. *J. Phys. Chem. A* **2013**, *117* (29), 6066–6072.

(128) Dieringer, J. A.; McFarland, A. D.; Shah, N. C.; Stuart, D. A.; Whitney, A. V;

Yonzon, C. R.; Young, M. A.; Zhang, X.; Van Duyne, R. P. Surface Enhanced Raman Spectroscopy: New Materials, Concepts, Characterization Tools, and Applications. *Faraday Discuss.* **2006**, *132*, 9–26.

(129) White, R. J.; Luque, R.; Budarin, V. L.; Clark, J. H.; MacQuarrie, D. J. Supported Metal Nanoparticles on Porous Materials. Methods and Applications. *Chem. Soc. Rev.* **2009**, *38* (2), 481–494.

(130) Comotti, M.; Li, W.-C.; Spliethoff, B.; Schüth, F. Support Effect in High Activity Gold Catalysts for CO Oxidation. *J. Am. Chem. Soc.* **2006**, *128* (3), 917–924.

(131) Sarina, S.; Waclawik, E. R.; Zhu, H. Photocatalysis on Supported Gold and Silver Nanoparticles under Ultraviolet and Visible Light Irradiation. *Green Chem.* **2013**, *15* (7), 1814–1833.

(132) Kale, M. J.; Avanesian, T.; Christopher, P. Direct Photocatalysis by Plasmonic Nanostructures. *ACS Catal.* **2014**, *4* (1), 116–128.

(133) Primo, A.; Corma, A.; García, H. Titania Supported Gold Nanoparticles as Photocatalyst. *Phys. Chem. Chem. Phys.* **2011**, *13* (3), 886–910.

(134) Zhang, X.; Li, X.; Reish, M. E.; Zhang, D.; Su, N. Q.; Gutiérrez, Y.; Moreno, F.; Yang, W.; Everitt, H. O.; Liu, J. Plasmon-Enhanced Catalysis: Distinguishing Thermal and Nonthermal Effects. *Nano Lett.* **2018**, *18* (3), 1714–1723.

(135) Adleman, J. R.; Boyd, D. A.; Goodwin, D. G.; Psaltis, D. Heterogenous Catalysis Mediated by Plasmon Heating. *Nano Lett.* **2009**, *9* (12), 4417–4423.

(136) Keller, E. L.; Frontiera, R. R. Ultrafast Nanoscale Raman Thermometry Proves Heating Is Not a Primary Mechanism for Plasmon-Driven Photocatalysis. *ACS Nano* **2018**, *12* (6), 5848–5855.

(137) Davis, M. E. Ordered Porous Materials for Emerging Applications. *Nature* **2002**, *417*, 813–821.

(138) Gorelikov, I.; Matsuura, N. Single-Step Coating of Mesoporous Silica on Cetyltrimethyl Ammonium Bromide-Capped Nanoparticles. *Nano Lett.* **2008**, *8* (1), 369–373.

(139) Egger, S. M.; Hurley, K. R.; Datt, A.; Swindlehurst, G.; Haynes, C. L. Ultraporous Mesostructured Silica Nanoparticles. *Chem. Mater.* **2015**, *27* (9), 3193–3196.

(140) Yang, W. H.; Hulteen, J.; Schatz, G. C.; Van Duyne, R. P. A Surface-Enhanced Hyper-Raman and Surface-Enhanced Raman Scattering Study of Trans-1,2-Bis(4-Pyridyl)Ethylene Adsorbed onto Silver Film over Nanosphere Electrodes. Vibrational Assignments: Experiment and Theory. *J. Chem. Phys.* **1996**, *104* (11), 4313–4323.

(141) Wu, X.; Ni, Y.; Zhu, J.; Burrows, N. D.; Murphy, C. J.; Dumitrica, T.; Wang, X. Thermal Transport across Surfactant Layers on Gold Nanorods in Aqueous Solution. *ACS Appl. Mater. Interfaces* **2016**, *8* (16), 10581–10589.

(142) Huang, J.; Park, J.; Wang, W.; Murphy, C. J.; Cahill, D. G. Ultrafast Thermal Analysis of Surface Functionalized Gold Nanorods in Aqueous Solution. *ACS Nano* **2013**, *7* (1), 589–597.

(143) Coquil, T.; Richman, E. K.; Hutchinson, N. J.; Tolbert, S. H.; Pilon, L. Thermal Conductivity of Cubic and Hexagonal Mesoporous Silica Thin Films. *J. Appl. Phys.* **2009**, *106* (3).

(144) Li, J.; Feng, Y.; Zhang, X.; Huang, C.; Wang, G. Near-Field Radiative Heat Transfer across a Pore and Its Effects on Thermal Conductivity of Mesoporous Silica. *Phys. B Condens. Matter* **2015**, *456*, 237–243.

(145) Braun, J. L.; Baker, C. H.; Giri, A.; Elahi, M.; Artyushkova, K.; Beechem, T. E.; Norris, P. M.; Leseman, Z. C.; Gaskins, J. T.; Hopkins, P. E. Size Effects on the Thermal Conductivity of Amorphous Silicon Thin Films. *Phys. Rev. B* **2016**, *93* (14), 140201.

(146) Combis, P.; Cormont, P.; Gallais, L.; Hebert, D.; Robin, L.; Rullier, J. L. Evaluation of the Fused Silica Thermal Conductivity by Comparing Infrared Thermometry Measurements with Two-Dimensional Simulations. *Appl. Phys. Lett.* **2012**, *101* (21), 1–5.

(147) Marszewski, M.; Butts, D.; Lan, E.; Yan, Y.; King, S. C.; McNeil, P. E.; Galy, T.; Dunn, B.; Tolbert, S. H.; Hu, Y.; et al. Effect of Surface Hydroxyl Groups on Heat Capacity of Mesoporous Silica. *Appl. Phys. Lett.* **2018**, *112* (20), 201903.

(148) Ge, Z.; Kang, Y.; Taton, T. A.; Braun, P. V.; Cahill, D. G. Thermal Transport in Au-Core Polymer-Shell Nanoparticles. *Nano Lett.* **2005**, *5* (3), 531–535.

(149) Wilson, O. M.; Hu, X.; Cahill, D. G.; Braun, P. V. Colloidal Metal Particles as Probes of Nanoscale Thermal Transport in Fluids. *Phys. Rev. B - Condens. Matter Mater. Phys.* **2002**, *66* (22), 2243011–2243016.

(150) Cahill, D. G.; Braun, P. V.; Chen, G.; Clarke, D. R.; Fan, S.; Goodson, K. E.; Keblinski, P.; King, W. P.; Mahan, G. D.; Majumdar, A.; et al. Nanoscale Thermal Transport. II. 2003-2012. *Appl. Phys. Rev.* **2014**, *1* (1), 011305.

(151) Bippus, L.; Jaber, M.; Lebeau, B.; Schleich, D.; Scudeller, Y. Thermal Conductivity of Heat Treated Mesoporous Silica Particles. *Microporous Mesoporous Mater.* **2014**, *190*, 109–116.

(152) Nguyen, S. C.; Zhang, Q.; Manthiram, K.; Ye, X.; Lomont, J. P.; Harris, C. B.; Weller, H.; Alivisatos, A. P. Study of Heat Transfer Dynamics from Gold

Nanorods to the Environment via Time-Resolved Infrared Spectroscopy. *ACS Nano* **2016**, *10* (2), 2144–2151.

(153) Shim, S.; Mathies, R. A. Generation of Narrow-Bandwidth Picosecond Visible Pulses from Broadband Femtosecond Pulses for Femtosecond Stimulated Raman. *Appl. Phys. Lett.* **2006**, *89* (12), 121124.

(154) Zou, L.; Wang, H.; He, B.; Zeng, L.; Tan, T.; Cao, H.; He, X.; Zhang, Z.; Guo, S.; Li, Y. Current Approaches of Photothermal Therapy in Treating Cancer Metastasis with Nanotherapeutics. *Theranostics* **2016**, *6* (6), 762–772.

(155) Linic, S.; Aslam, U.; Boerigter, C.; Morabito, M. Photochemical Transformations on Plasmonic Metal Nanoparticles. *Nat. Mater.* **2015**, *14* (6), 567–576.

(156) Luther, J. M.; Jain, P. K.; Ewers, T.; Alivisatos, A. P. Localized Surface Plasmon Resonances Arising from Free Carriers in Doped Quantum Dots. *Nat. Mater.* **2011**, *10* (5), 361–366.

(157) Mcclain, M. J.; Schlather, A. E.; Ringe, E.; King, N. S.; Liu, L.; Manjavacas, A.; Knight, M. W.; Kumar, I.; Whitmire, K. H.; Everitt, H. O.; et al. Aluminum Nanocrystals. *Nano Lett.* **2015**, *15* (4), 2751–2755.

(158) Agrawal, A.; Johns, R. W.; Milliron, D. J. Control of Localized Surface Plasmon Resonances in Metal Oxide Nanocrystals. *Annu. Rev. Mater. Res.* **2017**, *47* (1), 1–31.

(159) Guler, U.; Shalaev, V. M.; Boltasseva, A. Nanoparticle Plasmonics : Going Practical with Transition Metal Nitrides. *Biochem. Pharmacol.* **2015**, *18* (4), 227–237.

(160) Kriegel, I.; Scotognella, F.; Manna, L. Plasmonic Doped Semiconductor Nanocrystals : Properties , Fabrication , Applications and Perspectives. *Phys. Rep.* **2017**, *674*, 1–52.

(161) Liu, X.; Swihart, M. T. Heavily-Doped Colloidal Semiconductor and Metal Oxide Nanocrystals : An Emerging New Class of Plasmonic Nanomaterials. *Chem. Soc. Rev.* **2014**, *43* (11), 3908–3920.

(162) Kim, J.; Agrawal, A.; Krieg, F.; Bergerud, A.; Milliron, D. J. The Interplay of Shape and Crystalline Anisotropies in Plasmonic Semiconductor Nanocrystals. *Nano Lett.* **2016**, *16* (6), 3879–3884.

(163) Balitskii, O. A.; Sytnyk, M.; Stangl, J.; Primetzhofer, D.; Groiss, H.; Heiss, W. Tuning the Localized Surface Plasmon Resonance in $Cu_{2-x}Se$ Nanocrystals by Postsynthetic Ligand Exchange. *ACS Appl. Mater. Interfaces* **2014**, *6* (20), 17770–17775.

(164) Crockett, B. M.; Jansons, A. W.; Koskela, K. M.; Johnson, D. W.; Hutchison, J. E. Radial Dopant Placement for Tuning Plasmonic Properties in Metal Oxide Nanocrystals. *ACS Nano* **2017**, *11* (8), 7719–7728.

(165) Marbella, L. E.; Gan, X. Y.; Kaseman, D. C.; Millstone, J. E. Correlating Carrier Density and Emergent Plasmonic Features in $Cu_{2-x}Se$ Nanoparticles. *Nano Lett.* **2017**, *17* (4), 2414–2419.

(166) Lounis, S. D.; Runnerstrom, E. L.; Bergerud, A.; Nordlund, D.; Milliron, D. J. Influence of Dopant Distribution on the Plasmonic Properties of Indium Tin Oxide Nanocrystals. *J. Am. Chem. Soc.* **2014**, *136* (19), 7110–7116.

(167) Li, W.; Zamani, R.; Ibanez, M.; Cadavid, D.; Shavel, A.; Morante, J. R.; Arbiol, J.; Cabot, A. Metal Ions To Control the Morphology of Semiconductor Nanoparticles: Copper Selenide Nanocubes. *J. Am. Chem. Soc.* **2013**, *135*, 4664–4667.

(168) Wu, K.; Chen, J.; McBride, J. R.; Lian, T. Efficient Hot-Electron Transfer by a Plasmon-Induced Interfacial Charge-Transfer Transition. *Science* **2015**, *349* (6248), 632–635.

(169) Griffin, S.; Montoni, N. P.; Li, G.; Straney, P. J.; Millstone, J. E.; Masiello, D. J.; Camden, J. P. Imaging Energy Transfer in Pt-Decorated Au Nanoprisms via Electron Energy-Loss Spectroscopy. *J. Phys. Chem. Lett.* **2016**, *7* (19), 3825–3832.

(170) Agrawal, A.; Cho, S. H.; Zandi, O.; Ghosh, S.; Johns, R. W.; Milliron, D. J. Localized Surface Plasmon Resonance in Semiconductor Nanocrystals. *Chem. Rev.* **2018**, *118* (6), 3121–3207.

(171) Stolarczyk, J. K.; Bhattacharyya, S.; Polavarapu, L.; Feldmann, J. Challenges and Prospects in Solar Water Splitting and CO_2 Reduction with Inorganic and Hybrid Nanostructures. *ACS Catal.* **2018**, 3602–3635.

(172) Cui, J.; Li, Y.; Liu, L.; Chen, L.; Xu, J.; Ma, J.; Fang, G.; Zhu, E.; Wu, H.; Zhao, L.; et al. Near-Infrared Plasmonic-Enhanced Solar Energy Harvest for Highly Efficient Photocatalytic Reactions. *Nano Lett.* **2015**, *15* (10), 6295–6301.

(173) Deka, S.; Genovese, A.; Zhang, Y.; Miszta, K.; Bertoni, G. Phosphine-Free Synthesis of p-Type Copper (I) Selenide Nanocrystals in Hot Coordinating Solvents. *J. Am. Chem. Soc.* **2010**, *132* (26), 8912–8914.

(174) Yu, Y.; Sundaresan, V.; Willets, K. A. Hot Carriers versus Thermal Effects: Resolving the Enhancement Mechanisms for Plasmon-Mediated Photoelectrochemical Reactions. *J. Phys. Chem. C* **2018**, *122* (9), 5040–5048.

(175) Yu, Y.; Williams, J. D.; Willets, K. A. Quantifying Photothermal Heating at Plasmonic Nanoparticles by Scanning Electrochemical Microscopy. *Faraday Discuss.* **2018**.

(176) Dang, N. C.; Bolme, C. A.; Moore, D. S.; McGrane, S. D. Femtosecond Stimulated Raman Scattering Picosecond Molecular Thermometry in Condensed Phases. *Phys. Rev. Lett.* **2011**, *107* (4), 1–4.

(177) Kim, S.; Kim, J. M.; Park, J. E.; Nam, J. M. Nonnoble-Metal-Based Plasmonic Nanomaterials: Recent Advances and Future Perspectives. *Adv. Mater.* **2018**, *1704528*, 1–24.

(178) Scotognella, F.; Valle, G. Della; Ram, A.; Kandada, S.; Dorfs, D.; Zavelani-rossi, M.; Conforti, M.; Miszta, K.; Comin, A.; Korobchevskaya, K.; et al. Plasmon Dynamics in Colloidal $Cu_{2-x}Se$ Nanocrystals. *Nano Lett.* **2011**, *11* (11), 4711–4717.

(179) Swearer, D. F.; Leary, R. K.; Newell, R.; Yazdi, S.; Robatjazi, H.; Zhang, Y.; Renard, D.; Nordlander, P.; Midgley, P. A.; Halas, N. J.; et al. Transition-Metal Decorated Aluminum Nanocrystals. *ACS Nano* **2017**, *11* (10), 10281–10288.

(180) Tian, S.; Neumann, O.; McClain, M. J.; Yang, X.; Zhou, L.; Zhang, C.; Nordlander, P.; Halas, N. J. Aluminum Nanocrystals: A Sustainable Substrate for Quantitative SERS-Based DNA Detection. *Nano Lett.* **2017**, *17* (8), 5071–5077.

(181) Clark, B. D.; Jacobson, C. R.; Lou, M.; Yang, J.; Zhou, L.; Gottheim, S.; DeSantis, C. J.; Nordlander, P.; Halas, N. J. Aluminum Nanorods. *Nano Lett.* **2018**, *18* (2), 1234–1240.

Appendix A

Supporting Information for Manuscript:

Monitoring Charge Density Delocalization upon Plasmon Excitation with Ultrafast Surface-Enhanced Raman Spectroscopy

A.1 Methods

A.1.1 Sample Preparation

Gold (III) chloride trihydrate, sodium citrate, and 4-nitrobenzenethiol (4-NBT) for sample preparation were obtained from Sigma-Aldrich and used without further purification. To synthesize colloidal gold nanoparticles (AuNPs), 4.1 mg of gold (III) chloride trihyrdrate dissolved in 41 mL of DI H_2O was combined with 0.172 mL 1% by weight aqueous sodium citrate dihydrate under heat and stirring.[1] The as-synthesized particles were centrifuged at 2600 g for 0.5 to 1 hour and concentrated by removing 2.94 mL of supernatant from 3 mL of sample. The particles were aggregated in a 1.7 mL microcentrifuge tube with 70 µL of a saturated 4-NBT aqueous solution, 105 µL to 150 µL of 0.100 M KNO_3 and 262 µL to 180 µL of DI H_2O. The concentration of the saturated 4-NBT solution was measured by UV-visible spectroscopy to be approximately 200 µM, well in excess of that required for the formation of a monolayer of 4-NBT on the AuNP substrates. The sample was transferred to a 2 mm pathlength quartz cuvette (Starna 21-Q-2) for all measurements. Samples were stirred throughout the course of the experiment to refresh the sample in the irradiated volume and to minimize precipitation of the aggregated particles.

A.1.2 Ultrafast SERS Instrumentation

Ultrafast SERS measurements were performed using the instrument described previously.[2] Some modifications were made to include a commercial NOPA (Clark-MXR iNOPA) as described below and depicted schematically in Figure A1. The instrument utilized a Yb-doped fiber-based amplified laser (Clark-MXR Impulse), which produced

<250 fs pulses centered at 1035 nm at 2 MHz repetition rate, with an average power of 20.5 W. To generate the picosecond probe pulse, 8 W of the incident beam entered a spectral filter constructed in a retroreflecting geometry[3], which contained a transmission grating (LightSmyth Technologies LSFSG-1000-3212-94) to disperse the beam and a 100 mm focal length cylindrical lens (Newport CKX100AR.16) to image the beam onto a slit. The spectral width of the filtered output was 12.6 cm^{-1}, as measured from the 801 cm^{-1} peak of cyclohexane. Pump wavelengths used for excitation were 700, 750, 800, and the fundamental wavelength of 1035 nm. For wavelengths other than 1035 nm, a commercial NOPA generated the pump beam from the Impulse output with a repetition rate of 2MHz at 16 W. The bandwidth of the NOPA output at 700 nm, 750 nm and 800 nm was 16 nm, 28 nm and 50 nm, respectively. Unwanted NIR wavelengths from the NOPA output were removed by placing two 950 nm shortpass filters (Thorlabs FESH0950 and FES0950) before the sample. A 100 mm focal length achromatic lens (Edmund Optics 49-374) focused the pump and probe beams onto the sample to a spot size of approximately 120 microns. The probe power was 24.5 mW and the pump power ranged from 10 to 150 mW. After the sample, a spatial filter blocked pump transmission, and a 60 mm focal length lens (Thorlabs, LA1134-C) collimated the spontaneous Raman signal. An additional longpass filter (Thorlabs FEL1100) was used to further reduce pump beam scatter. A 100 mm focal length achromatic lens (Thorlabs, AC254-100-C) focused the Raman signal into a 0.3 m spectrograph (Princeton Instruments SP2300i) equipped with a 600 gr/mm, 750 nm blaze grating. A 1064 nm Raman filter (Edmund Optics 47-510) directly before the spectrograph removed any remaining 1035 nm light from the Raman

signal. A 1024 pixel, liquid nitrogen cooled InGaAs photodiode array (Princeton Instruments PyLoN-IR 1.7) was used for detection of the Stokes-shifted spontaneous Raman scattering.

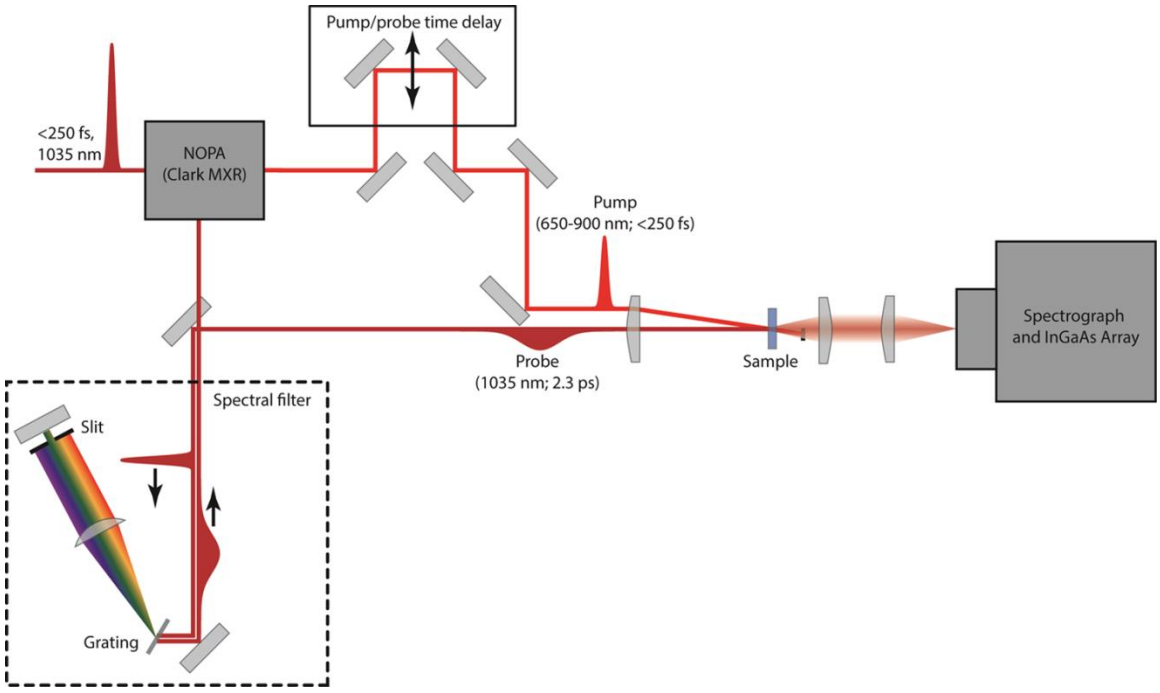

Figure A1. Schematic depiction of the ultrafast SERS instrument. Acronym used in the figure are non-colinear optical parametric amplifier (NOPA). Adapted with permission from ref. 2.

A.1.3 Data Collection and Processing

Each ultrafast SER spectrum consists of 3 averaged frames integrated for 20 seconds with the probe beam. For pump-probe measurements, a delay stage (Newport XMS50) in the pump path allows for data acquisition at various time points. The time resolution of the 24.5 MHz set-up is 3.6 ps, which is determined from an optical Kerr effect measurement in benzene and the time resolution of the 2 MHz set-up is 2.4 ps. Normally, a pump-off spectrum is taken followed immediately by a pump-on spectrum at each time point. After the spectra are averaged, the pump-off spectrum is subtracted from

the pump-on spectrum to see the effects of excitation at different time delays. However, there is a great deal of static background from the pump beam which makes the difference spectra from this subtraction difficult to interpret due to the large background. Instead of subtracting a pump-off spectrum, a spectrum at -50 ps is taken with the pump on and this spectrum is used as a substitute for the pump-off spectrum. At -50 ps, the probe pulse arrives before the pump pulse, thus the spectrum only shows the static background from the pump without any sample dynamics due to excitation. Pump-off spectra are still obtained periodically throughout a scan by blocking the pump beam with a mechanical shutter (Picard Industries) to account for sample changes throughout an experiment.

A.1.4 Data Fitting

The peaks in the transient ultrafast SER spectra were fit to a Gaussian lineshape to obtain peak amplitudes using IGOR. The amplitudes were normalized using the respective peak amplitudes from the pump-off spectrum to obtain percent amplitude decrease relative to the initial signal magnitude. These amplitudes were plotted and then fit to a convolution between an exponential decay and the Gaussian instrument response with the addition of a sigmoidal function with an offset for later time points to obtain the kinetics for the transient features. Figures A2 & A3 include representative ultrafast SER spectra and kinetic fits for 1035 nm pump excitation at 5.92 nJ (24.5 MHz) and 35 nJ (2 MHz), respectively. Table A1 and A2 lists time constant values determined for 1035 nm pump data for powers ranging between 0.4 to 75 nJ. The kinetic fit for the1079 cm^{-1} peak in the 5 nJ transient spectra was not successful due to insufficient signal to noise.

Data collected at different pump wavelengths underwent the same fitting procedure. Table A3 lists time constant values of the 1343 cm^{-1} peak determined for 15 nJ pump excitation for wavelengths ranging between 700 to 1035 nm. Figure A4 and A5 show data for 15 nJ pump excitation at 700 and 800 nm, respectively. The error bars for the amplitudes in the kinetic fits come from the error associated with the Gaussian fit applied to each transient peak.

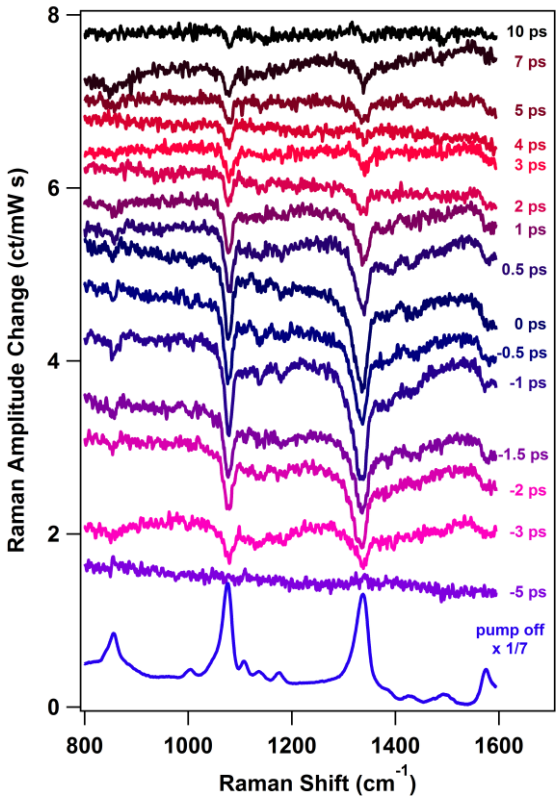

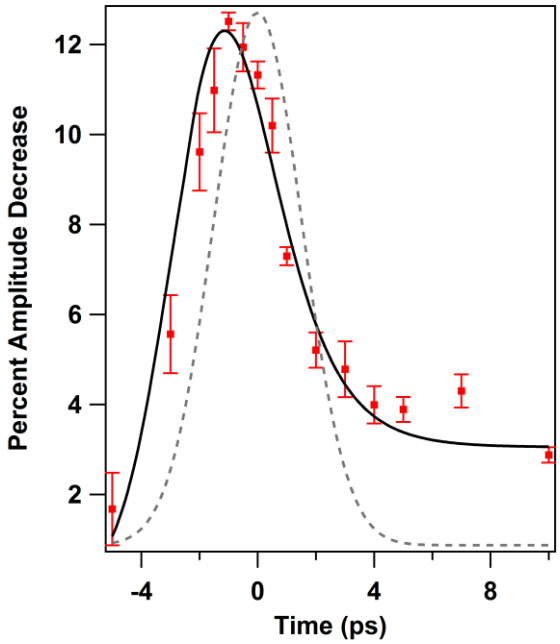

Figure A2. (a) Ultrafast surface-enhanced Raman difference spectra obtained upon excitation with 5.92 nJ of 1035 nm pump pulse, resulting in a transient signal decrease for 4-nitrobenzenthiol modes. (b) convolved fit of 1079 cm^{-1} amplitudes from (a) and instrument response which yields a lifetime of 1.4 ± 0.2 ps for the transient peak depletion.

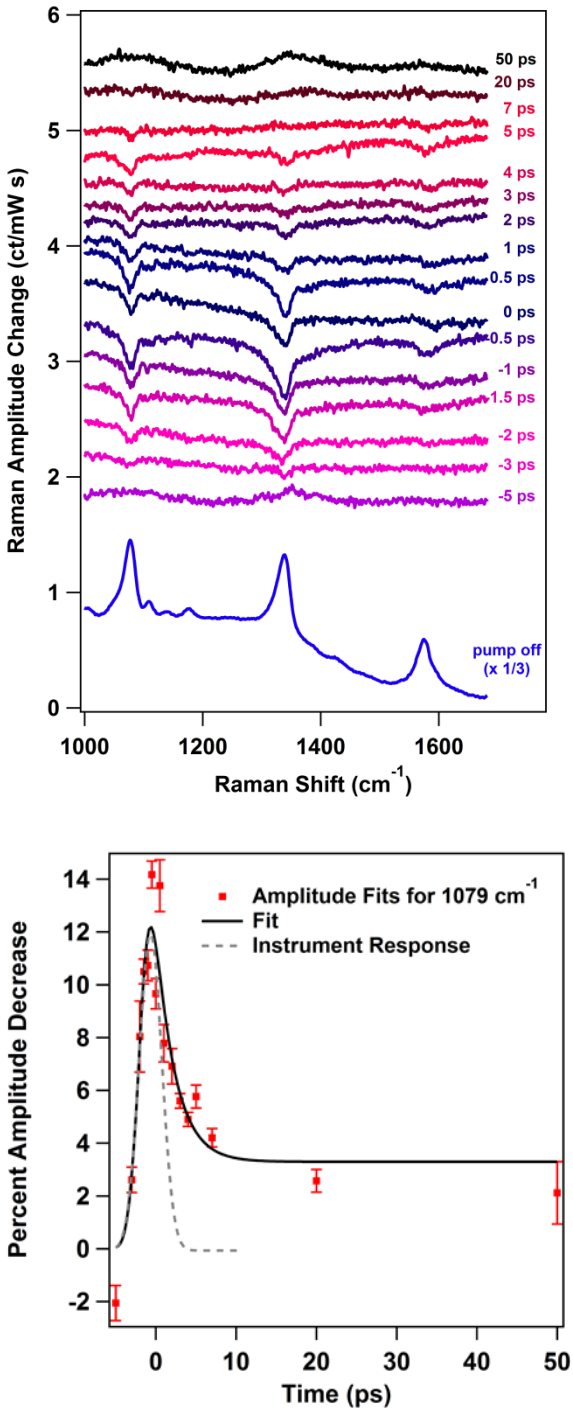

Figure A3. (a) Ultrafast surface-enhanced Raman difference spectra obtained upon excitation with 35 nJ of 1035 nm pump pulse, resulting in a transient signal decrease for 4-nitrobenzenthiol modes. (b) convolved fit of

1343 cm^{-1} amplitudes from (a) and instrument response which yields a lifetime of 2.4 ± 0.3 ps for the transient peak depletion.

Table A1. Lifetimes of transient bleach features as a function of pump power dependence, 2 MHz repetition rate

Pulse Energy (nJ)	**1079 cm^{-1} peak (ps)**	**1343 cm^{-1} peak (ps)**
5	-	2.4 ± 0.3
15	1.8 ± 0.2	3.3 ± 0.2
25	4.4 ± 0.5	5.7 ± 0.6
35	2.0 ± 0.3	2.4 ± 0.3
45	2.7 ± 0.2	4.0 ± 0.7
55	2.8 ± 0.3	2.5 ± 0.1
75	2.4 ± 0.2	1.2 ± 0.1

Table A2. Lifetimes of transient bleach features as a function of pump power dependence, 24.5 MHz repetition rate

Pulse Energy (nJ)	**1079 cm^{-1} peak (ps)**	**1343 cm^{-1} peak (ps)**
0.41	1.9 ± 0.8	1.5 ± 0.1
1.22	2.8 ± 0.2	2.3 ± 0.1
2.04	1.9 ± 0.3	2.2 ± 0.1
2.65	3.6 ± 0.2	3.0 ± 0.1
3.67	3.9 ± 0.9	3.4 ± 0.8
4.45	1.1 ± 0.2	1.0 ± 0.1
5.92	1.4 ± 0.2	1.5 ± 0.1

Table A3. Lifetimes of transient bleach features as a function of wavelength dependence, 15 nJ excitation

Wavelength (nm)	**1343 cm^{-1} peak (ps)**
700	4.9 ± 0.5
750	2.9 ± 0.2
800	1.1 ± 0.1
1035	3.3 ± 0.2

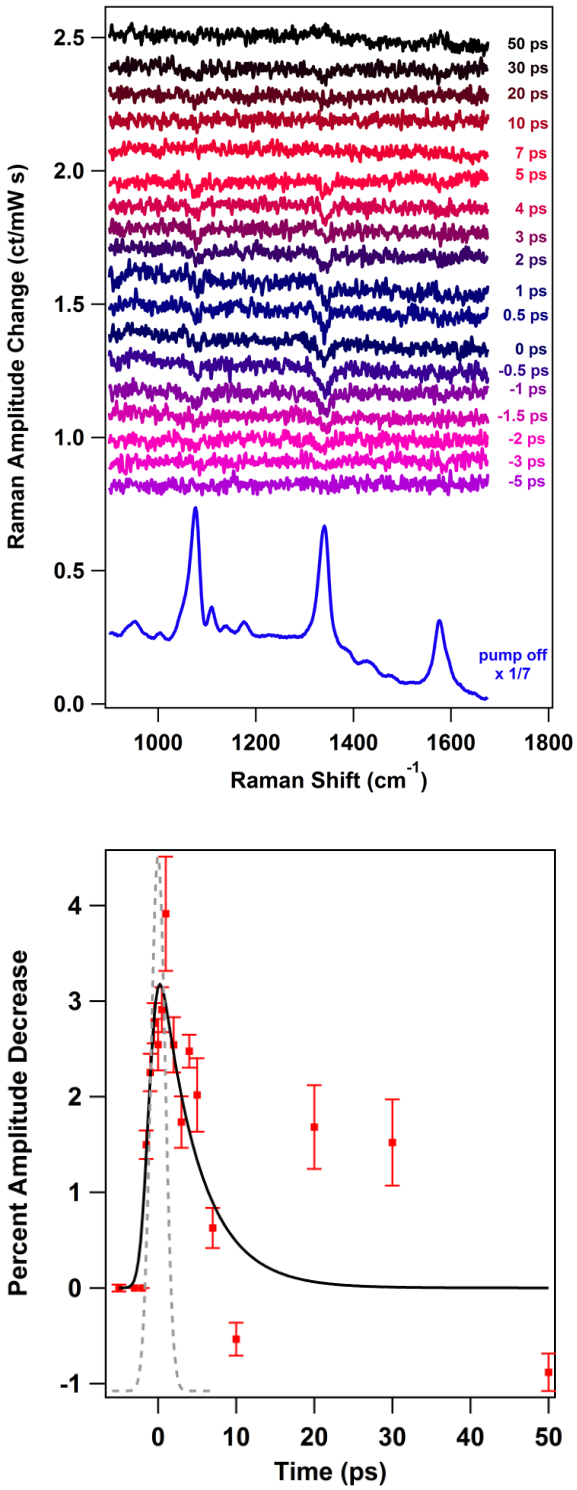

Figure A4. (a) Ultrafast surface-enhanced Raman difference spectra obtained upon

excitation with 15 nJ of 700 nm pump pulse, resulting in a transient signal decrease for 4-nitrobenzenthiol modes. (b) convolved fit of 1343 cm^{-1} amplitudes from (a) and instrument response which yields a lifetime of 4.9 ± 0.5 ps for the transient peak depletion.

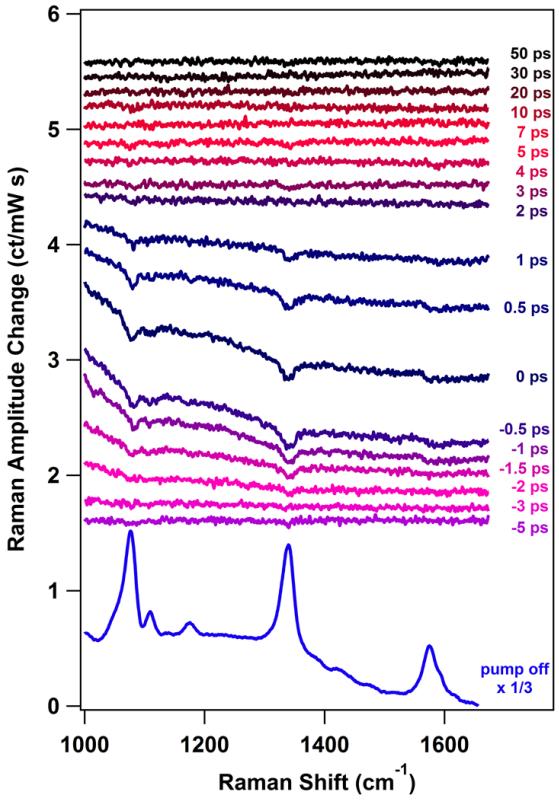

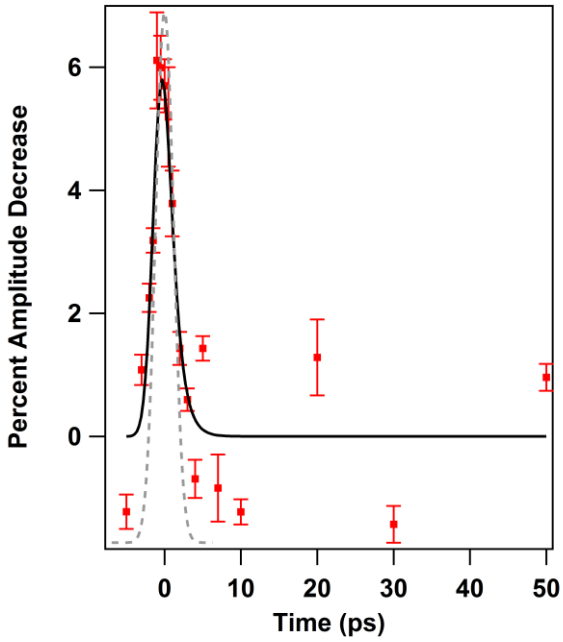

Figure A5. (a) Ultrafast surface-enhanced Raman difference spectra obtained upon excitation with 15 nJ of 800 nm pump pulse, resulting in a transient signal decrease for 4-nitrobenzenthiol modes. (b) convolved fit of 1343 cm^{-1} amplitudes from (a) and instrument response which yields a lifetime of 1.1 ± 0.1 ps for the transient peak depletion.

A.2 Power Dependence

Increasing pump energies may also affect the electron-phonon scattering lifetime. Previous transient absorption studies monitored the lifetime change with respect to pump power from 50 to 160 nJ.[4] As the power increased, the lifetime of the LSPR bleach also increased. The relaxation lifetime of hot electrons is temperature dependent, thus when more energy is added to the system, relaxation times increase.[4] However, our lifetime measurements do not increase at higher pump energies, with pump excitations ranging from 0.5 to 75 nJ (Table A1 & A2). Given the time resolution of our instrument, it is

difficult to resolve differences between the lifetimes measured at different pump energies. Additionally, transient absorption studies track changes occurring on the length scale of the whole nanoparticle, whereas SERS looks at the plasmon-molecule interaction in much smaller hotspot regions. The lack of a trend in the lifetime measurements with increased pump powers for our SERS measurements may simply arise from the differences between SERS and transient absorption measurements.

Although the electron-phonon coupling lifetime measured in our data does not appear to follow with transient absorption data, we believe the same physical phenomenon drives the LSPR shift. As the pump energy increases, we expect the thermal distribution of the electrons to increase. Before excitation, some of the conduction electron density extends beyond the physical nanoparticle. As the temperature of the electrons becomes elevated, the electron density is expected to extend even further from the particle. Additionally, the electron density is inhomogeneous across the aggregate volume.[5,6] This increased charge delocalization potentially allows for greater interaction between hot electrons and molecules adsorbed to the aggregated nanoparticles' surface.

Additionally, the adsorbed molecules may affect the properties of plasmonic nanoparticles.[7,8] In other plasmonic systems, added adsorbates, which interact strongly with the plasmonic nanoparticle, result in stronger plasmon damping, leading to increased scattering of electrons at the nanoparticle/adsorbate interface.[7,9] Hot electrons generated by plasmon excitation populate the surface of the plasmonic substrate and, if sufficiently energetic, may scatter to nearby adsorbed molecules to drive chemical reactions, like H_2 dissociation.[10,11] Thus, the population of hot electrons may be unevenly distributed

among the aggregated nanoparticles in our sample due to the adsorbed 4-NBT molecules, resulting in the decreased charge density that results in the red shift of the LSPR.

Potentially more electrons are interacting with molecules adsorbed to the surface of the nanoparticle, a greater charge density change may arise from charge-transfer between the hot electrons and adsorbed molecules. However, we do not observe a frequency shift which would be expected upon charge-transfer to the adsorbate. There are several possible explanations for this observation. First, the charge transfer may occur but the quantum yield of the charge transfer may be too low for us to detect with our signal to noise. Additionally, 4-NBT may not undergo major frequency shifts upon the addition of an electron to the adsorbed molecule. The electrons could transfer to the solvent, water. Solvated electrons are known to live for nanoseconds, which would still allow them to drive chemistry.[12] Finally, the electrons likely return to the aggregate instead of interacting with the molecules. Additionally, the perceived charge density decrease may arise from the electrons moving away from the molecules in the hot spot. Although the peak depletion magnitude is clearly dependent upon pump pulse energy, it is unclear whether the effect arises solely from a charge-transfer process with adsorbed molecules or nanoparticle expansion due to heating from hot electron-phonon interactions, or a combination of the two.

A.2.1 Estimation of the Number of Photons Driving Plasmon Excitation

From the saturation point in the power dependence data (Fig. 3.4b), we estimated the number of photons that drive plasmon excitation in one Au aggregate by the following calculations.

Photons/Pulse

First, we determined the number of photons per pulse to be 2 x 10^{10} photons by using the pump excitation wavelength (1035 nm) to calculate the energy per photon and the pulse energy at the saturation point (4.4 nJ).

Spot Size/Focal Volume

Then we calculated the spot size to be 126 μm by measuring the power of the pump beam before and after a 50 μm diameter pinhole placed at the sample position and using the values in the following equation (A1):

$$\text{spot size} = 2\sqrt{\frac{-2\left(\frac{d}{2}\right)^2}{\ln\left(1-\frac{p_a}{p_b}\right)}} \qquad \text{(A1)}$$

where d is the diameter of the pinhole, p_b is the power before the pinhole, and p_a is the power after the pinhole.

Number of Aggregates in the Focal Volume

Next, we estimated the number of aggregates in the focal volume. To determine the size of an aggregate, we treated the aggregate as a spherical gold particle with an LSPR maximum > 1250 nm. Using an online widget for Mie scattering,[13] we used the dielectric constants from Johnson and Christy to solve for the radius of the aggregate. We compared extinction plots while changing the radius until we obtained an extinction

spectra that had a local maximum around 1250 nm. From this widget, we estimated the aggregate radius to be ~150 nm.

Using this size estimate and the known size of the monomer AuNPs, we determined that ~50 AuNPs make up an aggregate by dividing the volume of the aggregate by the volume of a AuNP and then multiplying the dividend by a scaling factor, 0.64, that takes into account the random packing of spheres within a sphere.[14] We determined the monomer concentration in the as-synthesized sample based on the synthetic method, the size of the AuNP, and the Au unit cell. By generating a calibration curve with unaggregated samples at varying concentrations (Fig. A6), we determined the AuNP concentration in each sample by using the monomer peak in the spectra for the aggregated samples. From this concentration, we can estimate the number of AuNPs in the focal volume. Based on the monomer concentration, the number of aggregates in the focal volume is ~10^4.

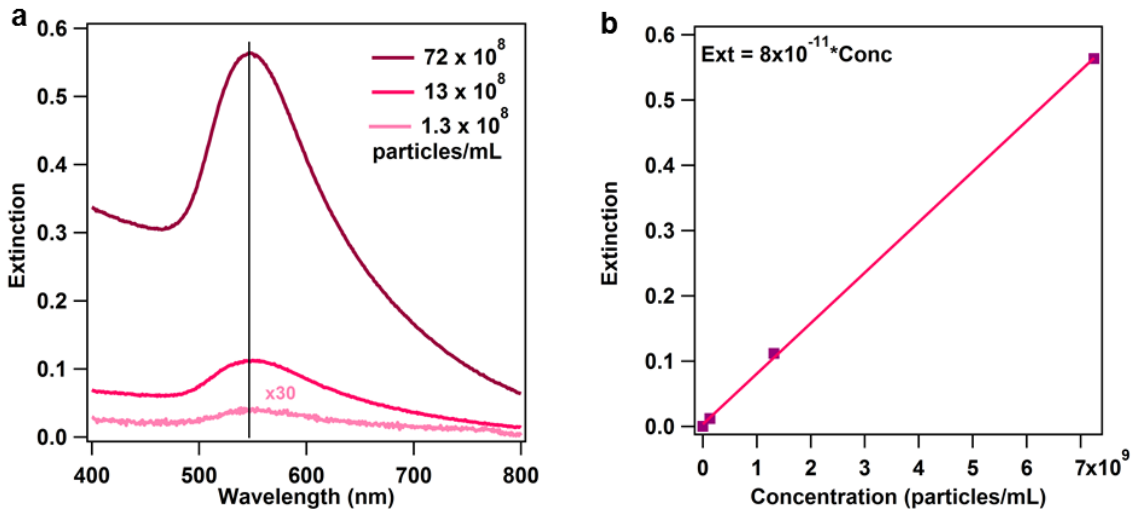

Figure A6. Calibration curve for colloidal gold nanoparticles (a) Extinction spectra of unaggregated AuNP solutions at different concentrations; (b) Extinction measured at λ_{max} (550 nm) plotted against concentration. The cuvette pathlength is 0.2 cm.

Photons/Aggregate/Pulse

Using the number of aggregates in the focal volume and the number of photons per pulse, we determined that an aggregate interacts with ~10^6 photons/pulse. However, there is also a possibility of plasmon re-excitation during one pulse interaction, due to the long pulse duration relative to the plasmon lifetime. Thus, we estimate the number of photons that interact with an aggregate after one pulse to be ~10^5.

Refresh Rate

However, this value does not to take into account the refresh rate of the aggregates due to stirring. With assistance from Miss. Shweta Narayan from Prof. Cari Dutcher's group, we determined the velocity of our stir system to be 2.5 cm/s. Using the spot area, we can estimate the refresh rate to be 1.2 x 10^{-3} mL/s, Using the refresh rate, we can determine how long an aggregate will be in the irradiated volume, which is 0.08 s. Using this length of time and the repetition rate of the laser, each aggregate interacts with ~ 10^6 pulses. With this additional information, we corrected our estimate for the number of photons per aggregate to be on the order of 10^{11}.

A.2.2 Determining the Degree of Charge Delocalization

Using the magnitude of the LSPR red shift, we estimated that 10^9 free electrons are displaced as a result of the charge density change due to plasmon excitation. To begin, we made several assumptions. First, SERS signal magnitude is proportional to LSPR magnitude. Thus, a 10% decrease in SERS signal due to LSPR red shift is equivalent to at 10% decrease in LSPR magnitude at that specific wavelength. Second, the comparison of the blue-edge of a Gaussian LSPR peak from literature to our positive

slope line LSPR is reasonable when assessing LSPR changes due to charge density changes. We also assume that the LSPR shift due to charge density changes is the same for both single particles and aggregates.

Using Figure 6d in Collins et al.,[15] we extrapolate the plot out to a scattering cross section change of 10%. We assume that the scattering cross section and extinction are essentially the same due to the size of our nanoparticles. When scattering cross section change is 10%, the resulting change in charge density is 0.7%. To estimate the number of electrons associated with this percentage, we needed to determine the total number of electrons associated with an aggregate. To do so, we took the estimated radius of the particles and estimated the number of AuNPs that would make up a single aggregate (described previously). Using the number of AuNPs in an aggregate, the radius of the monomer (measured by SEM), and the number of atoms in a gold unit cell, we estimated the number of gold atoms in an aggregate, which is equivalent to the number of conduction electrons. We then took the number of conduction electrons, ~ 10^{11}, and the percent change in charge density, to determine that ~10^{9} electrons are displaced upon plasmon excitation.

A.3 References

(1) Frens, G. Controlled Nucleation for the Regulation of the Particle Size in Monodisperse Gold Suspensions. *Nat. Phys. Sci.* **1973**, *241*, 20–22.

(2) Brandt, N. C.; Keller, E. L.; Frontiera, R. R. Ultrafast Surface-Enhanced Raman Probing of the Role of Hot Electrons in Plasmon-Driven Chemistry. *J. Phys. Chem. Lett.* **2016**, *7* (16), 3179–3185.

(3) Shim, S.; Mathies, R. A. Generation of Narrow-Bandwidth Picosecond Visible Pulses from Broadband Femtosecond Pulses for Femtosecond Stimulated Raman. *Appl. Phys. Lett.* **2006**, *89* (12), 121124.

(4) Link, S.; El-Sayed, M. A. Shape and Size Dependence of Radiative, Non-

Radiative and Photothermal Properties of Gold Nanocrystals. *Int. Rev. Phys. Chem.* **2000**, *19* (3), 409–453.

(5) Jain, P. K.; Qian, W.; El-Sayed, M. A. Ultrafast Electron Relaxation Dynamics in Coupled Metal Nanoparticles in Aggregates. *J. Phys. Chem. B* **2006**, *110* (1), 136–142.

(6) Manjavacas, A.; Nordlander, P.; Kulkarni, V.; Liu, J. G. Plasmon-Induced Hot Carriers in Metallic Nanoparticles. *ACS Nano* **2014**, *8* (8), 7630–7638.

(7) Voisin, C.; Christofilos, D.; Loukakos, P. A.; Del Fatti, N.; Vallée, F.; Lermé, J.; Gaudry, M.; Cottancin, E.; Pellarin, M.; Broyer, M. Ultrafast Electron-Electron Scattering and Energy Exchanges in Noble-Metal Nanoparticles. *Phys. Rev. B* **2004**, *69* (19), 1–13.

(8) Nikoobakht, B.; El-Sayed, M. A. Surface-Enhanced Raman Scattering Studies on Aggregated Gold Nanorods. *J. Phys. Chem. A* **2003**, *107* (18), 3372–3378.

(9) Byers, C. P.; Hoener, B. S.; Chang, W.-S.; Yorulmaz, M.; Link, S.; Landes, C. F. Single-Particle Spectroscopy Reveals Heterogeneity in Electrochemical Tuning of the Localized Surface Plasmon. *J. Phys. Chem. B* **2014**, *118* (49), 14047–14055.

(10) Hendrich, C.; Bosbach, J.; Stietz, F.; Hubenthal, F.; Vartanyan, T.; Träger, F. Chemical Interface Damping of Surface Plasmon Excitation in Metal Nanoparticles: A Study by Persistent Spectral Hole Burning. *Appl. Phys. B* **2003**, *76* (8), 869–875.

(11) Mukherjee, S.; Libisch, F.; Large, N.; Neumann, O.; Brown, L. V; Cheng, J.; Lassiter, J. B.; Carter, E. A.; Nordlander, P.; Halas, N. J. Hot Electrons Do the Impossible: Plasmon-Induced Dissociation of H_2 on Au. *Nano Lett.* **2012**, *13* (1), 240–247.

(12) Mukherjee, S.; Zhou, L.; Goodman, A. M.; Large, N.; Ayala-Orozco, C.; Zhang, Y.; Nordlander, P.; Halas, N. J. Hot-Electron-Induced Dissociation of H_2 on Gold Nanoparticles Supported on SiO_2. *J. Am. Chem. Soc.* **2014**, *136* (1), 64–67.

(13) Siefermann, K. R.; Liu, Y.; Lugovoy, E.; Link, O.; Faubel, M.; Buck, U.; Winter, B.; Abel, B. Binding Energies, Lifetimes and Implications of Bulk and Interface Solvated Electrons in Water. *Nat. Chem.* **2010**, *2* (4), 274–279.

(14) Large, N. Widget-Mie Scattering http://nordlander.rice.edu/miewidget (accessed May 7, 2016).

(15) Collins, S. S. E.; Wei, X.; McKenzie, T. G.; Funston, A. M.; Mulvaney, P. Single Gold Nanorod Charge Modulation in an Ion Gel Device. *Nano Lett.* **2016**, *16* (11), 6863–6869.

Appendix B

Supporting Information for Manuscript:

Ultrafast Nanoscale Raman Thermometry Proves Heating Is Not a Primary Mechanism for Plasmon-Driven Photocatalysis

B.1 Methods

B.1.1 Sample Preparation

Colloidal gold nanoparticles were prepared by following the Frens method for citrate-capped gold nanoparticles with a listed diameter of 97.5 nm.[1] Under heat and stirring, 5.4 mg of gold (III) citrate dissolved in 54 mL DI H_2O were combined with 1% by weight aqueous sodium citrate dihydrate. After 15 minutes, nanoparticles were formed with an average diameter of 80 ± 30 nm, as measured by SEM (JEOL 6700F) using ImageJ software. Samples for ultrafast SERS were prepared by centrifuging 3 mL as-synthesized gold nanoparticles for 30 minutes and removing 2.95 mL of the supernatant. For samples where 4-nitrobenzenthiol (4-NBT) is the analyte, the nanoparticles were aggregated to generate highly enhancing hot spots by adding 70 µL of saturated aqueous 4-nitrobenzenethiol and 330 µL of 0.044 M potassium nitrate dissolved in DI water. For samples containing *trans*-1,2-bis(4-pyridyl)ethylene (BPE), the nanoparticles were aggregated with 50 µL of 0.18 mM *trans*-1,2-bis(4-pyridyl)ethylene dissolved in 190 proof ethanol and 350 µL of 0.032 M potassium nitrate dissolved in DI water. For ultrafast measurements, the samples were placed in a 2 mm quartz cuvette with a stir bar. Stirring the samples minimized precipitation of the aggregates during measurements and refreshed the focal volume. Gold (III) chloride, sodium citrate dehydrate, potassium nitrate, 4-nitrobenzenthiol, and *trans*-1,2-bis(4-pyridyl)ethylene were obtained from Sigma Aldrich and used without further purification. Ethanol was obtained from Pharmco-Aaper.

Extinction spectra for the samples containing 4-NBT were obtained with a Cary-14 UV-Vis spectrometer, while extinction spectra for the BPE samples were obtained with a Shimadzu UV-2600 UV-Vis spectrometer with an integrating sphere (Figure B1).

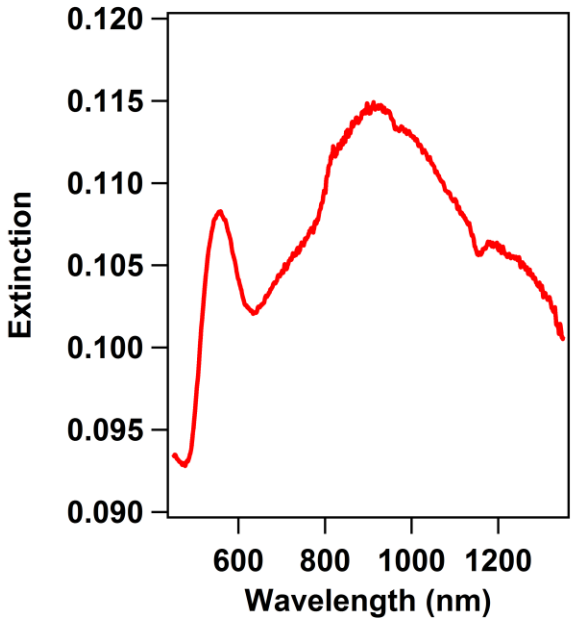

Figure B1. Extinction spectrum of *trans*-1,2-bis(4-pyridyl)ethylene adsorbed to aggregated gold nanoparticles

B.1.2 Instrument Set-up

A detailed description of the ultrafast SERS instrumentation has been published previously.[2] In brief, <250 fs laser pulses, centered at 1035 nm from a fiber amplifier (Clark-MXR Impulse) were split with a 50:50 beam splitter to make the pump and probe beams. The pump beam at 518 nm was generated by SHG in a 3 mm beta-barium borate (BBO) crystal (Newlight Photonics), and the 1035 nm used a portion of the fundamental laser beam directly. The pump beam was sent onto a motorized delay stage (Newport

XMS500) before the sample to vary the time delay. To generate the narrowband picosecond probe beam, the femtosecond pulses were sent into a spectral filter where they were dispersed by a transmission grating onto a slit.[3] After the sample, the spontaneous Raman scattering was directed to a spectrograph (Princeton Instruments, 2300i) with a 600 gr/mm grating blazed at 750 nm or a 300 gr/mm grating blazed at 1 μm onto a 1024 pixel InGaAs array (Princeton Instruments PYLON-IR 1.7). For Stokes measurements, a 1064 nm Raman Edge filter (Edmund Optics 47-510) was placed before the spectrograph and for anti-Stokes measurements a 1000 nm short pass filter (Thorlabs, FESH1000) was used. The data were collected using home-written LabView code. The instrument response of this set-up is 2.8 ps, as measured by the optical Kerr effect in toluene while the spectral resolution is 13 cm^{-1}, as measured from the 800 cm^{-1} mode of cyclohexane.

The probe energy was 1 nJ with a spot size of 1 x 10^{-4} cm^2 and the pump energies ranged from 1 to 10 nJ with a spot size of 5 x 10^{-4} cm^2 for 1035 nm excitation and 6 x 10^{-4} cm^2 for 518 nm excitation. Each spot radius was determined by measuring the power before and after a 50 μm diameter pinhole at the sample position and placing the values in the following equation (B1):

$$\text{spot radius} = 2\sqrt{\frac{-2\left(\frac{d}{2}\right)^2}{\ln\left(1-\frac{p_a}{p_b}\right)}} \qquad \text{(B1)}$$

where d is the diameter of the pinhole, p_b is the power before the pinhole, and p_a is the power after the pinhole. Table B1 & B2 list the probe and pump peak energy, fluence, flux, and peak power at 1035 nm and 518 nm, respectively.

Table B1. List of photoexcitation and probe peak energy, fluence, flux, and peak power for each photoexcitation energy at 1035 nm

Pump	Peak Energy (nJ)	Fluence ($\mu J/cm^2$)	Flux (W/cm^2)	Peak Power	
	1	2	50	8 MW/cm^2	0.3 J/cm^2
	4	8	200	30 MW/cm^2	1 J/cm^2
	10	20	500	80 MW/cm^2	3 J/cm^2
Probe	1	10	250	3 MW/cm^2	0.1 J/cm^2

Table B2. List of photoexcitation peak energy, fluence, flux, and peak power for each photoexcitation energy at 518 nm

Pump	Peak Energy (nJ)	Fluence ($\mu J/cm^2$)	Flux (W/cm^2)	Peak Power	
	1	2	40	6 MW/cm^2	0.3 J/cm^2
	4	7	160	26 MW/cm^2	1.0 J/cm^2

B.1.3 Data Collection and Processing

Each spectrum consists of 3 spectra that were acquired for 20s and averaged together. For each time point, a pump-only spectrum was obtained to subtract out the static pump background from each spectrum taken with both the pump and probe.

B.1.4 Calculating the Wavelength-Dependent Instrument Response Function

First, we obtained the specification sheets for the gratings (300 gr/mm blazed at 1 μm and 600 gr/mm blazed at 750 nm) from Richardson Gratings and the InGaAs array (Pylon-IR 1.7) from Princeton Instruments. We then determined the wavelength of each mode on the anti-Stokes and Stokes sides of the laser line at 1035 nm and extrapolated the respective efficiencies of the detector components at each wavelength. To obtain the

overall detector efficiency, we multiplied the grating efficiency with the InGaAs array efficiency. The overall detector efficiency at each wavelength was then used to scale the amplitudes of the anti-Stokes and Stokes peaks to account for wavelength dependent detector efficiencies. .

B.1.5 Estimating Thermal Contribution for Plasmonic Photocatalysis Reported in the Literature

Using the power dependence from Figure 4.3b, we created a calibration curve for plasmonic heating with respect to the photoexcitation peak power (Figure B2). The examples chosen from the literature use continuous wave (CW) excitation while our experiments rely on pulsed lasers. To account for this difference, we converted our pump flux to peak power (Table B1) and assume that the plasmonic heating response is linear across the entire range of pump powers. Using the maximum excitation fluxes reported in the literature, we extrapolate the thermal contribution for each plasmon-driven process (Table B3) by inputting the flux into the equation obtained from the calibration curve (ΔTemperature = $1*10^{-6}$ (flux)). Due to the many assumptions and error in our calibration curve, we only report order of magnitude values for the scattering-induced thermal contribution in these examples. Our values agree with reports from some of the authors that heating of their samples does not produce similar reaction yields as photoexcitation.[4,5]

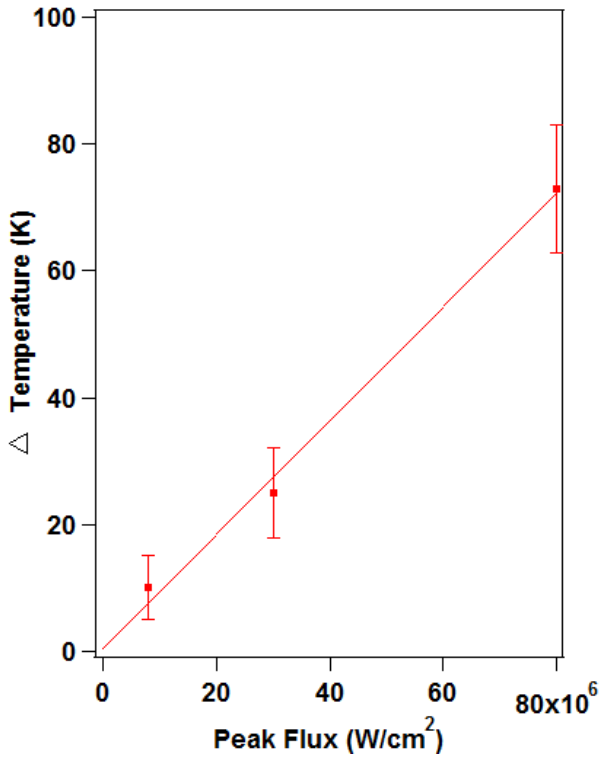

Figure B2. Calibration curve for plasmonic heating with respect to photoexcitation peak powers. The equation for the linear fit is Temperature = $1x10^{-6}$ flux

Table B3. List of select literature examples of plasmonic photocatalysis and the estimated thermal contribution for each set of reaction conditions

Ref. number in main text	Reaction	Flux (W/cm^2)	Thermal Contribution (K)
5	H_2O splitting	12000	0.01
16	Ethylene Epoxidation	0.25	1×10^{-7}
43	Acetylene Hydrogenation	14.3	1×10^{-5}

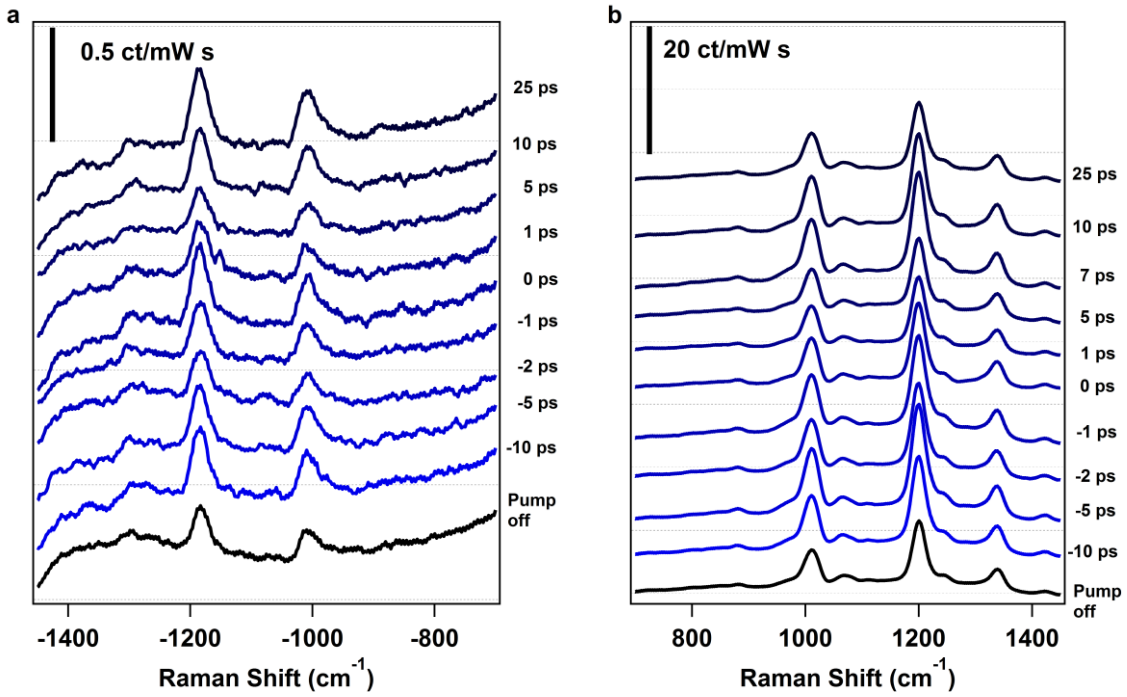

Figure B3. Ultrafast surface-enhanced (a) anti-Stokes and (b) Stokes Raman spectra of *trans*-1,2-bis(4-pyridyl)ethylene adsorbed to colloidal gold nanoparticles with 200 W/cm^2 photoexcitation flux and 250 W/cm^2 probe flux. Spectra are offset for clarity.

B.2 References

(1) Frens, G. Controlled Nucleation for the Regulation of the Particle Size in Monodisperse Gold Suspensions. *Nat. Phys. Sci.* **1973**, *241*, 20–22.

(2) Keller, E. L.; Frontiera, R. R. Monitoring Charge Density Delocalization upon Plasmon Excitation with Ultrafast Surface-Enhanced Raman Spectroscopy. *ACS Photonics* **2017**, *4* (5), 1033–1039.

(3) Shim, S.; Mathies, R. A. Generation of Narrow-Bandwidth Picosecond Visible Pulses from Broadband Femtosecond Pulses for Femtosecond Stimulated Raman. *Appl. Phys. Lett.* **2006**, *89* (12), 121124.

(4) Swearer, D. F.; Zhao, H.; Zhou, L.; Zhang, C.; Robatjazi, H.; Mark, J.; Martirez, P. Heterometallic Antenna − Reactor Complexes for Photocatalysis. *Proc. Natl. Acad. Sci. U. S. A.* **2016**, *113* (32), 8916–8920.

(5) Christopher, P.; Xin, H.; Linic, S. Visible-Light-Enhanced Catalytic Oxidation Reactions on Plasmonic Silver Nanostructures. *Nat. Chem.* **2011**, *3* (6), 467–472.

Appendix C

Supporting Information for Manuscript:

Effect of Silica Supports on Plasmonic Heating of Molecular Adsorbates as Measured by Ultrafast Surface-Enhanced Raman Thermometry

C.1 Methods

C.1.1 Sample Preparation

Citrate-capped AuNP Aggregates. Colloidal gold nanoparticles were prepared by following the Frens method for citrate-capped gold nanoparticles with a listed diameter of 97.5 nm.[1] Under heat and stirring, 5.4 mg of gold (III) citrate dissolved in 54 mL DI H_2O were combined with 0.227 mL of 1% by weight aqueous sodium citrate dihydrate. After 15 minutes, nanoparticles were formed with an average diameter of 80 ± 30 nm, as measured by SEM (JEOL 6700F) using ImageJ software. Samples for ultrafast SERS were prepared by centrifuging 3 mL as-synthesized gold nanoparticles for 30 minutes and removing 2.95 mL of the supernatant. The nanoparticles were aggregated with 50 µL of 0.18 mM *trans*-1,2-bis(4-pyridyl)ethylene dissolved in 190 proof ethanol and 350 µL of 0.032 M potassium nitrate dissolved in DI water. For ultrafast measurements, the samples were placed in a 2 mm quartz cuvette with a stir bar. Stirring the samples minimized precipitation of the aggregates during measurements and refreshed the focal volume. Gold (III) chloride, sodium citrate dehydrate, potassium nitrate, and *trans*-1,2-bis(4-pyridyl)ethylene were obtained from Sigma Aldrich and used without further purification. Ethanol was obtained from Pharmco-Aaper.

Mesoporous Silica AuNR. The mesoporous silica-coated gold nanorods (AuNRs@mSiO_2) were synthesized with a modified Stöber method.[2] First, the as-purchased CTAB-stabilized AuNRs were centrifuged once to lower CTAB concentrations (1 mM CTAB-stabilized in water, OD = 1.1, 0.045 mg/mL of Au). The pellets of 0.45 mg of Au were resuspended in 1 mL of CTAB-decane micelle suspension

to yield 1 nM AuNRs. The micelle suspension was prepared by sonicating CTAB and decane mixture in water. The decane-CTAB mixture can form micelles which have been known to create larger pore diameters of silica shells than those of silica shells synthesized with just CTAB micelles.[3] The CTAB and decane concentrations were 1.0 mM and 1.5 mM, respectively. The 1 nM AuNRs suspension was transferred to 15 x 34 mm vials with a magnetic stirring bar, and the suspension was stirred for at least 3 hours at room temperature. While continuously stirring, 5 μL of 0.1 M NaOH and 4 μL of 20% TEOS in ethanol were added, subsequently. The suspension was stirred again for 24 hours. For AuNRs@mSiO_2 modified with chlorotrimethylsilane (TMS) or 2-[methoxy(polyethyleneoxy)$_{9\text{-}12}$propyl]trimethoxysilane (PEG), 5 μL of 0.1 M NaOH was added again and stirred for 30 min. Then, excess TMS or PEG were added to the suspensions with stirring for the next 48 hours. For purification, the suspensions were centrifuged and resuspended in 6 mL of ethanolic ammonium nitrate solution (6 g of NH_4NO_3 in 1 L ethanol) and refluxed twice for 30 min at 60°C. After reflux, the suspensions were washed three times via centrifugation in 99% ethanol. The final products were stored in 99% ethanol. The average thickness of the silica shells at the tip was 8 ± 2 nm as measured by TEM (n=100). Tetraethylorthosilicate (TEOS), hexadecyltrimethylammonium bromide (CTAB) chlorotrimethylsilane (TMS) were purchased from Sigma Aldrich. 2-[methoxy(polyethyleneoxy)$_{9\text{-}12}$propyl]trimethoxysilane (PEG, average molecular weight 657 g/mol) was purchased from Gelest. Decane was purchased from TCI Chemicals. CTAB-stabilized AuNRs (LSPR λ_{max}=808 nm) were purchased from Nanohybrids and used without further surface functionalization. All

chemicals were used without further purification. For SERS measurements, 5 µL of 1.8 mM BPE were added to 200 µL of 6 x 10^{11} nanorod/mL mesoporous silica AuNRs. The samples were allowed to incubate for 12 hours.

Silica encapsulated AuNP dimers. Silica encapsulated AuNP dimers, also known as SERS440 nanotags, were obtained from Becton Dickinson. The samples consist of 60 nm diameter gold core with *trans*-1,2,-bis(4-pyridyl)ethylene adsorbed to the surface. The gold cores are surrounded with a ~50 nm thick silica shell. The sample contains primarily monomers, but also contain some dimers and oligomers which give rise to the SERS signal at 1035 nm. These samples were used without further purification.

CTAB-capped AuNR. AuNR were obtained from Nanohybyrids. The AuNRs have a width of 9.9 ± 0.9 nm and a length of 42 ± 4 nm, with an aspect ratio of 4.2. The AuNRs are capped with CTAB and were used without further purification. For SERS measurements, 5 µL of 1.8 mM BPE were added to 200 µL of 7.5 x 10^{11} nanorod/mL AuNRs.

C.1.2 Materials Characterization

Extinction spectra for the samples were obtained with a Shimadzu UV-2600 UV-Vis spectrometer with an integrating sphere.

Transmission electron micrographs for the AuNRs@mSiO_2 were taken with a FEI Tecnai T12 at 120 kV. The purified AuNRs@mSiO_2 were dispersed in ethanol and

Formvar/carbon-coated copper grids (Ted Pella, INC, Redding, CA) were dipped into the ethanolic suspensions. The grids were then dried in air to prepare TEM samples.

Scanning electron micrographs for bare AuNP aggregates and silica encapsulated AuNP dimers were taken with a JEOL 6700F at 5 kV and 10 kV, respectively. The samples were prepared by dropcasting 3 μL of the sample onto carbon-coated copper grids (Electron Microscopy Sciences) and left in air until the solvent evaporated.

C.1.3 Instrument Set-up

A detailed description of the ultrafast SERS instrumentation has been published previously.[4] In brief, <250 fs laser pulses, centered at 1035 nm from a fiber amplifier (Clark-MXR Impulse) were split with a 50:50 beam splitter to make the pump and probe beams. The pump beam at the 1035 nm used a portion of the fundamental laser beam directly. The pump beam was sent onto a motorized delay stage (Newport XMS500) before the sample to vary the time delay. To generate the narrowband picosecond probe beam, the femtosecond pulses were sent into a spectral filter where they were dispersed by a transmission grating and then focused onto a slit with a cylindrical lens.[5] After the sample, the spontaneous Raman scattering was directed to a spectrograph (Princeton Instruments, Acton SP2300) with a 300 gr/mm grating blazed at 1 μm onto a 1024 pixel InGaAs array (Princeton Instruments PYLON-IR 1.7). For Stokes measurements, a 1064 nm Raman Edge filter (Edmund Optics 47-510) was placed before the spectrograph and for anti-Stokes measurements a 1000 nm short pass filter (Thorlabs, FESH1000) was used. The data were collected using home-written LabView code. The instrument

response of this set-up is 2.8 ps, as measured by the optical Kerr effect in toluene while the spectral resolution is 17 cm^{-1}, as measured from the 786 cm^{-1} mode of toluene.

For the ultrafast Raman thermometry measurements, the probe energy was 2 nJ with a spot size of 1 x 10^{-4} cm^2 and the pump energy was 1 nJ with a spot size of 5 x 10^{-4} cm^2 for 1035 nm excitation. Each spot radius was determined by measuring the power before and after a 50 μm diameter pinhole at the sample position and placing the values in the following equation (C1):

$$\text{spot radius} = 2\sqrt{\frac{-2\left(\frac{d}{2}\right)^2}{\ln\left(1-\frac{p_a}{p_b}\right)}} \quad \text{(C1)}$$

where d is the diameter of the pinhole, p_b is the power before the pinhole, and p_a is the power after the pinhole. Table C1 lists the probe and pump peak energy, fluence, flux, and peak power at 1035 nm.

Table C1. List of peak energy, fluence, flux, and peak power for each photoexcitation and probe energy at 1035 nm

Beam	Peak Energy (nJ)	Fluence (μJ/cm^2)	Flux (W/cm^2)	Peak Power	
Pump	1	2	50	8 MW/cm^2	0.3 J/cm^2
Probe	2.0	14	350	5.4 MW/cm^2	0.22 J/cm^2
	1.2	8.6	210	3.2 MW/cm^2	0.13 J/cm^2
	2.9	20	490	7.5 MW/cm^2	0.31 J/cm^2
	3.7	26	630	9.6 MW/cm^2	0.39 J/cm^2
	4.5	31	770	12 MW/cm^2	0.48 J/cm^2
	5.3	37	910	14 MW/cm^2	0.57 J/cm^2
	6.1	43	1050	16 MW/cm^2	0.66 J/cm^2

C.1.4 Data Collection and Processing

For the ultrafast SERS data, each spectrum consists of 3 spectra that were acquired for 10s and averaged together. For each time point, a pump-only spectrum was obtained to subtract out the static pump background from each spectrum taken with both the pump and probe. An example of the spectra obtained from these measurements is shown in Figure C1 for the silica encapsulated AuNP dimers with 50 W/cm^2 photoexcitation.

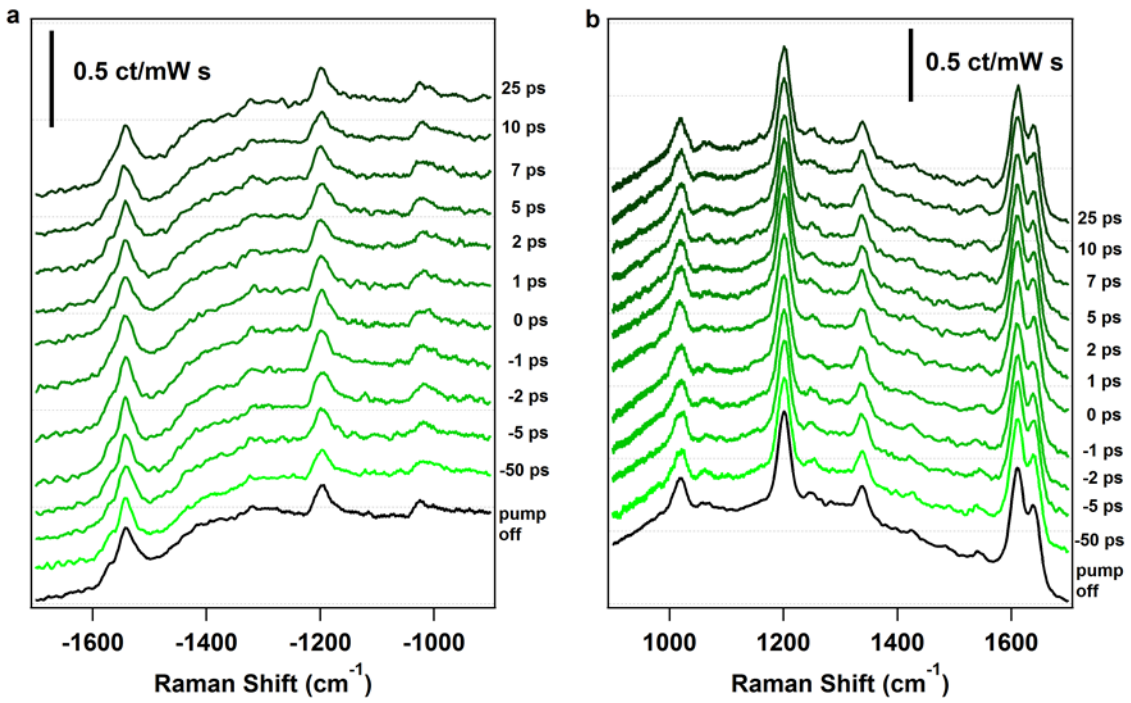

Figure C1. Ultrafast surface-enhanced (a) anti-Stokes and (b) Stokes Raman spectra of silica encapsulated AuNP dimers with 50 W/cm^2 photoexcitation flux and 500 W/cm^2 probe flux. Spectra are offset for clarity.

For the steady state measurements, each spectrum consists of 3 spectra that were acquired for 10s and averaged together. In Figure 5.4, each data point is the average of 4 separate measurements of the anti-Stokes and Stokes Raman intensity ratio. Figure C2-C5 shows representative spectra for each sample obtained at the fluxes listed in Figure 5.4.

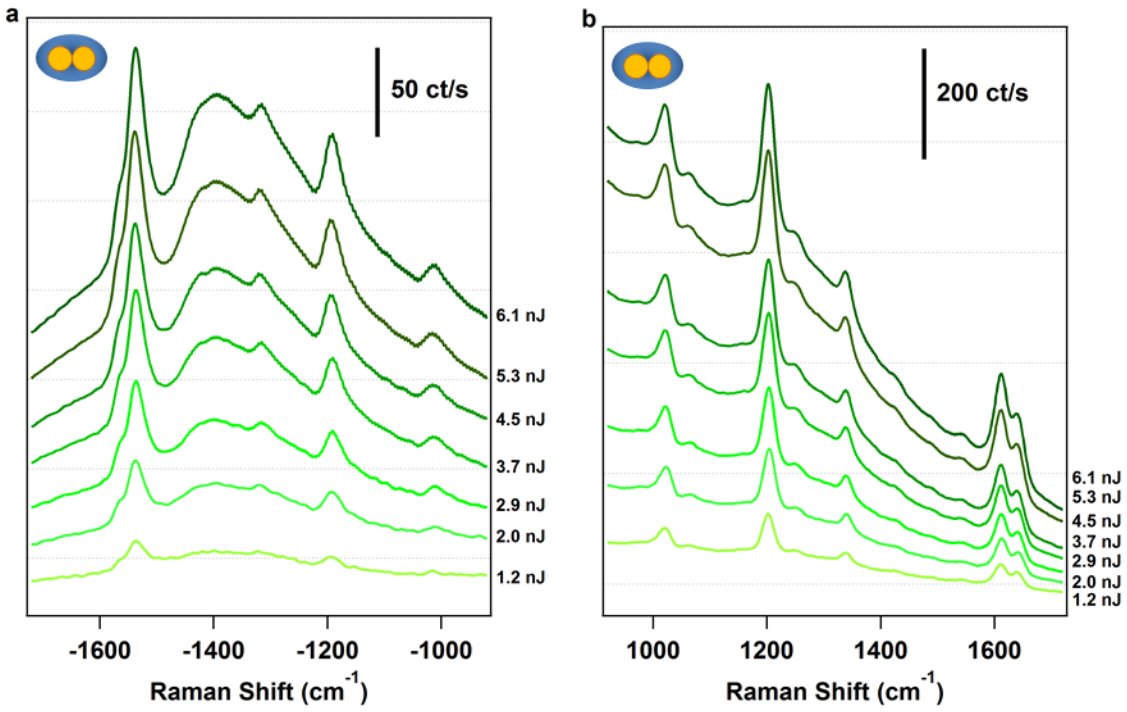

Figure C2. Surface enhanced (a) anti-Stokes and (b) Stokes Raman spectra obtained on silica encapsulated AuNP dimers with fluxes ranging between 210 W/cm^2 and 1050 W/cm^2. Spectra are offset for clarity.

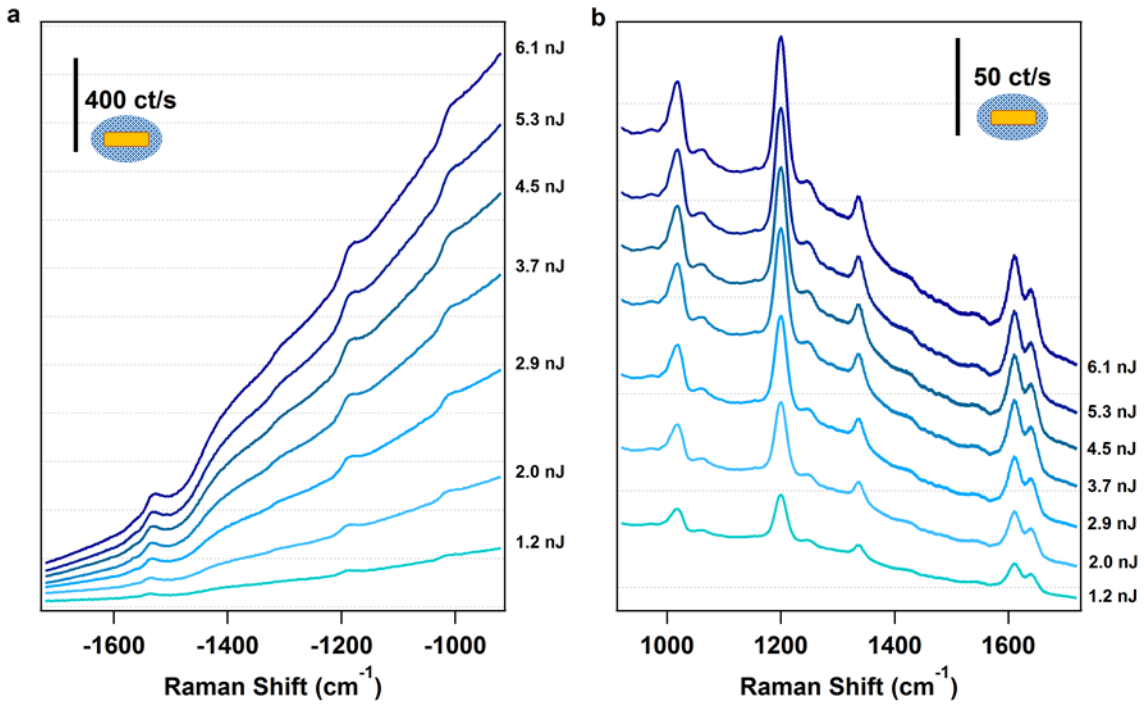

Figure C3. Surface enhanced (a) anti-Stokes and (b) Stokes Raman spectra obtained on mesoporous silica AuNRs (TMS) with fluxes ranging between 210 W/cm^2 and 1050 W/cm^2. Spectra are offset for clarity.

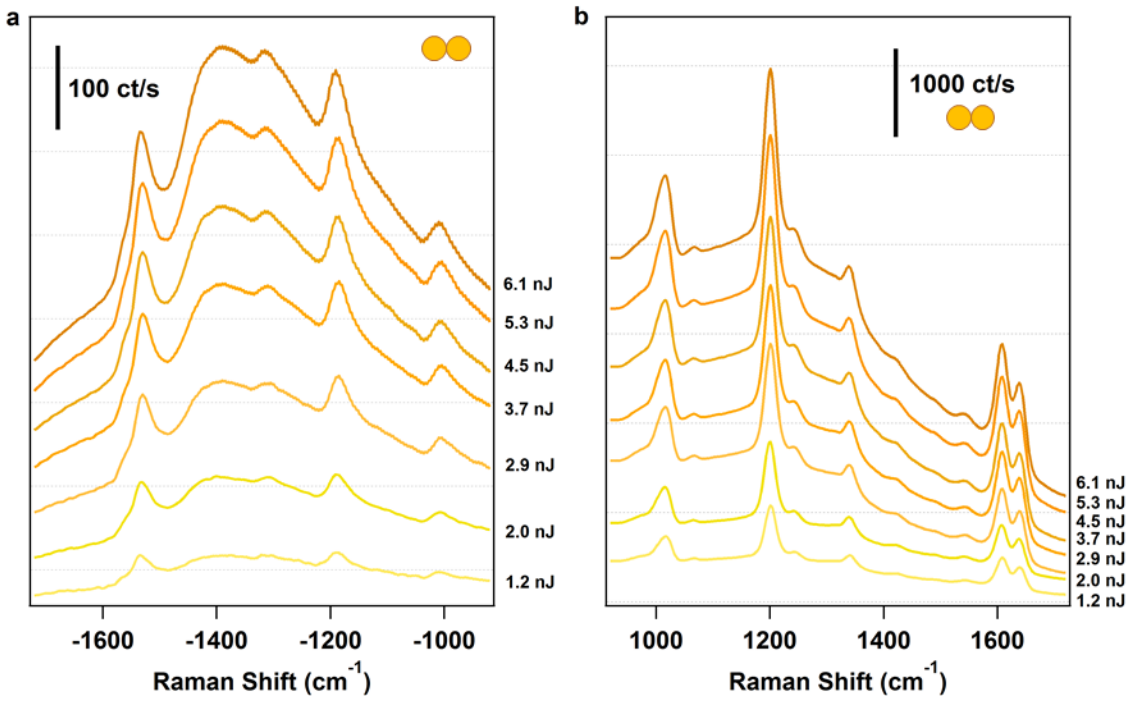

Figure C4. Surface enhanced (a) anti-Stokes and (b) Stokes Raman spectra obtained on citrate-capped AuNP aggregates with fluxes ranging between 210 W/cm^2 and 1050 W/cm^2. Spectra are offset for clarity.

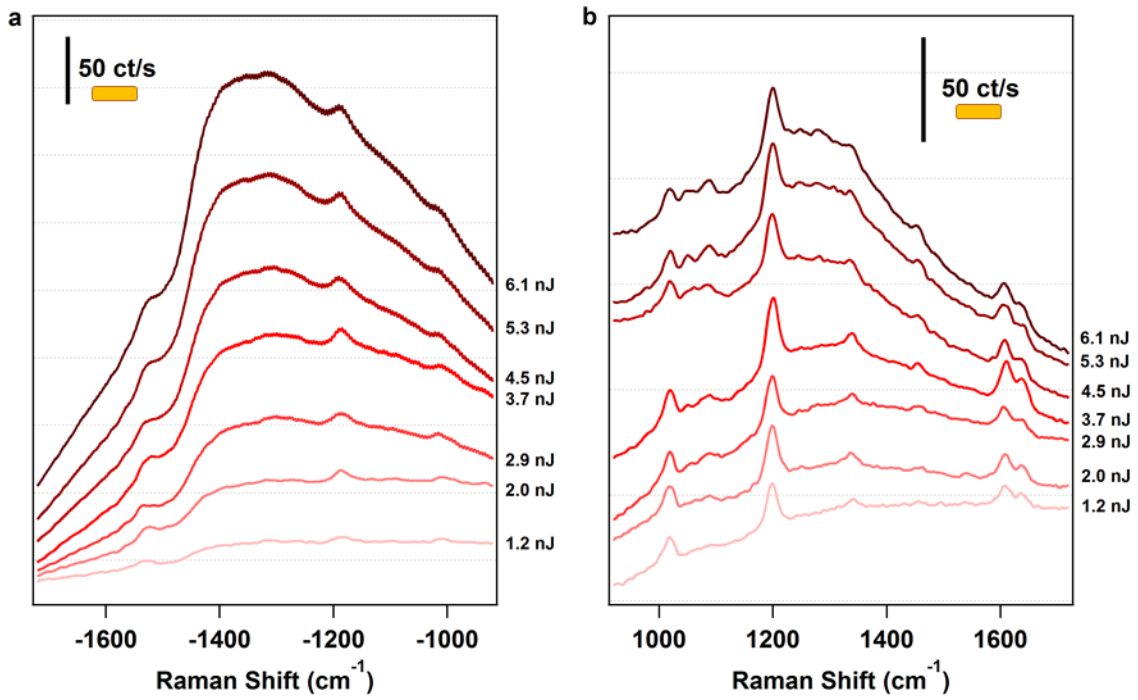

Figure C5. Surface enhanced (a) anti-Stokes and (b) Stokes Raman spectra obtained on CTAB-capped AuNRs with fluxes ranging between 210 W/cm^2 and 1050 W/cm^2. Spectra are offset for clarity.

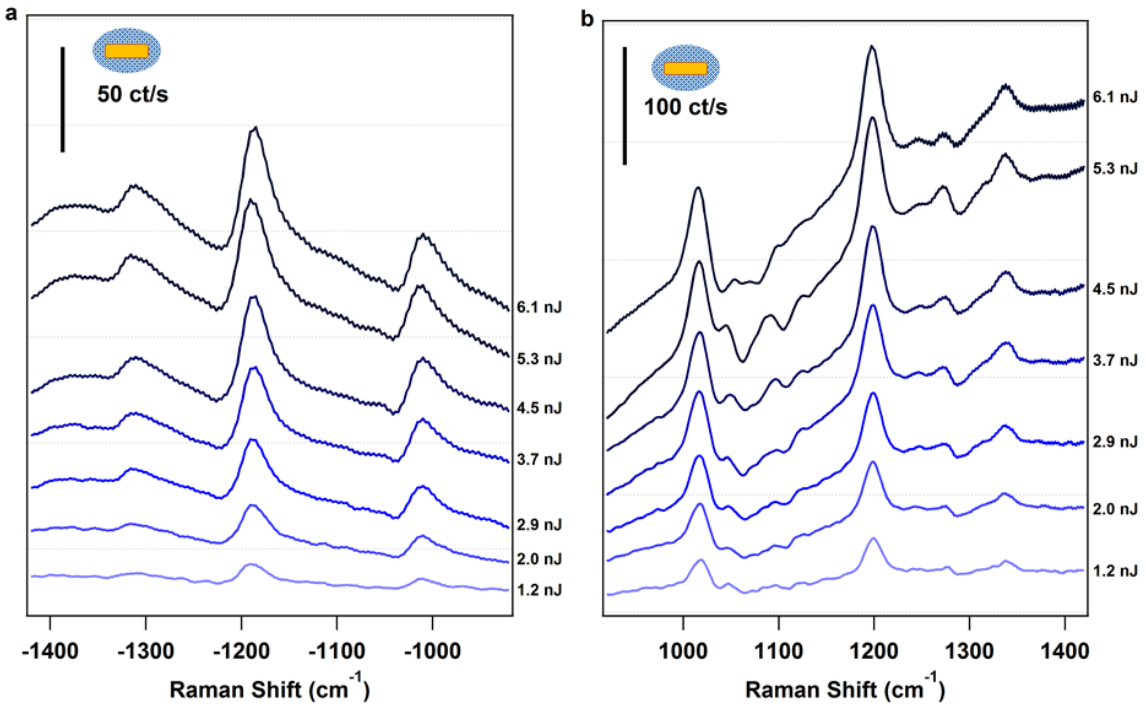

Figure C6. Surface-enhanced (a) anti-Stokes and (b) Stokes Raman spectra obtained on mesoporous silica AuNRs (PEG) with fluxes ranging between 210 W/cm^2 and 1050 W/cm^2. Spectra are offset for clarity

Mesoporous silica AuNRs (PEG). In addition to mesoporous silica AuNRs synthesized with a relatively hydrophobic silane (TMS), we also synthesized mesoporous silica shells with a more hydrophilic silane (PEG). Both syntheses generate similar mesoporous silica shell thickness and pore sizes. We performed the same set of experiments described for Figure 5.4 to obtain spectra at various fluxes (Figure C6). After fitting the 1200 cm^{-1} mode and normalizing the peak amplitudes with respect to the LSPR magnitude (Figure C7a) and the detector efficiency, we obtain a temperature for each flux (Figure C7b). Unsurprisingly, the temperatures are essentially identical to the TMS mesoporous silica AuNRs, which we would expect based on the similar properties between the two mesoporous silica shells. However, upon closer examination of the SER spectra in Figure C3 and C6, the signal magnitudes between the TMS and PEG

mesoporous silica AuNRs are comparable. Based on previous measurements, we would expect that the addition of PEG would limit access to the surface of the AuNR We did not see evidence of this which may be due to hydrolysis of PEG after synthesis or the lack of incorporation of PEG into the shell during synthesis. For these reasons, we removed the data from Chapter 5 and added it to Appendix C. Even with the uncertainty about the incorporation of PEG in the mesoporous silica shell, the results we obtained with these samples match with what we would expect for a mesoporous silica shell with similar pore sizes and overall thickness as the TMS samples and does not change any of our conclusions.

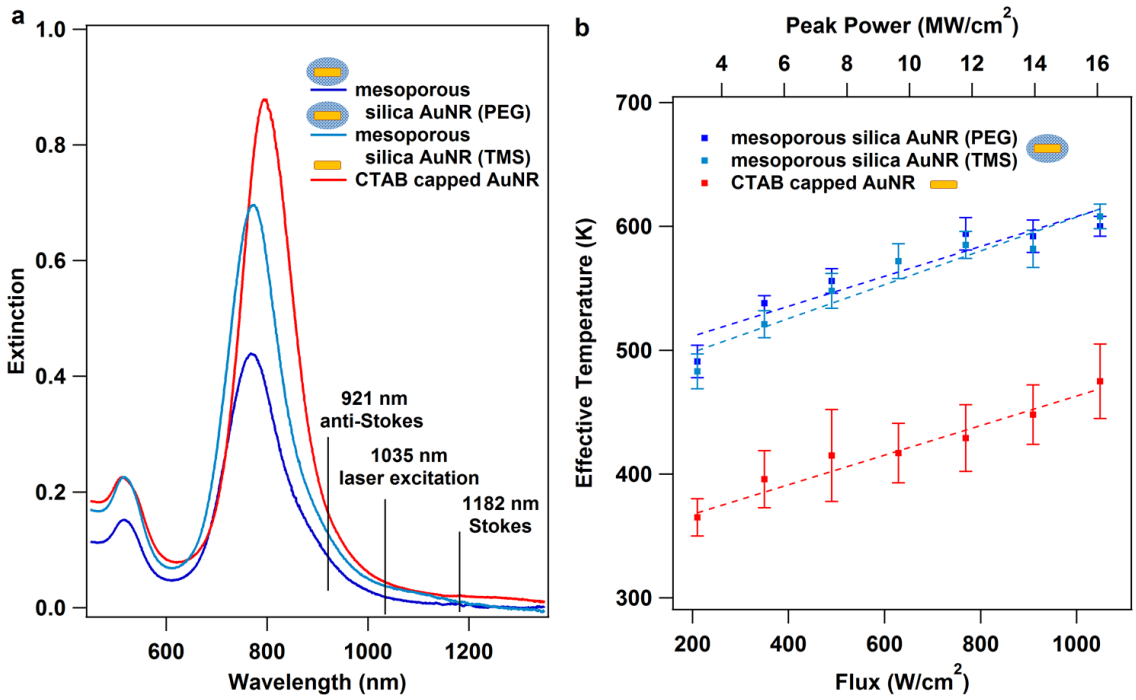

Figure C7. Comparison of CTAB-coated and mesoporous silica coated AuNRs (a) Extinction spectrum for both mesoporous silica AuNR samples (TMS & PEG) and the CTAB-capped AuNRs (b) Temperature plotted against flux (and peak power) for both mesoporous silica AuNRs and CTAB-capped AuNRs. Both mesoporous silica samples exhibit similar heating responses as we would expect due to comparable pore sizes between the two samples.

C.1.5 Calculating Effective Temperature

Applying Boltzmann Distribution Analysis. To calculate effective temperatures from the spectra collected, we apply a Boltzmann distribution analysis as described by the following equation (C2):[4]

$$\text{Effective Temperature (K)} = \frac{-\text{Energy of Vibration (J)}}{k_b * \ln\left(\frac{\text{Intensity}_{\text{anti-Stokes}}}{C * \text{Intensity}_{\text{Stokes}}}\right)} \quad \text{(C2)}$$

where k_b is the Boltzmann constant and C accounts for the wavelength dependent Raman scattering efficiency. We obtain the intensities by fitting the 1200 cm^{-1} peak, corresponding to the ethylene symmetric stretch of *trans*-1,2-bis(4-pyridyl)ethylene, to a Gaussian to extrapolate out the peak amplitudes. Before we can apply the Boltzmann distribution analysis, we must account for the wavelength dependent enhancement of SERS,[6] by normalizing the Raman intensities by the LSPR magnitude at the respective wavelength for the anti-Stokes and Stokes Raman peak. During this step, we also scale the Raman intensities with respect to the detector efficiency at the respective wavelengths, as described below. Once properly scaled, the intensities can be used in Equation C2 to obtain an effective temperature for each data point.

Calculating the Wavelength Dependent Instrument Response Function. First, we obtained the specification sheets for the grating (300 gr/mm blazed at 1 μm) from Richardson Gratings and the InGaAs array (Pylon-IR 1.7) from Princeton Instruments. We then determined the wavelength of each mode on the anti-Stokes and Stokes sides of the laser line at 1035 nm and extrapolated the respective efficiencies of the detector components at each wavelength. To obtain the overall detector efficiency, we multiplied

the grating efficiency with the InGaAs array efficiency. The overall detector efficiency at each wavelength was then used to scale the amplitudes of the anti-Stokes and Stokes peaks to account for wavelength dependent detector efficiencies. An additional correction factor was added to the overall detector efficiency to account for day to day changes, which may arise due to differences in alignment. The correction factor was obtained by fitting the 786, 1004, and 1211 cm^{-1} of toluene and applying the Boltzmann distribution analysis described above. If the temperatures obtained were not within error of room temperature, a correction factor was extrapolated based on the difference between the measured temperature and room temperature. This correction factor was then applied to the overall detector efficiency and used to scale spectral intensities before the Boltzmann distribution analysis.

C.1.6 Specific Heat Capacity and Thermal Conductivity for Each Material

Estimating Heat Capacity and Thermal Conductivity for Mesoporous Silica AuNRs. Table C2 lists the heat capacity and thermal conductivity of each material near the adsorbates. The thermal properties for the mesoporous silica AuNRs are a combination of the mesoporous silica shell and the solvent present in the pores. Based upon the average pore size (7 ± 3 nm) and previously published surface area measurements taken before and after analyte addition,[7] we assume that the solvent contribution to the thermal properties of mesoporous silica AuNRs is 25 – 33%. Thus, we can estimate the thermal properties for the mesoporous silica AuNRs as shown in Table 5.1 and C2.

Table C2. Specific heat capacities and thermal conductivities for each material near the adsorbates

Material	Specific Heat Capacity	Thermal Conductivity
water	4.18 J/g K	0.59 W/ m K
ethanol	2.46 J/g K	0.169 W/ m K
silica	0.73 J/g K[8]	1 − 1.4 W/ m K[9,10]
mesoporous silica	0.84 J/g K[8]	0.2 − 0.4 W/m K[11,12]
mesoporous silica AuNRs	> 0.84 J/g K	0.2 − 0.3 W/m K
CTAB-capped AuNRs	1.6 – 4.18 J/mL K[13,14]	0.22 – 0.24 W/m K[13,14]

C.2 References

(1) Frens, G. Controlled Nucleation for the Regulation of the Particle Size in Monodisperse Gold Suspensions. *Nat. Phys. Sci.* **1973**, *241*, 20–22.

(2) Gorelikov, I.; Matsuura, N. Single-Step Coating of Mesoporous Silica on Cetyltrimethyl Ammonium Bromide-Capped Nanoparticles. *Nano Lett.* **2008**, *8* (1), 369–373.

(3) Egger, S. M.; Hurley, K. R.; Datt, A.; Swindlehurst, G.; Haynes, C. L. Ultraporous Mesostructured Silica Nanoparticles. *Chem. Mater.* **2015**, *27* (9), 3193–3196.

(4) Keller, E. L.; Frontiera, R. R. Ultrafast Nanoscale Raman Thermometry Proves Heating Is Not a Primary Mechanism for Plasmon-Driven Photocatalysis. *ACS Nano* **2018**, *12* (6), 5848–5855.

(5) Shim, S.; Mathies, R. A. Generation of Narrow-Bandwidth Picosecond Visible Pulses from Broadband Femtosecond Pulses for Femtosecond Stimulated Raman. *Appl. Phys. Lett.* **2006**, *89* (12), 121124.

(6) McFarland, A. D.; Young, M. A.; Dieringer, J. A.; Van Duyne, R. P. Wavelength-Scanned Surface-Enhanced Resonance Raman Excitation Spectroscopy. *J. Phys. Chem. B* **2005**, *109* (22), 11279–11285.

(7) Gao, Z.; Burrows, N. D.; Valley, N. A.; Schatz, G. C.; Murphy, C. J.; Haynes, C. L. In Solution SERS Sensing Using Mesoporous Silica-Coated Gold Nanorods.

Analyst **2016**, *141* (17), 5088–5095.

(8) Marszewski, M.; Butts, D.; Lan, E.; Yan, Y.; King, S. C.; McNeil, P. E.; Galy, T.; Dunn, B.; Tolbert, S. H.; Hu, Y.; Pilon, L. Effect of Surface Hydroxyl Groups on Heat Capacity of Mesoporous Silica. *Appl. Phys. Lett.* **2018**, *112* (20), 201903.

(9) Braun, J. L.; Baker, C. H.; Giri, A.; Elahi, M.; Artyushkova, K.; Beechem, T. E.; Norris, P. M.; Leseman, Z. C.; Gaskins, J. T.; Hopkins, P. E. Size Effects on the Thermal Conductivity of Amorphous Silicon Thin Films. *Phys. Rev. B* **2016**, *93* (14), 140201.

(10) Combis, P.; Cormont, P.; Gallais, L.; Hebert, D.; Robin, L.; Rullier, J. L. Evaluation of the Fused Silica Thermal Conductivity by Comparing Infrared Thermometry Measurements with Two-Dimensional Simulations. *Appl. Phys. Lett.* **2012**, *101* (21), 1–5.

(11) Coquil, T.; Richman, E. K.; Hutchinson, N. J.; Tolbert, S. H.; Pilon, L. Thermal Conductivity of Cubic and Hexagonal Mesoporous Silica Thin Films. *J. Appl. Phys.* **2009**, *106* (3).

(12) Li, J.; Feng, Y.; Zhang, X.; Huang, C.; Wang, G. Near-Field Radiative Heat Transfer across a Pore and Its Effects on Thermal Conductivity of Mesoporous Silica. *Phys. B Condens. Matter* **2015**, *456*, 237–243.

(13) Wu, X.; Ni, Y.; Zhu, J.; Burrows, N. D.; Murphy, C. J.; Dumitrica, T.; Wang, X. Thermal Transport across Surfactant Layers on Gold Nanorods in Aqueous Solution. *ACS Appl. Mater. Interfaces* **2016**, *8* (16), 10581–10589.

(14) Huang, J.; Park, J.; Wang, W.; Murphy, C. J.; Cahill, D. G. Ultrafast Thermal Analysis of Surface Functionalized Gold Nanorods in Aqueous Solution. *ACS Nano* **2013**, *7* (1), 589–597.

Appendix D

Supporting Information for Manuscript:

Plasmon-Enhanced Chemical Sensing and Conversion using Copper Selenide Nanoparticles

D.1 General Methods and Materials

Copper(I) chloride (CuCl, > 99.995%), selenium powder (Se, > 99.5%), octadecene (ODE, 90% technical grade), oleylamine (OLA, 70% technical grade), chloroform (> 99%), polyvinylpyrrolidone (PVP, average molecular weight 10,000), benzenethiol (BT, ≥ 98%), 4-nitrobenzenethiol (NBT, 80% technical grade) were purchased from Sigma Aldrich (St. Louis, MO). Absolute ethanol (EtOH) was purchased from Thermo Fisher Scientific (Pittsburgh, PA). All chemicals were used as received with no additional purification unless otherwise noted. Prior to use, all glassware and Teflon stir bars were washed in aqua regia and rinsed with copious amounts of water prior to oven drying. Caution: aqua regia is highly toxic and corrosive, and should only be used with proper personal protective equipment and training. Aqua regia should be handled only inside a fume hood.

D.2 Synthesis of OAm Capped $Cu_{2-x}Se$ NPs

$Cu_{2-x}Se$ NPs were synthesized using a previously described hot injection method.[1,2] The synthetic procedure was completed using standard air-free techniques and is described in detail below. The selenium-octadecene-oleylamine mixture was created by dissolving 80 mg Se in 1 mL of ODE and 2 mL of OLA. The solution was heated in a round bottom flask for 12 hrs under argon gas at 195 °C. In a 3-neck round bottom flask, 200 mg CuCl was added with 5 mL OLA and 5 mL of ODE. The Cu-ODE-OLA mixture was heated to 140 °C under vacuum for 30 min then heated to 285 °C under Ar. Then, the Se mixture was injected into the Cu mixture. The precursors reacted for 10 min at ~285

°C to form $Cu_{2-x}Se$ NPs. The NPs were cooled to room temperature by removing the heating mantle.

The $Cu_{2-x}Se$ NP product was purified via centrifugation. First, the as-synthesized NPs were transferred to glass centrifuge tubes containing 10 mL of EtOH and centrifuged in an Eppendorf 5804R centrifuge with a swing bucket rotor (A-44-4) (Eppendorf, Inc.) at a force of 2850 rcf at 20 °C for 5 min. The resulting supernatant was removed and the pellet was resuspended in a small amount of $CHCl_3$ for additional centrifugation in another 10 mL of EtOH. This washing procedure was repeated once. All purified NPs were then characterized by high resolution transmission electron microscopy (HRTEM), ultraviolet-visible-near infrared (UV-vis-NIR) extinction spectroscopy, powder X-ray diffraction (PXRD), and Raman spectroscopy.

D.3 Ligand Exchange of $Cu_{2-x}Se$ NPs with 10 kDa PVP

Purified OAm capped $Cu_{2-x}Se$ NPs were dispersed in 4 mL $CHCl_3$. 6 mL of 8 mM of 10 kDa PVP solution in $CHCl_3$ was added into the dispersed NP solution and the mixture solution was left stirring overnight at room temperature. After incubation, the $Cu_{2-x}Se$ NP product was purified via centrifugation. First, the as-synthesized NPs were distributed to Eppendorf tubes in aliquots of 0.5 mL. 1 mL hexanes were added into the Eppendorf tubes and centrifuged in an Eppendorf 5424 centrifuge with a fixed angle rotor (F-45-30-11) (Eppendorf, Inc.) at a force of 15,000 rpm at 20 °C for 10 min. The resulting supernatant was removed and the pellet was resuspended in a small amount of $CHCl_3$ for additional centrifugation in another 1 mL of hexanes. This washing procedure

was repeated once. All purified NPs were then characterized by HRTEM, UV-vis-NIR extinction spectroscopy, and Raman spectroscopy.

D.4 High Resolution Transmission Electron Microscopy (HRTEM)

$Cu_{2-x}Se$ NPs were prepared for electron microscopy by drop casting an aliquot of purified NP solution (diluted 1:10 or 1:100 with $CHCl_3$) onto carbon film-coated copper transmission electron microscopy (TEM) grids (Ted Pella, Inc.) for routine bright field imaging analysis. TEM characterization was performed on a Hitachi H9500 Environmental TEM with an accelerating voltage of 300 kV (NanoScale Fabrication and Characterization Facility, Petersen Institute of NanoScience and Engineering, Pittsburgh, PA). The size distributions of the NPs were determined from TEM images of at least 200 NPs from various areas of the grid using ImageJ 1.47d (National Institutes of Health, USA).

D.5 Powder X-ray Diffraction (PXRD)

Purified $Cu_{2-x}Se$ NPs were characterized by PXRD using a Bruker AXS D8 Discover XRD (NanoScale Fabrication and Characterization Facility, Petersen Institute of NanoScience and Engineering, Pittsburgh, PA) at 40 kV, 40 mA for Cu Kα (λ = 1.5406 Å) X-ray source with a scan speed of 0.7 s/step from 10.00 - 90.00° with a step size of 0.02°. Samples were prepared by drop casting an aliquot of purified NP solution (diluted 1:10 or 1:100 with toluene) on a glass microscope slide (Fisher Scientific). All spectra were baseline corrected with respect to the spectrum of the amorphous glass background.

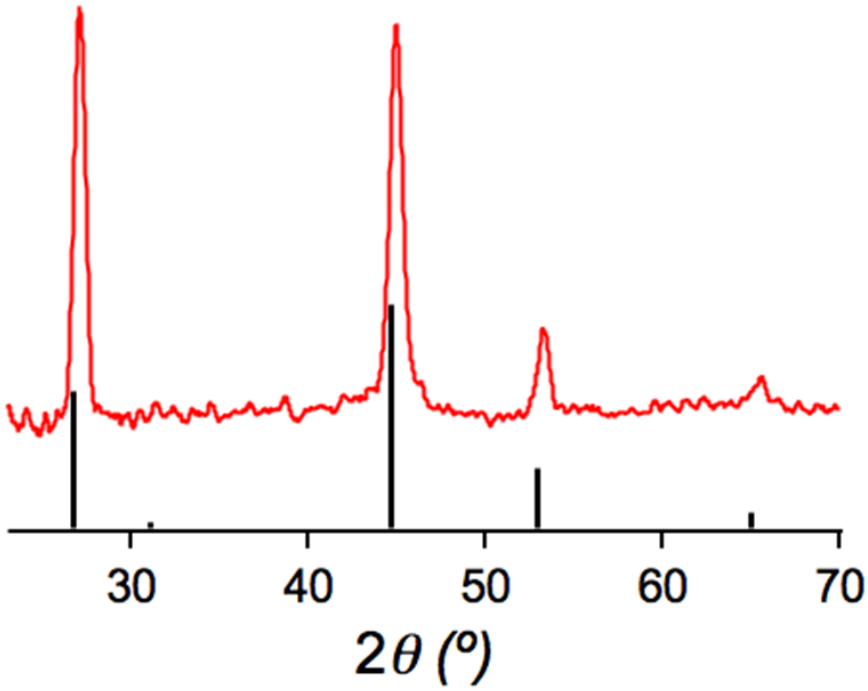

Figure D1. Representative PXRD pattern of $Cu_{2-x}Se$ NPs referenced to PDF # 00-006-0680

The lattice parameter (a) of the antifluorite structure was determined using the PXRD peak at 27°, which corresponds to the cubic (111). Using the Bragg equation described below:

$$a = \frac{\lambda\sqrt{h^2+k^2+l^2}}{2sin(\theta)} \quad \text{(D1)}$$

where λ is the X-ray source, h=k=l=1, the lattice parameter was calculated to estimate the volume of the unit cell for the quantification of NP concentration (vide infra).

D.6 Additions of Raman Analytes to $Cu_{2-x}Se$ NPs

250 µL of OAm capped $Cu_{2-x}Se$ NPs with an estimated optical density of ~5 at the LSPR maximum was added into a 1.5 mL Eppendorf tube, and BT and NBT solutions of concentrations ranging from 0 to 100 mM were added into the Eppendorf tubes to reach a final solution volume of 1.5 mL. The mixture solution was thoroughly mixed by incubation on the thermomixer (Eppendorf R Thermomixer) for at least an hour. The mixture solutions were then characterized by UV-vis-NIR extinction spectroscopy and Raman spectroscopy. Note that NPs were not purified after the addition of analytes to prevent NP instability, the concentration of analytes in solution is in excess compared to the NP concentration.

D.7 Analysis of $Cu_{2-x}Se$ NPs as a Function of Raman Analyte Addition

The LSPR properties of $Cu_{2-x}Se$ NPs before and after the addition of Raman analytes such as BT and NBT were measured using a UV-vis-NIR spectroscopy. As a function of increasing analyte concentrations, the LSPRs of $Cu_{2-x}Se$ NPs redshifted and plateaued (Figure D2). This observation resulted from the interaction between the thiol binding moiety present in both the Raman analytes and the NP surface, where the more electron donating thiolated headgroups reduce the carrier densities in $Cu_{2-x}Se$ NPs quantified using the Drude model. These results also indicate that BT is a more electron donating analyte than NBT, since the resulting redshifts are more dramatic (from 1080 nm to 1450 nm instead of 1200 nm). Using this study, we could then estimate the maximum surface coverage of Raman analytes on $Cu_{2-x}Se$ NPs, which is an important figure of merit for the SERS EF measurement.

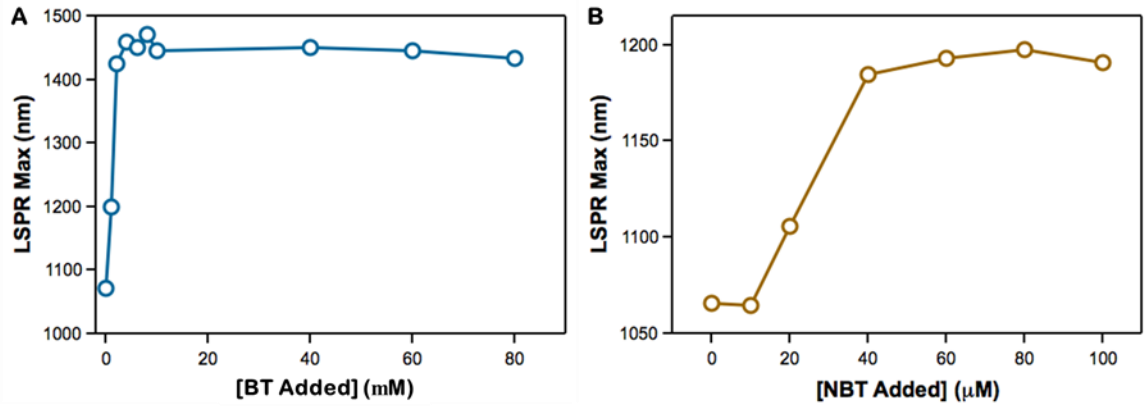

Figure D2. Shifts of LSPR maximum for OAm capped $Cu_{2-x}Se$ NPs as a function of increasing (a) BT and (b) NBT concentration in $CHCl_3$

D.8 Method for Inductively Coupled Plasma Optical Emission Spectrometry Analysis

ICP-OES analysis was performed using an argon flow with an Optima spectrometer (Perkin Elmer, Inc.). An aqua regia solution was prepared with a 3:1 ratio of hydrochloric acid (Sigma Aldrich, > 99.999% trace metal basis): nitric acid (Sigma Aldrich, > 99.999% trace metal basis) and diluted with water for a 5% v/v aqua regia matrix. Unknown Se and Cu concentrations were determined by comparison to a 7-point standard curve with a range of 0.10 - 10 ppm Cu and Se (0.10, 0.50, 1.0, 2.5, 5.0, 7.5, and 10 ppm of each metal prepared by volume) using a selenium standard for ICP (Fluka, TraceCERT 1000 ± 2 mg/L Se in HNO3) and Cu standard for ICP (Fluka, TraceCERT 1000 ± 2 mg/L Cu in HNO3), diluted in a 5% aqua regia matrix. All standards and unknown samples were measured 6 times and averaged. A 7 minute flush time with 5% aqua regia matrix was used between all runs, and a blank was analyzed before each unknown sample to confirm removal of all residual metals from the instrument.

D.9 Calculation of $Cu_{2-x}Se$ NP Concentrations

$Cu_{2-x}Se$ NP concentrations were determined using the UV-vis-NIR spectrum of the NPs before BT and NBT addition in $CHCl_3$ (Figure D3). Spectra were taken using a Cary 5000 UV-vis-NIR (Agilent, Inc.). UV-vis-NIR measurements were collected of NP suspensions diluted in $CHCl_3$ using 1.0 cm quartz cuvettes (Hellma, Inc.). Five serial dilutions of the concentrated NP stock were prepared in each solvent system for each ligand shell (OAm and PVP). These particles were air dried, digested in 5% aqua regia and then further diluted for analysis. The extinction spectra were measured from 800-1500 nm, the concentrations of NPs were measured by ICP-OES (vide supra), and the average diameters of the NPs were determined using HRTEM micrographs. The total number of unit cells per particle was estimated by dividing the volume of the NP sphere by the volume of the cubic antifluorite lattice of Cu_2Se. The volume of the antifluorite unit cell was determined by PXRD (vide supra). The total number of Se atoms was then estimated per particle by multiplying the number of unit cells per particle by 4, which is the number of Se atoms present in an antifluorite unit cell.

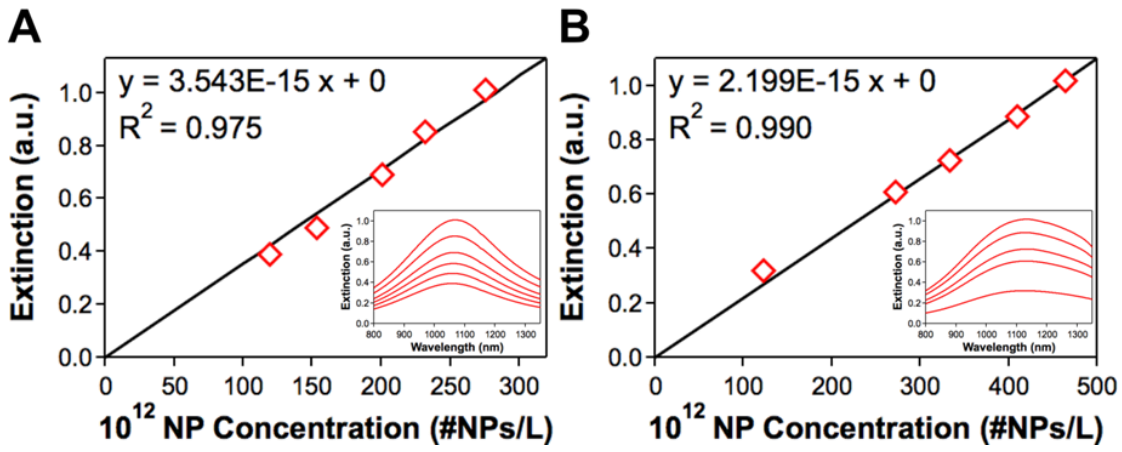

Figure D3. Molar extinction spectra of the (A) OAm and (B) PVP capped $Cu_{2-x}Se$ NPs dispersed in $CHCl_3$. The insets correspond to their extinction profiles.

D.10 ^{1}H Nuclear Magnetic Resonance (NMR) Spectroscopy

All ^{1}H NMR measurements were performed on a Bruker 400 Ultrashield magnet with an AVANCE III 400 Console or a Bruker 600 Ultrashield magnet with an AVANCE III 600 Console (Bruker Biospin, Billerica, MA) at 298 K. For all experiments, a minimum recycle delay of 15 s was used, which was sufficiently greater than T_1. NMR samples were prepared as described above by dissolving OAm in $CDCl_3$, and by concentrating the $Cu_{2-x}Se$ NPs in $CDCl_3$.

D.11 Quantifying the OAm Ligand Density on $Cu_{2-x}Se$ NPs

The OAm ligand density on $Cu_{2-x}Se$ NPs was quantified using a non-destructive ^{1}H NMR technique.[3] Briefly, following NP purification, the OAm capped $Cu_{2-x}Se$ NPs were air-dried diluted to a final volume of 2 mL of $CDCl_3$. 10 µL of the concentrated NP solution was further diluted to a final volume of 500 µL using $CDCl_3$, and analyzed via ^{1}H NMR. Dimethylsulfoxide (DMSO, 5 µL of 70 mM DMSO in$CDCl_3$) was added to

each sample as an internal standard. Proton peaks (2H) at δ=~5.4 ppm, which can be assigned to the allylic protons of OAm, were integrated with respect to the DMSO standard (6H). Particle concentrations in each sample were determined using ICP-MS and HRTEM as discussed in the calculation of molar extinction coefficient section (*vide supra*). Ligand densities were calculated by dividing the integrated allylic ligand concentrations by the concentration of NPs obtained using ICP-OES (note that the ICP-OES and ^{1}H NMR values were always obtained from the same sample solution). Representative ^{1}H NMR spectra of OAm capped $Cu_{2-x}Se$ NPs are included in Figure D4, in comparison with OAm solution without the presence of NPs. The average quantified OAm ligand density was 3.1 ± 0.4 nm^{-2}, where the error accounts for the standard error for over 10 experimental replicates. This reported ligand density corresponds to 1719 ± 250 OAm ligands on a $Cu_{2-x}Se$ NP surface, assuming the particles are spheres.

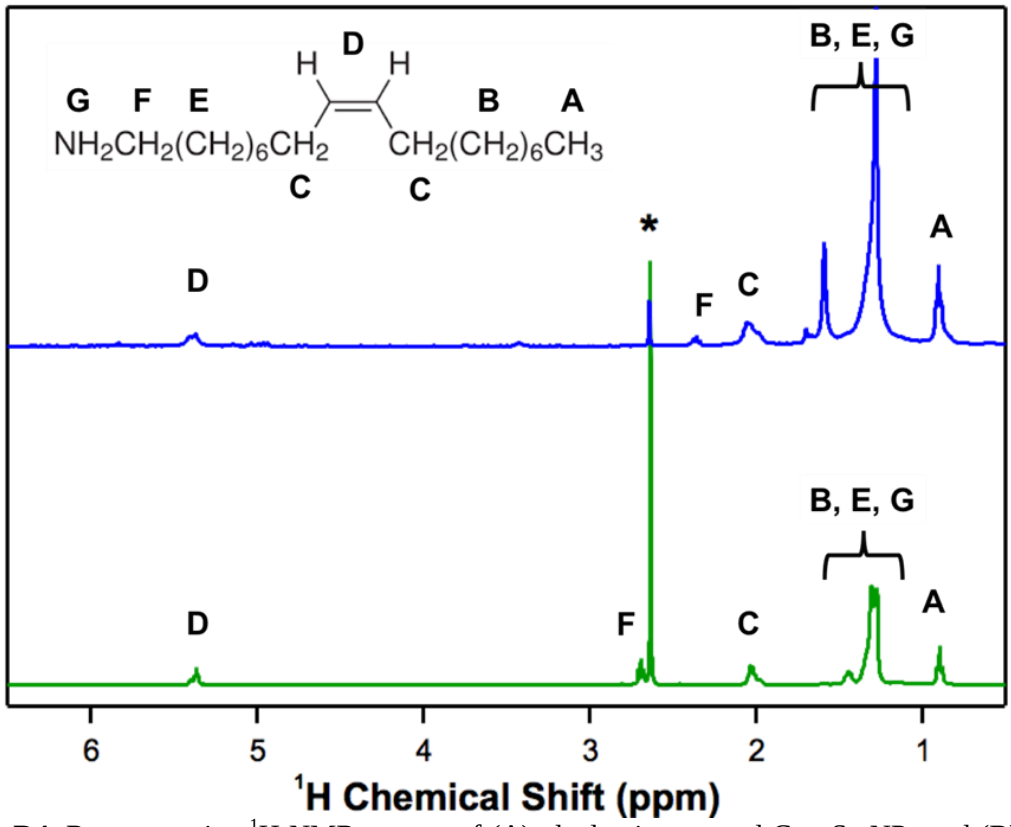

Figure D4. Representative ^{1}H NMR spectra of (A) oleylamine capped $Cu_{2-x}Se$ NPs and (B) free oleylamine in solution

D.12 Raman Spectroscopy Analysis

The SERS instrument is a modified version of a previously published set-up.[4] Briefly, 6W of <250 fs pulses, centered at 1035 nm, from a fiber amplifier (Clark MXR, Impulse), are sent through a spectral filter to generate picosecond pulses. In the spectral filter, the beam is directed through a transmission grating and focused onto a slit in front of a mirror.[5] The beam is then focused onto the sample. The spectral resolution is 17.8 cm^{-1} as measured by the 786 cm^{-1} peak in toluene and the pulse duration is 2.8 ps, as measured by the optical Kerr effect in toluene. After the sample, the spontaneous Raman signal is sent through a 1064 nm Razor Edge Raman filter and focused into a

spectrograph (Princeton Instruments, Acton SP2300) containing a 300 gr/mm grating blazed at 1 μm. The Raman signal is collected with a 1024 pixel, liquid N_2 cooled InGaAs array (Princeton Instruments, Pylon-IR 1.7). The spectra were collected as 3 frames with 20 s acquisitions. The frames were averaged together and the spectra were scaled with respect to acquisition time and laser power. For all measurements, the flux was 350 W/cm^2, which corresponds to 5.4 MW/cm^2 peak power.

D.13 Estimation of SERS Enhancement Factor for $Cu_{2-x}Se$ NPs

The SERS enhancement factor (EF) for $Cu_{2-x}Se$ NPs was determined by the following equation (D2):

$$EF = \frac{I_{SERS}N_{NRS}}{N_{SERS}I_{NRS}} \quad \text{(D2)}$$

where I_{SERS} and I_{NRS} are the Raman intensities of a specific mode for the SERS and normal Raman spectroscopy (NRS) measurements, respectively, while N_{SERS} and N_{NRS} correspond to number of BT molecules adsorbed on the plasmonic substrate and in solution, respectively, for the probed volume.

In Figure 6.2A, the grey spectrum represents a normal Raman spectrum of BT diluted with chloroform to 98 mM. We can fit each Raman peak to a Gaussian to extrapolate the peak amplitude which is equivalent to I_{NRS} for each mode. From the known concentration of the solution, we can calculate N_{NRS} after measuring the focal volume of the laser. The spot radius of the laser beam at the focus was determined by

measuring the power before and after a 50 μm diameter pinhole at the sample position and placing the values in the following equation (D3):

$$spot\ radius = 2\sqrt{\frac{-2\left(\frac{d}{2}\right)^2}{ln\left(1-\frac{p_a}{p_b}\right)}} \quad \text{(D3)}$$

where d is the diameter of the pinhole, p_b is the power before the pinhole, and p_a is the power after the pinhole. For these experiments, the focal volume was 2 x 10^{-5} mL. By multiplying the focal volume by the concentration of the BT solution and converting moles to molecules using Avogadro's number, N_{NRS} is 1.2 x 10^{15} molecules.

N_{SERS} was calculated by first determining the concentration of NPs in the focal volume (2 x 10^{-5} mL). From the extinction spectrum (Figure 6.1C), the optical density is 0.166 at the LSPR maximum, which corresponds to 5 x 10^{13} particles/L based on the molar extinction coefficient (Figure D3). By multiplying the focal volume by the particle concentration, the number of particles in the focal volume is 1 x 10^6. Next, we can estimate the surface area of a particle from the average particle diameter measured by TEM (Figure 6.1B, 16 ± 2 nm). Assuming the particles are spheres, the surface area is 8 x 10^{-4} μm^2.

In addition to particle concentration, the other key component of determining N_{SERS} is estimating the packing density of the analyte on the NP surface. For these experiments, the packing density is estimated based on the capping ligand density of the NPs.[3] Additionally, Osawa et al. reported that a self-assembly monolayer of BT on Au

(111) surface has a maximum density of 3.2 molecules/nm^2 where the BT molecules are attached at a tilt angle.[6] These densities assume that the analyte completely displaces the capping ligand on the surface of the NPs. Due to NP instability post-purification, the $Cu_{2-x}Se$ NPs ligand shell could not be analyzed using 1H NMR techniques.[7] Instead, LSPR shifts were used to quantitatively access the relative surface coverage of BT in $Cu_{2-x}Se$ NPs (Figure D2). From these packing density estimates, the number of molecules per particle is 2400, which gives a N_{SERS} of 2.4 x 10^9 molecules.

The I_{SERS} at each concentration is measured by fitting each peak (Figure 6.2A) to a Gaussian to extrapolate the peak amplitude, which is equivalent to the intensity (Table D1). At this point, we would normally be able to calculate an enhancement factor. However, in these experiments, an excess of BT was used and this excess must be taken into account. We have done so in the following manner. After finding the I_{SERS} for each BT concentration, we can calculate the I_{SERS}/N_{SERS} ratio by dividing each intensity by the number of molecules (Table D1). Each sample has the same concentration of particles and due to the excess of BT added, we can assume that N_{SERS} is the same for all three concentrations. We can then repeat the N_{NRS} calculation, described above, to determine the number of BT molecules at each concentration if we assume there are no NPs present (Table D1). We then plot the I_{SERS}/N_{SERS} ratio against the N_{NRS} at each concentration to obtain Figure 6.2B. If we fit these data to a linear regression, the y-intercept (4.9 x 10^{-12}) can be used as an idealized I_{SERS}/N_{SERS} ratio that accounts for the excess BT in the samples. Using this ratio in Equation D2 with the NRS ratio described earlier for the 98 mM BT solution, we obtain an enhancement factor of ~10^4.

Table D1. Relative SERS intensities of 1002 cm^{-1} mode of BT at various concentrations for the quantification of an enhancement factor for $Cu_{2-x}Se$ NPs

[BT] (mM)	I_{SERS}	I_{SERS}/N_{SERS}	N_{NRS}
3.9	0.030	1.2×10^{-11}	4.7×10^{13}
19.6	0.100	4.17×10^{-11}	2.4×10^{14}
58.8	0.290	1.21×10^{-10}	7.1×10^{14}

D.14 Time-Resolved SER Spectra of NBT Dimerization on OAm and PVP Capped $Cu_{2-x}Se$ NPs

The difference spectra shown in Figure 6.3 were obtained by subtracting the spectrum obtained upon initial exposure to the laser (0 min) from the spectrum obtained after 5 minutes of irradiation (Figure D5). The grey spectrum in Figure D5 is a normal Raman spectrum of NBT. The NBT peaks are marked by black dashed lines and the DMAB product peak is denoted with a red dashed line. Solvent ($CHCl_3$) peaks are denoted by asterisks. Spectra are shown for both the OAm capped (Figure D5a) and the PVP capped (Figure D5b) $Cu_{2-x}Se$ NP samples.

From these spectra, we can estimate a percent yield for this reaction on $Cu_{2-x}Se$ NPs. First, we fit the 1344 and 1580 cm^{-1} reactant peaks before and after irradiation to a Gaussian function to extrapolate the peak amplitude. We account for any changes in signal by comparing the amplitude changes between the nitro stretch (1344 cm^{-1}) and the C-C stretch (1580 cm^{-1}) from before and after irradiation. Then we can fit the 1458 cm^{-1} product peak to obtain its peak amplitude. By placing the peak amplitudes into Equation

D5,[8] we can obtain the percent yield for this reaction to between 23 – 27% for OAm capped $Cu_{2-x}Se$ NPs and between 21 – 26% for PVP capped $Cu_{2-x}Se$ NPs.

$$Percent\ Yield = \frac{Final\ Product\ Amplitude}{Final\ Reactant\ Amplitude} \qquad (D4)$$

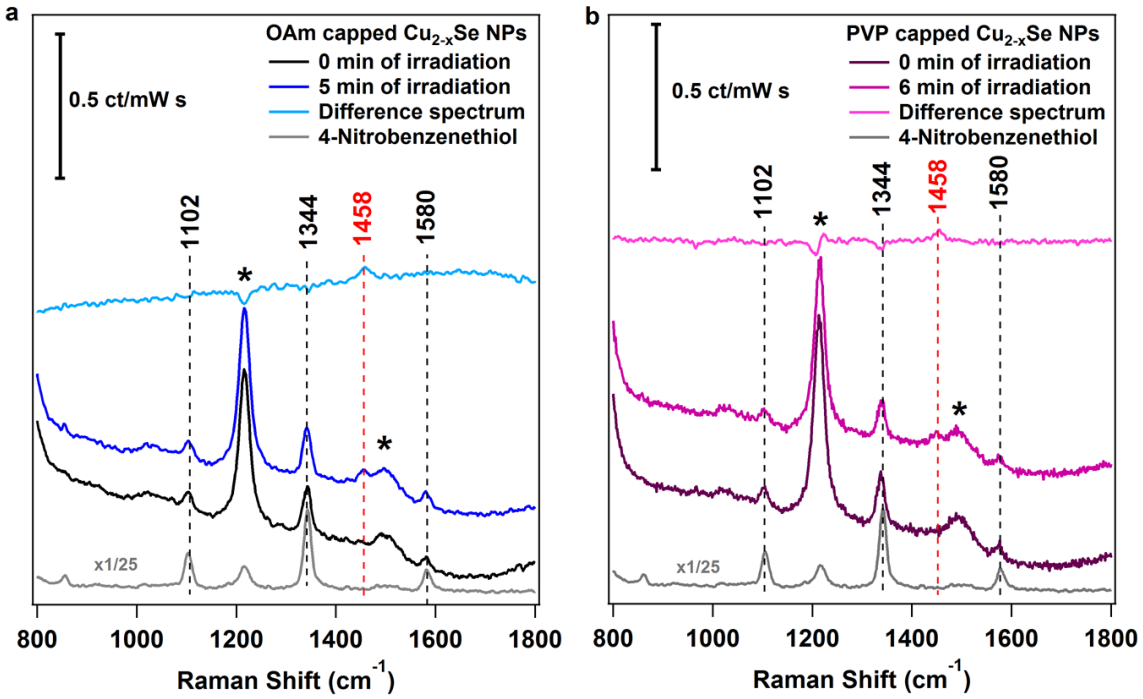

Figure D5. Time-resolved SER spectra of NBT in the presence of (a) OAm and (b) PVP capped $Cu_{2-x}Se$ NPs. Black dashed lines denote NBT and the red dashed line marks the growth of a DMAB peak in the spectrum obtained after 5 minutes of irradiation.

Additionally, we performed a control experiment by irradiating a concentrated NBT solution in the absence of $Cu_{2-x}Se$ NPs at the same power and duration as the samples containing $Cu_{2-x}Se$ NPs. As can be seen in the difference spectrum in Figure D6, no DMAB peaks are present after 5 minutes of irradiation showing the necessity of the plasmonic $Cu_{2-x}Se$ NPs for the dimerization of NBT

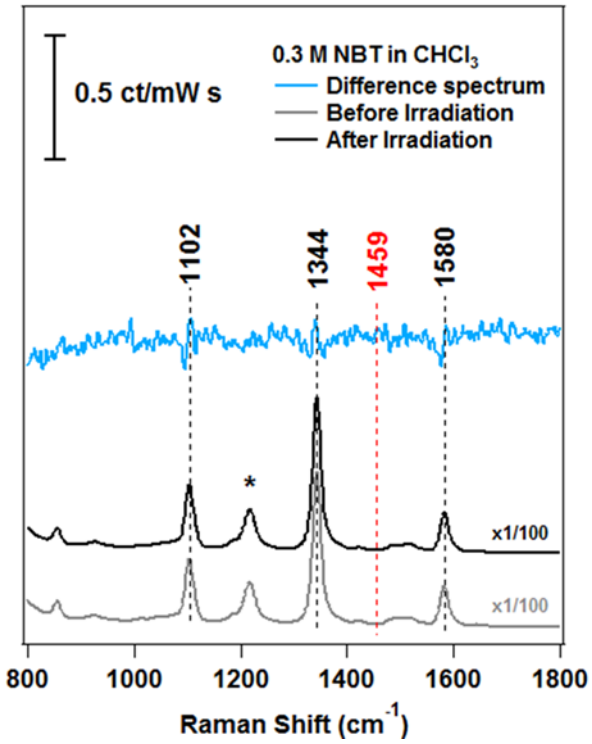

Figure D6. Time-resolved normal Raman spectra of NBT in the absence of $Cu_{2-x}Se$ NPs. After 5 minutes of irradiation, DMAB has not formed.

D.15 References

(1) Marbella, L. E.; Gan, X. Y.; Kaseman, D. C.; Millstone, J. E. Correlating Carrier Density and Emergent Plasmonic Features in Cu 2-x Se Nanoparticles. *Nano Lett.* **2017**, *17* (4), 2414–2419.

(2) Deka, S.; Genovese, A.; Zhang, Y.; Miszta, K.; Bertoni, G. Phosphine-Free Synthesis of p-Type Copper (I) Selenide Nanocrystals in Hot Coordinating Solvents. *J. Am. Chem. Soc.* **2010**, *132* (26), 8912–8914.

(3) Smith, A. M.; Johnston, K. A.; Crawford, S. E.; Marbella, L. E.; Millstone, J. E. Ligand Density Quantification on Colloidal Inorganic Nanoparticles. *Analyst* **2017**, *142* (1), 11–29.

(4) Keller, E. L.; Frontiera, R. R. Monitoring Charge Density Delocalization upon Plasmon Excitation with Ultrafast Surface-Enhanced Raman Spectroscopy. *ACS Photonics* **2017**, *4* (5), 1033–1039.

(5) Shim, S.; Mathies, R. A. Generation of Narrow-Bandwidth Picosecond Visible Pulses from Broadband Femtosecond Pulses for Femtosecond Stimulated Raman. *Appl. Phys. Lett.* **2006**, *89* (12), 121124.

(6) Wan, L.; Terashima, M.; Noda, H.; Osawa, M. Molecular Orientation and Ordered Structure of Benzenethiol Adsorbed on Gold (111). *J. Phys. Chem. A* **2000**, *104* (15), 3563–3569.

(7) Smith, A. M.; Marbella, L. E.; Johnston, K. A.; Hartmann, M. J.; Crawford, S. E.; Kozycz, L. M.; Seferos, D. S.; Millstone, J. E. Quantitative Analysis of Thiolated Ligand Exchange on Gold Nanoparticles Monitored by 1 H NMR Spectroscopy. **2015**.

(8) Brooks, J. L.; Frontiera, R. R. Competition between Reaction and Degradation Pathways in Plasmon-Driven Photochemistry. *J. Phys. Chem. C* **2016**, *120* (37), 20869–20876.

Appendix E

Supporting Information for Chapter 7:

Prospects

E.1 Methods for Mode-Specific Energy Transfer Experiments

E.1.1 Sample Preparation

Colloidal gold nanoparticles were prepared by following the Frens method for citrate-capped gold nanoparticles with a listed diameter of 97.5 nm.[1] Under heat and stirring, 7.4 mg of gold (III) citrate dissolved in 74 mL DI H_2O were combined with 1.55 mL of 1% by weight aqueous sodium citrate dihydrate. After 15 minutes, nanoparticles were formed with an average diameter of 80 ± 30 nm, as measured by SEM (JEOL 6700F) using ImageJ software. The gold nanoparticle were concentrated by centrifuging 1 mL as-synthesized gold nanoparticles for 50 minutes and removing 0.97 mL of the supernatant. The nanoparticles were combined with 2 µL of a saturated aqueous solution of 7-(trifluoromethyl)qunionline-4-thiol. The samples were prepared for ultrafast measurements by dropcasting 3 µL of the NP-analyte solution onto a glass slide. The solvent was allowed to evaporate prior to the measurement. Gold (III) chloride, sodium citrate dehydrate, potassium nitrate, and 7-(trifluoromethyl)quinoline-4-thiol were obtained from Sigma Aldrich and used without further purification.

An extinction spectrum was obtained with a Shimadzu UV-2600 UV-Vis spectrometer with an integrating sphere (Figure E1).

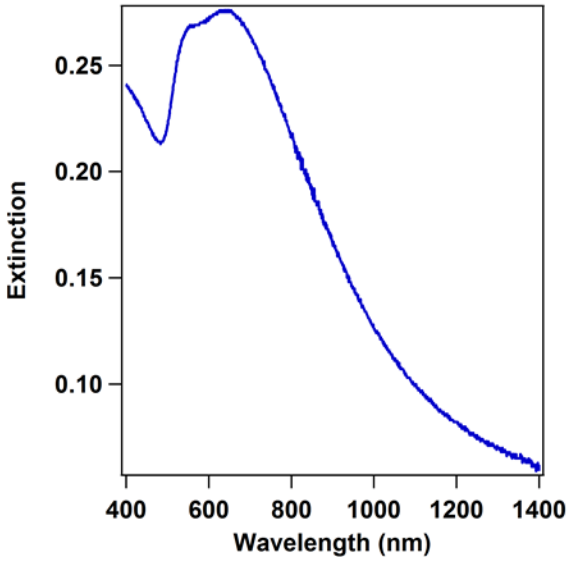

Figure E1. Extinction spectrum of 7-(trifluoromethyl)quinoline-4-thiol (CFQ) adsorbed to aggregated gold nanoparticles deposited on a glass slide

E.1.2 Data Collection and Processing

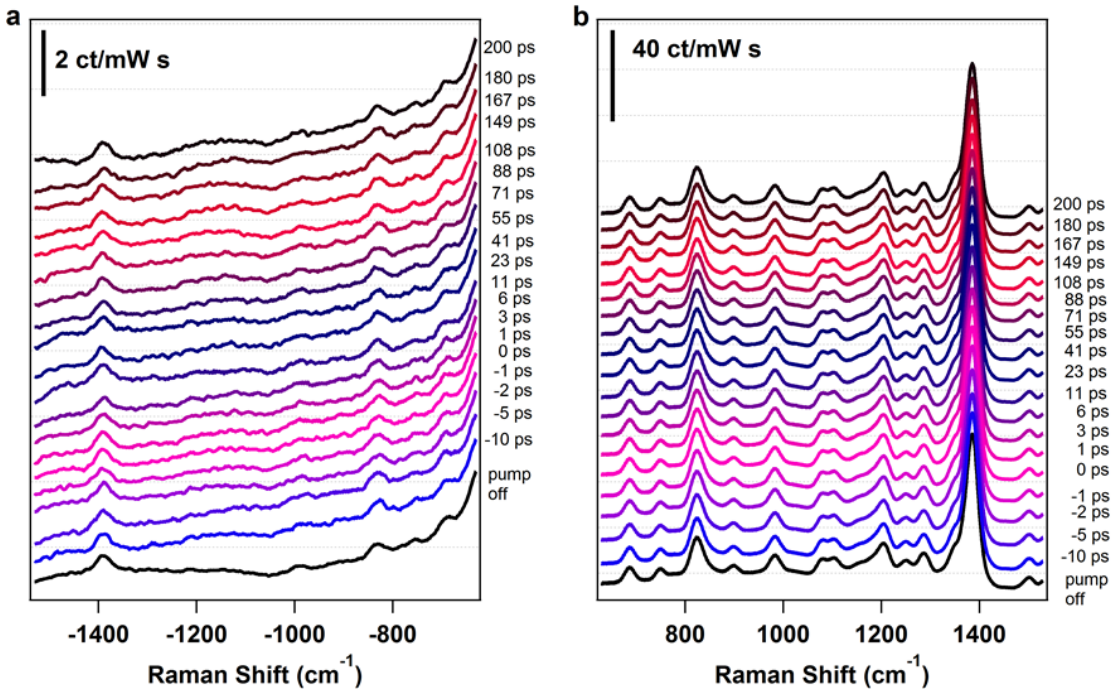

Figure E2. Ultrafast surface-enhanced (a) anti-Stokes and (b) Stokes spectra for 7-(trifluoromethyl)quinoline-4-thiol adsorbed to aggregated AuNPs. Spectra were obtained by photoexciting with 8.3 W/cm^2 at 518 nm and probing with 100 W/cm^2 at 1035 nm. Spectra are offset for clarity.

Each SER spectrum consists of 3 spectra that were acquired for 30s and averaged together (Figure E2). For each mode of interest, the peak at each time point was fit to a Gaussian to extrapolate the peak amplitude. These amplitudes were used in the Boltzmann distribution analysis as described by Equation (E1):

$$\text{Effective Temperature (K)} = \frac{-\text{Energy of Vibration (J)}}{k_b * \ln\left(\frac{\text{Intensity}_{\text{anti-Stokes}}}{\text{Intensity}_{\text{Stokes}}}\right)} \quad \text{(E1)}$$

where k_b represents the Boltzmann constant. To account for wavelength dependent enhancement from SERS and the detector efficiencies, the effective temperature were normalized with respect to the effective temperature of pump-off spectrum for each

mode. The resulting normalization allowed for the comparison between modes in terms of relative energy, as shown by the scale bar in Figure 7.1.

E.1.3 Oscillatory Features Present after 10 ps for Solution Phase Samples

As mentioned in Chapter 7, this dissertation primarily focuses on heating responses that occur within the first 25 ps after photoexcitation. However, preliminary data examining the heating response at later time points have been collected for solution phase samples. The solution phase samples are identical to the aggregated AuNPs samples with adsorbed 4-NBT that were discussed in Chapter 4. As mentioned in Chapter 7, sample heterogeneity strongly affects the heating response we observe at later time points. In Figure E3, I show the effective temperature plots for the ring breathing mode (1079 cm^{-1}) and the symmetric nitro stretch (1340 cm^{-1}) for 4-NBT from 10 ps to 200 ps for two different samples. The effective temperature plots are offset for clarity. As can be seen, each mode exhibits a similar pattern of oscillations over this time period, however, the relative magnitude at each time point can vary significantly. If we then consider potential sample instability and degradation over the course of subsequent measurements,

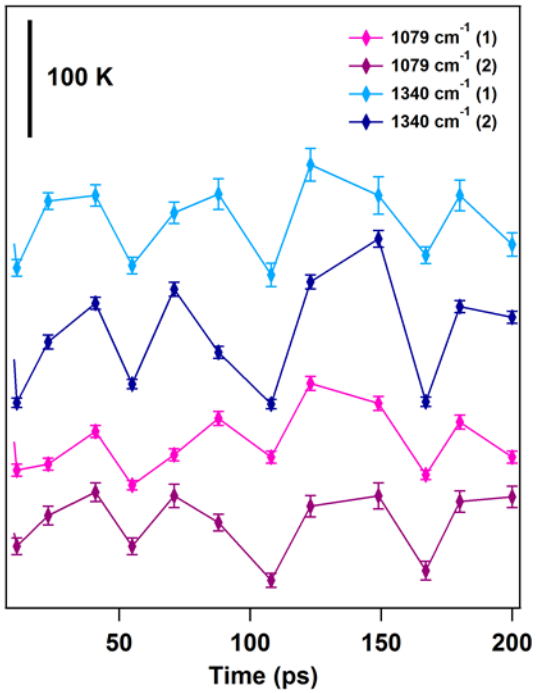

Figure E3. Comparison of oscillatory features that arise in solution phase samples containing 4-nitrobenzenethiol adsorbed to aggregated AuNPs for two different samples. The data sets are offset for clarity.

these oscillatory features become lost in the noise. While we can extrapolate important information about heat dissipation from the system on this time scale, this type of sample may not be optimal for these measurements.

E.2 Methods for Experiments with AlNC-Pd Nano-Antenna Reactors

E.2.1 Sample Preparation

Samples obtained from Dayne Swearer from the Halas group at Rice University.[2] Samples for ultrafast experiments were prepared by centrifuging 200 µL of as received AlNC-Pd (189B) suspended in 2-propanol for 30 minutes and removing 180 µL of the supernatant. The remaining 20 uL were split in half and 10 µL of AlNC-Pd suspended in 2-propanol were combined with 2 µL of 50 mM aqueous catechol in a microcentrifuge tube. On a clean glass slide, 3 µL were dropcasted and the solvent was allowed to evaporate.

The extinction spectrum in Figure 7.2b was obtained with a Shimadzu UV-2600 UV-Vis spectrometer with an integrating sphere.

E.2.2 Data Collection and Processing

Each spectrum consists of 3 spectra that were acquired for 30s and averaged together. Normally, a pump-off spectrum is taken followed immediately by a pump-on spectrum at each time point. After the spectra are averaged, the pump-off spectrum is subtracted from the pump-on spectrum to see the effects of excitation at different time delays. However, there is a great deal of static background from the pump beam which

makes the difference spectra from this subtraction difficult to interpret due to the large background. Instead of subtracting a pump-off spectrum, a spectrum at -50 ps is taken with the pump on and this spectrum is used as a substitute for the pump-off spectrum. At -50 ps, the probe pulse arrives before the pump pulse, thus the spectrum only shows the static background from the pump without any sample dynamics due to excitation.

E.2.3 Theoretical Modeling of AlNC-Pd Nano-Antenna Reactors

Yue Zhang in Peter Nordlander's group at Rice University performed theoretical modeling of the plasmonic properties of AlNC-Pd nano-antenna reactors with various AlNC diameters. She modeled the scattering cross section and the electric field enhancements for diameters between 110 to 200 nm. The electric field enhancement is 'measured' at a distance of 1 nm from a Pd island on the surface of the AlNC. The AlNC is assumed to have a 3 nm outer alumina layer and the particles are suspended in IPA, which has a refractive index of 1.37. From these computations, the optimal AlNC diameter was 200 nm shown in Figure E4. By comparing this figure to Figure 7.2b, it becomes clear that scattering dominates the experimental LSPR of the 200 nm AlNC-Pd nano-antenna reactors.

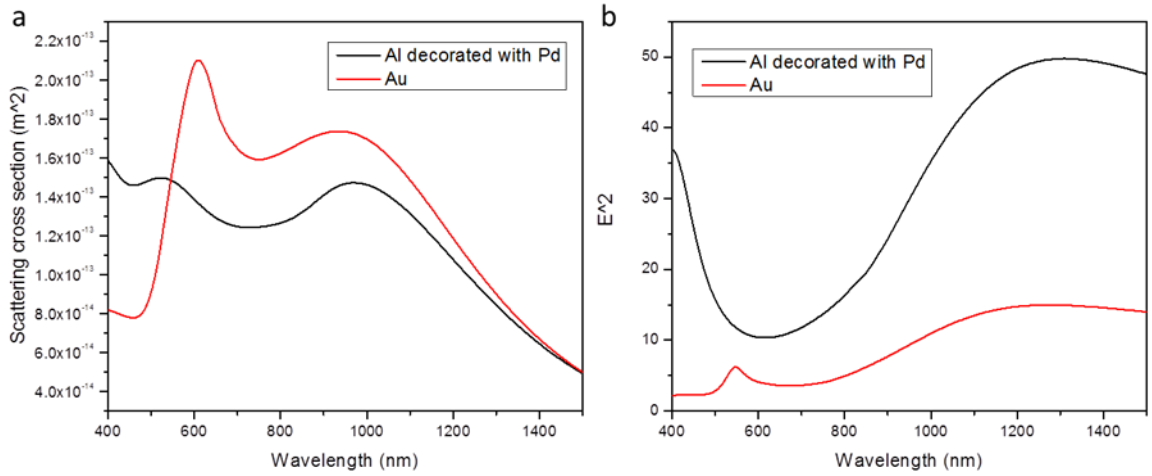

Figure E4. Theoretical modeling of the wavelength dependent (a) scattering cross sections and (b) electric field enhancement for AlNC-Pd nano-antenna reactors compared to similar AuNPs. Scattering dominates in the experimental LSPR (Figure 7.2b) Calculations and Figures courtesy of Yue Zhang and Peter Nordlander

E.3 SERS Instrument Set-up

A detailed description of the ultrafast SERS instrumentation has been published previously.[3] In brief, <250 fs laser pulses, centered at 1035 nm from a fiber amplifier (Clark-MXR Impulse) were split with a 50:50 beam splitter to make the pump and probe beams. The pump beam at 518 nm was generated by SHG in a 3 mm beta-barium borate (BBO) crystal (Newlight Photonics), and the 1035 nm used a portion of the fundamental laser beam directly.The pump beam was sent onto a motorized delay stage (Newport XMS500) before the sample to vary the time delay. To generate the narrowband picosecond probe beam, the femtosecond pulses were sent into a spectral filter where they were dispersed by a transmission grating onto a slit.[4] After the sample, the spontaneous Raman scattering was directed to a spectrograph (Princeton Instruments, 2300i) with a 600 gr/mm grating blazed at 750 nm or a 300 gr/mm grating blazed at 1 μm

onto a 1024 pixel InGaAs array (Princeton Instruments PYLON-IR 1.7). A 850 nm long pass filter (Thorlabs FEL850) removed the remaining pump light and a 1064 nm Raman Edge filter (Edmund Optics 47-510) was placed before the spectrograph to remove the Rayleigh scatter. The data were collected using home-written LabView code. The instrument response of this set-up is 2.17 ps, as measured by the optical Kerr effect on a glass slide while the spectral resolution is 13 cm^{-1}, as measured from the 800 cm^{-1} mode of cyclohexane. All data were collected with a repetition rate of 24.5 MHz.

The spot size of the probe was 1 x 10^{-4} cm^2 and the pump had a spot size of 6 x 10^{-4} cm^2 for 518 nm excitation. Each spot radius was determined by measuring the power before and after a 50 μm diameter pinhole at the sample position and placing the values in the following equation (E2):

$$\text{spot radius} = 2\sqrt{\frac{-2\left(\frac{d}{2}\right)^2}{\ln\left(1-\frac{p_a}{p_b}\right)}} \qquad \text{(E2)}$$

where d is the diameter of the pinhole, p_b is the power before the pinhole, and p_a is the power after the pinhole. Table E1 & E2 list the probe and pump peak energy, fluence, flux, and peak power for the CFQ and AlNC-Pd experiments, respectively.

Table E1. List of photoexcitation and probe peak energy, fluence, flux, and peak power for experiment with CFQ adsorbed on aggregated AuNPs

	Peak Energy (nJ)	Fluence ($\mu J/cm^2$)	Flux (W/cm^2)	Peak Power	
Pump	0.20	0.34	8.3	1.3 MW/cm^2	0.052 J/cm^2
Probe	0.41	4.1	100	1.8 MW/cm^2	0.072 J/cm^2

Table E2. List of photoexcitation and probe peak energy, fluence, flux, and peak power for experiment with AlNC-Pd

	Peak Energy (nJ)	Fluence ($\mu J/cm^2$)	Flux (W/cm^2)	Peak Power	
Pump	0.12	0.20	5.0	0.80 MW/cm^2	0.03 J/cm^2
Probe	0.37	3.7	90	1.6 MW/cm^2	0.065 J/cm^2

E.4 References

(1) Frens, G. Controlled Nucleation for the Regulation of the Particle Size in Monodisperse Gold Suspensions. *Nat. Phys. Sci.* **1973**, *241*, 20–22.

(2) Swearer, D. F.; Leary, R. K.; Newell, R.; Yazdi, S.; Robatjazi, H.; Zhang, Y.; Renard, D.; Nordlander, P.; Midgley, P. A.; Halas, N. J.; Ringe, E. Transition-Metal Decorated Aluminum Nanocrystals. *ACS Nano* **2017**, *11* (10), 10281–10288.

(3) Keller, E. L.; Frontiera, R. R. Monitoring Charge Density Delocalization upon Plasmon Excitation with Ultrafast Surface-Enhanced Raman Spectroscopy. *ACS Photonics* **2017**, *4* (5), 1033–1039.

(4) Shim, S.; Mathies, R. A. Generation of Narrow-Bandwidth Picosecond Visible Pulses from Broadband Femtosecond Pulses for Femtosecond Stimulated Raman. *Appl. Phys. Lett.* **2006**, *89* (12), 121124.